Fast acoustic tomography of coastal, tidally-driven temperature and current fields

by

Pierre Elisseeff

M.S., Ecole Centrale Paris, 1991
M.S., Florida Atlantic University, 1991

Submitted to the Department of Ocean Engineering
in partial fulfillment of the requirements for the Degree of

Doctor of Philosophy in Ocean Engineering

at the

MASSACHUSETTS INSTITUTE OF TECHNOLOGY
[June]
May 1998

Author . . . .
Department of Ocean Engineering
February 27, 1998

Certified by. . . . .
Professor Henrik Schmidt
Department of Ocean Engineering
Thesis Supervisor

Accepted by . . . .
Professor J. Kim Vandiver
Chairman, Departmental Graduate Committee
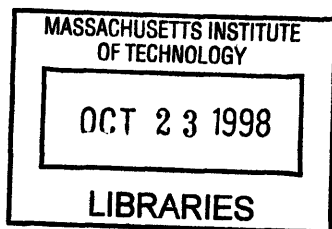
Fast acoustic tomography of coastal, tidally-driven temperature and current fields

by

Pierre Elisseeff

Submitted to the Department of Ocean Engineering
on February 27, 1998 in partial fulfillment of the
requirements for the Degree of
Doctor of Philosophy in Ocean Engineering

Abstract

Recent developments in wireless communication technology combined with significant increases in computing power have opened the way to Acoustically Focused Oceanographic Sampling (AFOS). AFOS consists of a network of acoustic arrays connected to a fleet of Autonomous Underwater Vehicles (AUV) and to a shore station using wireless local area network technology. A real-time field estimate of temperature or current in the region of interest is computed by combining the various integral and local data sets available. The real-time field estimate and its associated error field are then used to adaptively direct AUVs towards regions where high resolution is required due to large gradients or large uncertainties. A feasibility experiment was recently performed in Haro Strait, British Columbia (June-July 1996). The novelty of the Haro Strait data set resides in its unusual tomographic features: ranges are short (less than 3 km), sound speed perturbations are small (2 to 3m/s), and currents are relatively strong (up to 5 kts). Operational constraints require that the field inversion be robust and computationally efficient. This thesis makes contributions to both the forward and the inverse problem. Numerically efficient solutions to the windy wave equation are presented in the wavenumber integration and the normal mode approaches using a unified theoretical formulation. Accurate numerical predictions of the acoustic field in the presence of a stratified flow are made using modified versions of the computer codes OASES and KRAKEN. A robust, hybrid linear inversion scheme adapted to the estimation of oceanic fields in coastal environments such as Haro Strait is then developed. Expressions for hybrid field estimates as well as their associated estimate variances are derived. These expressions enable the combination of multiple data streams of global and local nature in a robust and and efficient fashion. Inversion performance is subsequently assessed, showing significant gains in coverage and estimated error from the combination of multiple data sets. Signal frequency coherence is shown to be a key asset in the Haro Strait environment. Second-order field statistics are computed, and the position of the Haro Strait front during flood tide on 06/20/96 was estimated.

Thesis Supervisor: Henrik Schmidt
Title: Professor, Department of Ocean Engineering

Acknowledgments

As any other achievement, a dissertation is the result of a collaborative effort. I would like to thank first and foremost my adviser, Henrik Schmidt, for his ever present support and thoughtful guidance. Henrik has been an adviser in the true sense of the term as well as a mentor, providing much needed help and advice on all aspects of the thesis. I hope we will have the opportunity to work together for years to come. I am grateful to Dr Tom Curtin at the U.S. Office of Naval Research for having funded the Haro Strait project and my research as a graduate student at MIT. Art Baggeroer, Bill Carey and Jim Lynch provided important input on my work at critical stages of the thesis. Dr Carlos Lozano (Harvard University) guided my first steps through the maze of data assimilation techniques and is for this reason an integral part of whatever degree of success this dissertation may achieve. Dr Rich Pawlowicz provided critical help in setting up and running Foreman's tidal model.

In addition I would like to thanks all the people who, directly or not, contributed to this dissertation through their help, encouragement and support. In particular much of the numerical work would have been impossible without the never ending help of Peter Daly and Brian Sperry. Sabina Rataj provided inexhaustible administrative as well as psychological support. I give many thanks to the rest of the folks in 5-435 (Vincent, Caterina, Jai, Yurij, Eugene, Kyle, Dan, ...) for having made this experience more enjoyable and having shared the highs and lows of graduate student life.

Finally, I would like to thanks my family and my wife, Jennifer, for their unending support and confidence in me.

Contents

List of Figures

10

12

List of Tables

Chapter 1

Introduction

1.1   Forward and inverse problems

Acoustic waves have long been a privileged means of remotely sensing ocean sub-surface structures, whether for military purposes such as surveillance, detection and counter-measures, or civilian purposes such as oceanographic modeling and climate monitoring. Remote sensing involves two fundamentally different problems. First, in order to properly extract source or environmental information from signals propagating through the ocean, the physical mechanisms accounting for propagation must be adequately modeled and quantitative field predictions must be available. This is the *forward problem*, whereby the modeler is able to produce an accurate wave field prediction based on an arbitrary environmental input. In the second and final stage, the measured field is used to infer the value of different source or environmental parameters such as source location, ocean temperature and salinity. This stage corresponds to the *inverse problem*, whose mathematical analysis is strictly distinct from that the forward problem. The forward problem is essentially a wave propagation problem and as such is quite specific. On the other hand the inverse problem amounts, loosely speaking, to properly inverting a matrix and is therefore relatively general. In particular the inverse problem draws on techniques developed from backgrounds as various as seismic imaging (oil exploration), computerized axial tomography (medical imaging) and data assimilation (atmospheric and oceanographic modeling) in addition to

modern ocean-specific techniques such as matched-field processing.

Over the last two decades acoustic waves have been proven to be a viable and reliable tool for measuring deep ocean temperature and current fields. Ocean acoustic tomography, thus called by analogy to medical imaging techniques, was repeatedly and successfully used in order to image mesoscale structures in the Atlantic as well as in the Pacific ocean. The advantage of ocean acoustic tomography over traditional oceanographic sampling methods is clearly one of coverage, therefore of cost. With only a few moorings areas of the order of hundreds of kilometers can be continuously monitored. This however comes at the expense of resolution. The inherent spatial averaging performed by acoustic waves in the course of propagation from source to receiver limits the horizontal resolution of acoustic measurement to typically a few kilometers along the path of propagation. Following advances in the deep ocean case tomographic inversions are now being applied with varying degrees of success to coastal environments, whose spatial and temporal scales are orders of magnitude smaller than that of the deep ocean.

This raises several issues with respect to both the forward and the inverse problem. Whereas sound speed fluctuations almost always dominate current fluctuations in the deep ocean case, the combination of tides and topography in coastal regions yields currents whose magnitude may be in some cases comparable to that of sound speed fluctuations. The influence of currents on acoustic propagation must therefore be carefully modeled. In particular the traditional equivalent sound speed approach does not take into account the anisotropic nature of propagation through a flow. This can lead to significant phase errors in wide angle scenarios. Inversion algorithms which are strongly dependent on the spatial dependence of the signal phase, such as matched-field processing, will then no longer operate properly as they require a valid forward model. Furthermore, the inverse problem analysis in coastal environments must cope with the increased complexity and richness of coastal fields. One might suggest attempting to combine various measurement systems and thus increase the

performance of the overall monitoring system. Combining for instance acoustic tomography with local, moored or mobile measurement platforms could potentially lead to a system which provides the user with the large coverage of acoustic tomography as well as the high resolution of local sensors. This idea is further explored in the next section.

1.2 The Haro Strait experiment

While coastal tomography remains a topic of active research, recent developments in wireless communication technology combined with significant increases in computing power have opened the way to Acoustically Focused Oceanographic Sampling (AFOS) [71]. AFOS consists of a network of acoustic arrays connected to a fleet of Autonomous Underwater Vehicles (AUV) and to a shore station using wireless local area network technology. Non-acoustic moorings may be integrated in the network as additional nodes when available. A real-time field estimate of temperature or current in the region of interest is computed by combining the various integral and local data sets available. Integral, synoptic data is provided by the acoustic tomographic inversion while non-acoustic sensors yield local point measurements. The real-time field estimate and its associated error field are then used to adaptively direct AUVs towards regions where high resolution is required due to large gradients or large uncertainties. AFOS provides *rapid environmental assessment*, which is important for coastal oceanography and operation of naval systems.

In this context a feasibility experiment was recently performed in Haro Strait, British Columbia [4]. Its first objective was to test the available technology when integrated into a single network. Its second objective was to demonstrate the scientific relevance of AFOS by investigating mixing mechanisms in the highly active Haro strait region. Three 16-element vertical receiver arrays were moored south of Stuart Island around the location of a coastal front driven by estuarine and tidal forcing (see figure 5-1). Four non-acoustic moorings were located around the acoustic network

(see figure 5-1), measuring local current, temperature and salinity. An extensive and varied acoustic data set was generated in the course of five weeks (June-July 1996). Tomographic signals were transmitted over a wide frequency band (150Hz to 15kHz).

The novelty of the Haro Strait data set resides in its unusual tomographic features: ranges are short (less than 3 km), sound speed perturbations are small (2 to 3m/s), and currents are relatively strong (up to 5 kts). Operational constraints place stringent demands on the oceanic field estimate provided by AFOS. Its computational load must be light enough, namely of the order of a few minutes at most. The inversion must be able to withstand large environmental uncertainties as well as accomodate a wide variety of data sets. In order to satisfy the robustness constraint, classical deep ocean travel time tomography and oceanographic data assimilation techniques are combined in this thesis and adapted to the Haro Strait environment. While these techniques are not new in themselves, the combined use of interdisciplinary models and data sets in the context of coastal ocean imaging raises several issues as of yet unresolved. Resolution and parameter sensitivity of the various models for instance have been shown to be critical factors in successfully coupling oceanographic and acoustic models [47]. The possible gains from jointly extracting environmental information from integral and local data sets, while heuristically and qualitatively clear, are still hardly quantified. Furthermore, the integration of synoptic acoustic estimates with non-acoustic data sets and models in coastal environments remains a topic of active research [67, 49].

1.3   Objectives

Far from exhaustively answering the issues outlined in the previous sections, this thesis attempts to explore some aspects of both the forward and the inverse problem. The effect of current on acoustic propagation is first investigated. A tomographic inversion scheme complying with the constraints of AFOS and the Haro Strait dataset is then developed. The objectives of this thesis can be summarized as follows:

23

- *forward problem*: the goal of this section is to develop a unified analytical formulation for the equations governing propagation through a moving medium, in particular through a stratified, low-Mach number flow. The resulting computational implementation in a wavenumber integration and a modal context leads to an improved phase modeling capability. The anisotropic effect of flow on waveguide properties and propagation mechanisms will also be assessed. The feasibility of current matched-field processing will be discussed in a general context as well as in the context of the Haro Strait experiment.

- *inverse problem*: in order to draw on the strengths of the various data sets gathered in Haro Strait while coping with the high uncertainty associated with coastal environments, a hybrid linear inversion technique is developed in this section with an emphasis on water column imaging. Bottom effects are specifically ignored and filtered out of the available data set. Issues associated with combining several data sets of different origin and type in an acoustic context are explored.

- *performance analysis*: the performance of the inversion scheme previously developed is assessed in terms of expected error, resolution and bias. The relevance of frequency-coherent inversion algorithms is discussed in the context of the Haro Strait configuration.

- *experimental data analysis*: finally, the inversion scheme discussed above is applied to a portion of the Haro Strait dataset, and the results are interpreted in light of the a priori and independent information available for the Haro Strait region.

Various works relevant to the present study are summarized in the next chapter in order to provide the reader with some background information. Acoustic propagation through a stratified moving medium is investigated in chapter 3. A hybrid linear inverse framework is developed in chapter 4. The experimental setup of the Haro Strait experiment and some of the environmental data gathered during this experi-

24

ment are discussed in chapter 5. The performance of the inversion scheme previously developed is assessed in chapter 6. Finally, applications of this inversion to the Haro Strait dataset are presented in chapter 7, and conclusions are drawn in chapter 8.

Chapter 2

Background

2.1 Introduction

Acoustic propagation through a flow has long been a research focus. A great wealth of articles has been published since the end of the second world war both in atmospheric and underwater acoustics. Following advances in acoustic forward modeling capabilities, ray-based ocean acoustic tomography was formally suggested as a means of remotely sensing ocean properties about two decades ago by Munk and Wunsch [58]. Since then a significant body of work has been accomplished, proving the feasibility of ocean acoustic tomography in deep ocean environments over ranges of several hundreds of kilometers. Far from exhaustively reviewing the existing literature (a fairly complete review of tomographic works can be found in Munk et al. [57]) this chapter summarizes some of the key works relative to both the forward and the inverse problem. The following section deals with the forward problem; the inverse problem is discussed in the next section. An attempt is then made to shed some light on contemporary research issues relative to the propagation of acoustic waves through oceanic currents as well as to the ocean tomographic problem.

2.2 Propagation in a moving medium

2.2.1 Ray theory

The problem of wave propagation through a moving medium has been extensively studied in a ray-theoretic context over the past fifty years. As early as 1946 an isentropic wave equation governing propagation through an irrotational flow was derived by Blokhintsev [5]. It was then extended to the case of weak shocks, *i.e.*, pressure and velocity discontinuities, by Heller [38]. A generalized form of the Eikonal equation and Snell's law were subsequently derived by Kornhauser for stratified media. The case of an arbitrary moving and inhomogeneous medium was finally handled by Ugincius ten years later [82]. An interesting study of ray kinematics by Thompson led to a better understanding of the effect of current on ray trajectories [81]. The effective velocity along a ray was shown to be the sum of the local current vector and a vector normal to the wavefront, with magnitude equal to the local sound speed. It was also pointed out that, due to flow advection, the tangent to the ray trajectory is not strictly normal to the propagating wavefront. Various practical cases were investigated by Stallworth and Jacobson [77, 79, 78] and Franchi and Jacobson [27, 29, 28]. These studies showed the significant impact a small current fluctuation could have on the acoustic field, owing to the non-linear dependence of the wave equation on environmental conditions. Furthermore, the effect of fluid motion perpendicular to the direction of propagation was shown to be negligible in the case of a transmission across a simulated geostrophic flow. On the other hand, horizontal sound speed gradients induced by the geostrophic flow were not negligible. Propagation through actual current profiles was investigated by Sanford [68]. The strong current shears measured in the northern Sargasso sea were shown to have a significant refractive effect on propagating rays. With the emergence in the late seventies of parabolic equation techniques, the ray-theoretic approach was progressively abandoned.

2.2.2 Wavenumber integration

The wavenumber integration method, based on a spatial Fourier decomposition of the acoustic field, has been the method of choice for atmospheric acoustic propagation. Although the atmospheric literature is rich in references to the so-called windy wave equation, a few only will be mentioned here for their relevance to the underwater propagation problem. A formal wavenumber integral representation was first derived by Pridmore-Brown for the case of a temperature- and wind-stratified medium, theoretically demonstrating the existence of a shadow zone upstream of the receiver [63]. The problem of causality in the case of propagation near a flow discontinuity (vortex sheet) was pointed out by Jones and Morgan [43]. Their analysis showed that solving the wave equation in the presence a vortex sheet lead to a non-causal solution, and that if a causality constraint was applied the resulting acoustic field included an unstable, exponentionally-growing interface wave at the flow discontinuity. This problem will be discussed in chapter 3. More recently an exhaustive theoretical analysis of propagation through moving media was carried out by Brekhovskikh and Godin [7]. In particular the magnitude of the acoustic field generated by a point source in a free moving space was shown to be isotropic. This result, which is at variance with experimental results by Ingard and Singhal [41] and numerical computations by Collins et al. [14], is discussed further in chapter 3. In addition, it must be noted that all the formulations discussed above are implicit and not suitable for numerical field predictions.

2.2.3 Parabolic equation

The parabolic equation (PE) method, first introduced by Hardin and Tappert in 1973 [36], has become over the past two decades an extremely popular tool for numerical simulations. A collection of parabolic equations with different domains of validity was developed by Robertson et al. in order to study current and current shear effects [64]. Confirming ray-based studies, small currents were found to have a significant impact on shallow water propagation. Furthermore, the effect of current could be

taken into account through an equivalent sound speed profile for low-shear currents. In a subsequent study Robertson et al. showed vertical current variations could have a substantial effect in an isospeed shallow water channel [65]. Finally, azimuthal coupling was shown to be negligible in the far field when horizontal sound speed gradients are small [66]. Another PE scheme was developed by Lan and Tappert in order to study the effect of ocean currents on acoustic reciprocity [46]. Their results showed the effect of current on both travel times and amplitudes of received signals are significant and should be measurable with available measurement techniques. Finally, a generalization of the adiabatic mode parabolic equation for three-dimensional acoustic waveguides in the presence of wind was recently made by Collins et al., showing discrepancies in the literature relative to propagation in a medium with no boundary interaction (see chapter 3).

2.2.4 Normal modes

The normal mode approach did not receive much attention until the eighties, when a few studies were published in the russian literature. Mathematical expressions for the acoustic normal modes of an isospeed atmosphere with a non-uniform wind profile were first derived by Chunchuzov [13]. The case of an atmospheric waveguide with linear wind and sound speed profiles was later studied by Ostashev [59]. A more general formulation was developed by Grigor'eva and Yavor and applied to a practical oceanic waveguide [33]. It was shown that, similarly to high-frequency signals in the ray-theoretic approach, small currents could have a significant impact on the transmission loss of low-frequency signal for certain source/receiver configurations. A practical numerical scheme was developed at about the same time by Porter in order to solve the modified Sturm-Liouville problem relative to propagation through moving media for the case of two-dimensional flow [62]. Porter however focused exclusively on numerically estimatting eigenvalues of the two-dimensional Sturm-Liouville problem. By contrast this thesis will derive the three-dimensional wave equation and investigate how the presence of a stratified flow influences mechanisms of propagation both in a wavenumber-integral context and a normal mode context. Finally, an

extensive normal mode formulation was recently developed by Godin as an extension of the wavenumber analysis he developed with Brekhovskikh [31, 7]. In particular the eigenvalue problem was shown to formally reduce to that of the medium at rest by using an equivalent wavenumber and an equivalent, wavenumber-dependent sound speed. This thesis will draw on some of Godin's work in order to derive explicit general expressions for the pressure field allowing numerical field predictions.

2.3 Acoustic tomography

2.3.1 Mesoscale temperature field

The effect of the oceanic mesoscale structure on ray arrival times patterns was shown early on to be measurable yet stable. In particular ray-based propagation models were found to be good predictors of the arrival structure [75, 76, 84]. This meant ray identification and therefore tomography was possible. The first experiment demonstrating the feasibility of ocean acoustic tomography was performed in 1981 by the Ocean Tomography Group [3]. An ocean mass of 300km by 300km southwest of Bermuda was mapped using 224-Hz M-sequence signals. A good agreement was found between the acoustically-derived sound speed maps and independent CTD measurements, although mapping error levels were found to be too high for oceanographic purposes [18]. A subsequent study by Mercer and Booker showed the ray paths through an evolving mesoscale perturbation were not stationary [54]. Changes in acoustic travel times were found in some cases to be non-linearly related to the sound speed perturbation, resulting in ray-fading, *i.e.*, the appearance and disappearance of some ray trajectories depending on the evolution of the mesoscale structure. Their study also showed a single source-receiver pair could yield range information relative to the mesoscale structure. This was later confirmed by Howe *et al.* in the course of the RTE83 experiment [40]. In addition, Howe showed that by using receiver arrays rather than single receivers the variance of the sound speed estimate could be substantially lowered. The range information content of acoustic tomographic signals

was further investigated by Cornuelle and Howe [16]. Due to the spatially periodic structure of ray propagation in a typical deep ocean environment, acoustic rays were found to act as a spatial high pass filter. Features of scales as small as 10km were recovered using simulated tomographic data at ranges of 600km. In order to overcome the high uncertainty associated with the traditional tomographic estimates, Cornuelle et al. suggested using moving (shipborne) receiver [17]. Numerical simulations showed the use of a moving receiver in addition to moored acoustic arrays yielded a residual sound speed variance of 1 to 5%, compared to typically 50% for the original 1981 tomography experiment.

2.3.2 Currents and tides

The development of current tomography parallels that of sound speed tomography. Whereas sound speed tomography relies on the mean travel time between a source and a receiver in the ocean, current tomography relies on the difference between upstream and downstream arrival time along a source-receiver pair. Current tomography is therefore based on reciprocal transmissions, in which sound is transmitted in both directions along a source-receiver transect. The first reciprocal transmission experiment (RTE83) was implemented in 1983 in the Atlantic Ocean west of Bermuda [40]. Upstream and downstream ray paths were found to be nearly reciprocal. A good agreement was observed between the acoustically-derived baroclinic current profiles and geostrophic velocity profiles inferred from XBT and AXBT measurements. Unlike the sound speed tomography case, adding receivers in depth was found to have no effect on the accuracy of the baroclinic and barotropic current estimates, as the estimated sound speed error was larger than the a priori current error [39].

A 1981 study of tidal effects by Munk *et al.* on long range travel time variability synthesized the results of three different acoustic experiments performed at ranges varying from 300km to 900km [56]. Although the interpretation of tidal fluctuations was found to be varied and complex, Munk suggested these fluctuations could be used to monitor deep-sea tides. Actual tidal tomographic measurements however

were not peformed until the 1987 Reciprocal Tomography Experiment, the results of which were analyzed by Dushaw [22]. Tidal constituents were computed using acoustic data from 1000-km transmissions across the central North Pacific Ocean. The acoustic tidal estimates were found to be in good agreement with those computed using current meter data and tidal models. A similar study by Headrick *et al.* showed tidal signals could be successfully extracted from 4000-km transmissions in the Pacific Ocean between Oahu and California [37]. Finally, analysis of Gulf Stream tomographic data by Chester *et al.* confirmed the unique capabilities of acoustic tomography for measuring the relative vorticity of eddy fields as well as eddy energy, Reynolds stresses and vorticity spectra [9].

2.3.3 Coastal techniques

While acoustic tomography in deep ocean environments is now well-established, its application to coastal environments raises environmental as well as signal processing issues. The spatial and temporal scales in coastal environments are substantially smaller than that of the deep ocean, therefore increasing the complexity of the acoustic signal as well as its variability. The nature of acoustic propagation itself changes as bottom effects become paramount. In shallow water waveguides ray arrivals tends to cluster and overlap one another. Ray identification becomes significantly more challenging owing to this overlap as well as to poorly modeled bottom effects. Acoustic transmissions across the Florida Straits were analyzed by DeFerrari [21]. The ranges involved were approximately 25 to 45 km; the ocean waveguide was approximately 500-m deep. Arrival overlapping was dealt with by tracking the envelope of ray clusters instead of individual rays. The envelope arrival time was then used to infer the average temperature (one-way transmissions) and the average current (two-way transmissions) across the acoustic propagation path. A fairly good agreement was observed with local non-acoustic measurements. Using the same data set, Ko *et al.* subsequently computed estimates of the current vorticity in this region [45].

More recently a formal tomographic scheme specifically dedicated to coastal environment, Coastal Acoustic Tomography (CAT), was developed by Chiu et al. [11, 12]. In order to overcome the problem of arrival overlapping, CAT uses vertical arrays providing some arrival angle information. It then combines modal arrival times as well as beamformed ray arrival times in the tomographic inversion. This scheme was recently applied during the Barents Sea Polar Front experiment. Low frequency signals were transmitted in a shallow, 200-m deep waveguide across a strong front at a range of about 30 km. The resulting range-depth tomographic maps were found to be in good agreement with concomitant CTD measurements [60].

Finally, acoustic scintillation was recently presented by Crawford *et al.* as a method for acoustically measuring currents over short ranges (less than 2km) [20]. By estimating the cross-correlation between two nearby receivers, the magnitude of the flow perpendicular to the direction of propagation can be measured. The experimental feasibility of this concept was demonstrated by Farmer and Crawford using a 67-kHz source across a 700-m long well stirred tidal channel, and by Menemenlis and Farmer using a 172-kHz source over a distance of 200 m under the arctic ice cap [24, 25, 53].

2.4 Conclusion

While ray-based acoustic tomography has demonstrated its feasibility in the deep ocean, its applicability to shallow water waveguides remains problematic. High frequency transmissions become less deterministic due to the small scale variability of coastal regions. Ray tracing is then highly sensitive to initial conditions. Low frequency transmissions on the other hand are known to yield robust results in shallow water environments. But the full wave field must be modelled as diffraction effects become non-negligible, i.e. propagation may take a strong modal character. These constraints lead to two different approaches to coastal tomography. The first approach is that taken by Chiu *et al.*; as shallow water propagation exhibits both a ray-like and a modal behavior, ray and mode arrival times are combined in order to increase the

amount of information taken into account by the inversion. Furthermore the inclusion of both rays and modes allows the tomographic scheme to capture equally important mechanisms of acoustic propagation through shallow water waveguides. The second approach, although theoretical and unproven in shallow water environments, uses Matched-Field Processing (MFP) techniques in order to recover the environmental information buried in the acoustic signal. Being a full field method, MFP has the potential to yield high-resolution estimates although its use has been limited so far by limitations of the available forward models as well as limitations of the available a priori environmental information relative for instance to bottom properties.

Regardless of the relative merits of the two approaches, both assume an accurate forward model of shallow water propagation is available. As discussed in the first section of this chapter, the mechanisms of propagation through a moving medium are still only partially understood. Insofar as currents effects in the Haro Strait experiment might in some cases be as strong as temperatures effects, this aspect of the forward problem demands further investigation. It must be noted that whereas numerical simulations of propagation through a current can be reasonably well handled by ray-based and parabolic equation codes today, neither is satisfactory for shallow water environments. Diffraction effects are completely ignored by ray models. Parabolic equation codes on the other hand might yield reasonable field predictions, but at the expense of not comprehending the mechanism of propagation analytically, depriving us of a powerful interpretative tool. In addition, parabolic simulations need to be compared to other computations in order to ensure their validity. The modal approach on the other hand seems extremely promising in spite of its difficulty. If valid assumptions can be made in the case of ocean acoustics, the modal formalism will lead to a deeper understanding of sound advection by currents and thus to more efficient inversion algorithms.

In addition to the challenges raised by the forward problem, inverse techniques have limitations of their own when applied to coastal environments. Deep ocean

techniques become inadequate as the nature of propagation and its variability change significantly. Some inversion schemes such as CAT have produced encouraging results when applied to actual data. However, modern coastal tomography techniques are still very computationally intensive. The temporally evolving nature of the ocean is generally not taken into account; the water mass is assumed to be frozen in time at the time of propagation and past data is usually only indirectly taken into account in the inversion. Other data sets acquired at the same time are not used in the inversion, thereby forgoing the opportunity to exploit complementarity between different datasets. As discussed in chapter 1, this thesis proposes to explore some of these issues, both for the forward and the inverse problem.

Chapter 3

Forward propagation through a stratified moving medium

3.1 Introduction

A shallow water high frequency tomography experiment was conducted in Haro Strait (British Columbia, Canada) [72] in June 1996. Its goal was to demonstrate the feasibility of real-time acoustic imaging of a tidal front, for which salinity and temperature effects can be of the same order of magnitude as current effects. A numerically accurate forward model is then required in order to develop any realistic inversion scheme. The purpose of this chapter is to generalize the existing medium-at-rest wavenumber integration and normal mode approaches [42] to the case of a low Mach number, stratified flow within a single formulation directly related to measurable or computable quantities. This leads to a modified eigenvalue problem which can be solved numerically by a simple modification of the code KRAKEN [61]. The modified wavenumber integration scheme amounts to an equally simple modification of SAFARI/OASES [69]. A modal closed-form solution based on the medium-at-rest mode set is then derived assuming adiabatic propagation (no current-induced mode coupling). These results are subsequently applied to simple scenarios for low and high frequency sources. Acoustic fields computed by KRAKEN and OASES are compared to one another. Their agreement with the closed-form solution is then

discussed. Finally, assuming full knowledge of the acoustic waveguide, the feasibility of a matched-field current tomographic inversion for a realistic environment is investigated.

3.2 Analysis

3.2.1 The wave equation

The wave equation for a point source in a stationary layered medium can be expressed, using classical tensor notation, as [7] (p119):

$$\rho \frac{\partial}{\partial x_j}\left(\frac{1}{\rho}\frac{\partial p(\mathbf{x},t)}{\partial x_j}\right) - \frac{1}{c^2}\left(\frac{\partial}{\partial t} + U_j\frac{\partial}{\partial x_j}\right)^2 p(\mathbf{x},t) + 2\rho\frac{dU_j}{dx_3}\frac{\partial u_3}{\partial x_j} = -S(t)\delta(\mathbf{x} - \mathbf{x_s}) \quad (3.1)$$

where U and u are the local hydrodynamic and acoustic flow velocities. Environmental range dependence is implicitly neglected throughout this paper unless otherwise stated. The hydrodynamic flow is assumed to be incompressible ($\nabla \cdot \mathbf{U} = 0$), stratified ($\mathbf{U} \cdot \hat{\mathbf{z}} = 0$) and depends on depth only. Current shear may be arbitrarily large. Taking the Fourier transform of (3.1) with respect to time then leads to the modified Helmholtz equation :

$$[\rho\frac{\partial}{\partial x_j}(\frac{1}{\rho}\frac{\partial}{\partial x_j}) + k^2 + 2ik\mathcal{M}_j\frac{\partial}{\partial x_j} - 2i\frac{\partial}{\partial x_j}(\frac{\mathcal{M}_l}{k})\frac{\partial^2}{\partial x_l\partial x_j}]p(\mathbf{x},\omega) = -S(\omega)\delta(\mathbf{x} - \mathbf{x_s})$$

$$(3.2)$$

where the Mach number $\mathcal{M} = U/c$ is assumed to be small and terms of order $\mathcal{M}^2$ and higher are neglected. The acoustic velocity was expressed to a first order approximation as a function of ∇p. The term in $\mathcal{M} \cdot \nabla$ represents convective transport of the acoustic wave and usually is the dominant flow-related term. The second term in $\mathcal{M}$ becomes significant at low frequencies when the current profile exhibits sharp variations over distances of the order of a wavelength.

37

The terms in $\mathcal{M}$ in (3.2) can equally be thought of as source terms. In this case, assuming the pressure field is the sum of a perturbation and a mean field, the solution to (3.2) could be written as the three-dimensional convolution of a Green's function with the three source terms expressed using the mean field [55]. This approach is however limited by the fact that, as range increases, so does the pressure perturbation and one can then expect the small perturbation assumption to break down for $kr\mathcal{M} > 1$.

Transforming (3.2) into cylindrical coordinates (r, θ, z), the derivatives with respect to θ account for azimuthal coupling. These terms are however of order at least $1/kr$ compared to other flow-related terms and were shown to be negligible in the far field in the absence of strong horizontal sound speed gradients [28, 66, 48]. Consequently, (3.2) can be rewritten for a given azimuth as :

$$[\frac{1}{r}\frac{\partial}{\partial r}(r\frac{\partial}{\partial r}) + \rho\frac{\partial}{\partial z}(\frac{1}{\rho}\frac{\partial}{\partial z}) + k^2 + 2ik\mathcal{M}\frac{\partial}{\partial r} - 2i\frac{d}{dz}(\frac{\mathcal{M}}{k})\frac{\partial^2}{\partial r\partial z}]p(r, z, \omega) =$$

$$-S(\omega)\frac{\delta(r)}{r}\delta(z - z_s) \tag{3.3}$$

where $\mathcal{M}$ is from now on the projected Mach number $U\cos\theta/c$. Thus the inherently 3D problem of acoustic propagation through a moving medium can be reduced to a series of 2D problems corresponding to different azimuths for low Mach number, stratified flows.

3.2.2 Wavenumber integration representation

Azimuthal coupling being neglected, the 2D propagation problem can be interpreted as that of acoustic propagation through a perfectly symmetric waveguide. The total acoustic field can then be decomposed into a sum conical waves using the

Hankel transform defined as :

$$p(k_r, z, \omega) = \int_0^\infty p(r, z, \omega) J_o(k_r r) r dr \qquad (3.4)$$

Combining (3.3) and (3.4) yields the following modified depth-separated wave equation :

$$[\rho \frac{d}{dz}(\frac{1}{\rho}\frac{d}{dz}) + k^2 - k_r^2 - 2k_r k\mathcal{M} + 2k_r \frac{d}{dz}(\frac{\mathcal{M}}{k})\frac{d}{dz}]p(k_r, z, \omega) = -S(\omega)\delta(z - z_s) \qquad (3.5)$$

The first term in $\mathcal{M}$ accounts for current-induced refraction. The second term represents the effect of shear stress or equivalently vorticity. While the former is almost always the dominant flow-related term, the latter may under certain circumstances become non-negligible. The ratio of shear over current can be represented by the *shear number* ζ [65]:

$$\zeta = \frac{1}{k}max(\frac{1}{U}\frac{dU}{dz}) = \frac{1}{kL} \qquad (3.6)$$

For deep water, the length scale L is typically 100m [68]. This means the shear term can be neglected above 20Hz. For shallow water L may be as small as 10m [65], making the shear term negligible above 200Hz. Below this limit, shear may be neglected for long range propagation insofar as the vertical wavenumber is small, i.e., for low grazing angles. The limit frequency is then given by $c \sin \theta_c/L$ where θ_c is the grazing angle of interest.

Assuming the current profile $\mathcal{M}(z)$ is *piecewise constant* with respect to z, the derivative of $\mathcal{M}$ with respect to z vanishes almost everywhere. Equation (3.5) therefore becomes identical to the classical depth-separated equation [42] provided the sound speed profile is replaced by the following wavenumber-dependent equivalent sound speed profile :

$$\tilde{c}(z) = \frac{c(z)}{1 - \frac{k_r}{k(z)}\mathcal{M}(z)} \qquad (3.7)$$

39

In contrast to previous expressions for an effective sound speed [65, 6], we take here into account the anisotropic nature of propagation, do not require that any derivative of the current profile be known and do not require any current-dependent mapping of the depth variable. Singularities arising between constant current layers are handled through the boundary condition, i.e., by imposing continuity of pressure and continuity of the modified particle displacement [62, 6] :

$$\tilde{w}(z) = \frac{w(z)}{(1 - \frac{k_r}{k(z)}\mathcal{M}(z))^2} \tag{3.8}$$

The presence of current shear can therefore be taken into account by discretizing the waveguide into isocurrent layers whose thickness is small compared to the acoustic wavelength. The current discontinuity arising between layers is known to introduce additional poles in the complex k_r plane [43] at the approximate location $(1 \pm i)k/\mathcal{M}$ (for small $\mathcal{M}$). Its effect on acoustic reciprocity is briefly discussed in section 3.2.4. When the traditional integration contour is considered (upper half plane), the presence of these poles makes the resulting acoustic field non-causal. This lack of causality can be seen as the effect of having a pole *above* the real axis. In the case of a Pekeris waveguide for instance poles corresponding to leaky modes are displaced slightly above the real axis, breaking in a much more dramatic fashion the causality of the field. This effect is important for receivers located in the near field (for a discussion of attenuation effects on causality, see [83, 30]). In the far field however this lack of causality has no visible effect on the modelled signal. It will thus be ignored in the rest of this paper. The approach presented here is numerically convenient as its implementation requires a very simple modification of a wavenumber-integration code such as OASES.

3.2.3 Normal mode representation

Ignoring the branch line contribution the pressure field can be decomposed as the following sum of normal modes (in matrix notation) [42]:

$$p(r, z, \omega) = \boldsymbol{\psi}^T(z)\mathbf{h}(r) \tag{3.9}$$

where $\mathbf{h}$ is the projection of p on $\boldsymbol{\psi}(z)$, and $\boldsymbol{\psi}(z)$ is the medium-at-rest mode set associated with the eigenvalue problem :

$$[\rho\frac{d}{dz}(\frac{1}{\rho}\frac{d}{dz}) + k^2]\boldsymbol{\psi} = \Lambda\boldsymbol{\psi}$$

with the normalization condition :

$$\int_0^D \frac{1}{\rho}\boldsymbol{\psi}(z)\boldsymbol{\psi}^T(z)dz = \mathbf{I}$$

where $\mathbf{I}$ is the identity matrix. Λ is a diagonal matrix whose elements are the modal eigenvalues k_{rn}^2. Equations (3.3) and (3.9) can then be recombined as (see appendix) :

$$[\frac{1}{r}\frac{d}{dr}(r\frac{d}{dr}) + 2i\mathbf{K}\frac{d}{dr} + \Lambda]\mathbf{h}(r) = -\frac{S(\omega)}{\rho(z_s)}\frac{\delta(r)}{r}\boldsymbol{\psi}(z_s) \tag{3.10}$$

where the current coupling matrix $\mathbf{K}$ is defined as :

$$\mathbf{K} = [\kappa_{mn}] = \int_0^D \frac{1}{\rho}k\mathcal{M}\boldsymbol{\psi}\boldsymbol{\psi}^T dz - \int_0^D \frac{1}{\rho}\frac{d}{dz}(\frac{\mathcal{M}}{k})\frac{d\boldsymbol{\psi}}{dz}\boldsymbol{\psi}^T dz$$

Equation (3.10) is similar in many respects to that recently derived by Collins [14]. The first term in $\mathbf{K}$ is hermitian and accounts for current-induced refraction. The second term explicitly accounts for the presence of shear in the flow. Their relative importance is characterized by the shear number ζ. In some cases the current profile is smooth enough and $\mathbf{K}$ can be considered diagonal. Propagation is then adiabatic and a closed-form solution for p can be derived as shown in the next section. In

general however off-diagonal elements of $\mathbf{K}$ do not vanish. This mode coupling can be induced by either current-based refraction (first term in $\mathbf{K}$) or shear stress (second term). Equation (3.10) in this case is a set of fully coupled equations. In order to decouple them, one could try to diagonalize $\mathbf{K}$ and reformulate (3.10) in the eigenbasis of $\mathbf{K}$. This would however introduce coupling in Λ, which unfortunately has a different set of eigenvectors.

Assuming shear stress is negligible, i.e., for small shear numbers, the difficulty outlined above can be circumvented by using a modified mode set. Current-induced refraction is then taken into account in the mode set by solving the following eigenvalue problem :

$$[\rho\frac{d}{dz}(\frac{1}{\rho}\frac{d}{dz}) + k^2]\psi = (\Lambda + 2k\mathcal{M}\Lambda^{1/2})\psi \tag{3.11}$$

The normalization condition becomes :

$$\int_0^D \frac{1}{\rho}\psi(z)\psi^T(z)dz = \mathbf{J}, \tag{3.12}$$

$$[J]_{mn} = \begin{cases} 1 & \text{if } m = n \\ -2\int_0^D \frac{1}{\rho}\frac{k\mathcal{M}}{k_{rn}+k_{rm}}\psi_n\psi_m dz & \text{if } m \neq n \end{cases}$$

Thus the modified mode set is no longer orthogonal. As shown below this however has a limited impact on the approximate representation of the field. The main features of the effect of current are captured by the modified set of eigenvalues for small Mach numbers. Combining (3.11) with (3.3) and (3.9) then leads to the following modified modal equation :

$$[\mathbf{J}\frac{1}{r}\frac{d}{dr}(r\frac{d}{dr}) + 2i\mathbf{K}\frac{d}{dr} + 2\Lambda^{1/2}\mathbf{K} + \Lambda\mathbf{J}]\mathbf{h}(r) = -\frac{S(\omega)}{\rho(z_s)}\frac{\delta(r)}{r}\psi(z_s) \tag{3.13}$$

where $\mathbf{K}$ accounts for refraction only and is thus hermitian. This equation is satisfied in the far field by the medium-at-rest solution :

$$h_n(r) \simeq \sqrt{\frac{2}{\pi}} e^{-i\pi/4} S(\omega) \frac{\psi_n(z_s)}{\rho(z_s)} \frac{e^{ik_{rn}r}}{\sqrt{k_{rn}r}} \qquad (3.14)$$

where ψ_n and k_{rn} are solution to the eigenvalue problem (3.11). The accuracy of (3.14) is of order $\mathcal{M}/kr$. The contribution of off-diagonal terms in $\mathbf{J}$ is of order $\mathcal{M}/(kr)^2$. The eigenvalue problem stated in (3.11) can be numerically solved by a code such as KRAKEN, simply by replacing k_r^2 in the code by $k_r^2 + 2k_r k\mathcal{M}$ and by using the modified boundary condition stated in section 3.2.2. The pressure field is then obtained by summing up modes as one would do for a medium at rest. This solution is compared to the wavenumber integration approach in section 3.3.

3.2.4 Adiabatic mode solution

Equation (3.10) can be conveniently reformulated in the wavenumber domain as :

$$(k_r^2 \mathbf{I} + 2k_r \mathbf{K} - \Lambda)\mathbf{h}(k_r) = \frac{S(\omega)}{\rho(z_s)}\psi(z_s) \qquad (3.15)$$

where $\mathbf{h}(k_r)$ is the transform of $\mathbf{h}(r)$. The current coupling matrix $\mathbf{K}$ includes again both the effect of current refraction and current shear. The solution to this equation is :

$$\mathbf{h}(k_r) = \frac{S(\omega)}{\rho(z_s)}(k_r^2 \mathbf{I} + 2k_r \mathbf{K} - \Lambda)^{-1}\psi(z_s) \qquad (3.16)$$

The matrix inversion can be performed analytically if terms of order $\mathbf{K}^2$ and higher are negligible, i.e., for low Mach numbers and low to moderate shear ($\zeta \leq 1$). A first-order coupled-mode expression for p can then be derived. However, this procedure appears to be numerically unstable and remains a topic of current research. In some cases the current profile is smooth enough with respect to depth so that mode-coupling can be neglected (*adiabatic propagation*) and $\mathbf{K}$ becomes diagonal. The wavenumber

domain pressure $\mathbf{h}(k_r)$ can then be simplified and its components become :

$$h_n(k_r) = \frac{S(\omega)}{\rho(z_s)} \frac{\psi_n(z_s)\psi_n(z)}{(k_r + \kappa_{nn})^2 - k_{rn}^2} \tag{3.17}$$

In this form it becomes apparent that the effect of current is to shift poles of the Green's function by κ_{nn} in the complex k_r plane. This pole translation is a fundamental property of moving waveguides which does not depend on adiabaticity. In the adiabatic case the translation is parallel to the real axis and can be characterized by a simple expression. This shift is the very reason acoustic reciprocity is broken, as poles are no longer symmetric with respect to the imaginary axis (see figure 3-1). When current discontinuities are present additional poles appear on the right half-plane as pointed out in section 3.2.2, making the asymmetry even stronger.

In order to compare (3.16) with results previously found in the literature, let us assume that the coupling matrix $\mathbf{K}$ is diagonal, $i.e.$, the current profile is approximately constant. Substituting the inverse Hankel transform of (3.16) in (3.9) leads then to :

$$p(r, z, \omega) = \frac{iS(\omega)}{4\rho(z_s)} \sum_n \psi_n(z_s)\psi_n(z)H_o^{(1)}((k_{rn} - \kappa_{nn})r) \tag{3.18}$$

If $\mathcal{M}$ is constant this expression becomes identical to that derived by Schmidt and Kuperman for a source and receiver moving at the same speed in a medium at rest [73]. Bearing in mind that mode coupling is neglected, the previous result can be generalized to the case of weakly range-dependent flows $\mathcal{M}(r, z)$:

$$p(r, z, \omega) = \frac{iS(\omega)}{4\rho(z_s)} \sum_n \psi_n(z_s)\psi_n(z) \times H_o^{(1)}(k_{rn}r - \int_0^r \kappa_{nn}(r')dr') \tag{3.19}$$

The notion of weak range dependence is voluntarily left undefined as a precise validity statement for the heuristic expression above lies beyond the scope of this thesis.

Hence in the case where mode-coupling can be neglected, the effect of an arbitrary range-independent stratified current profile is modelled by a simple modal wavenum-
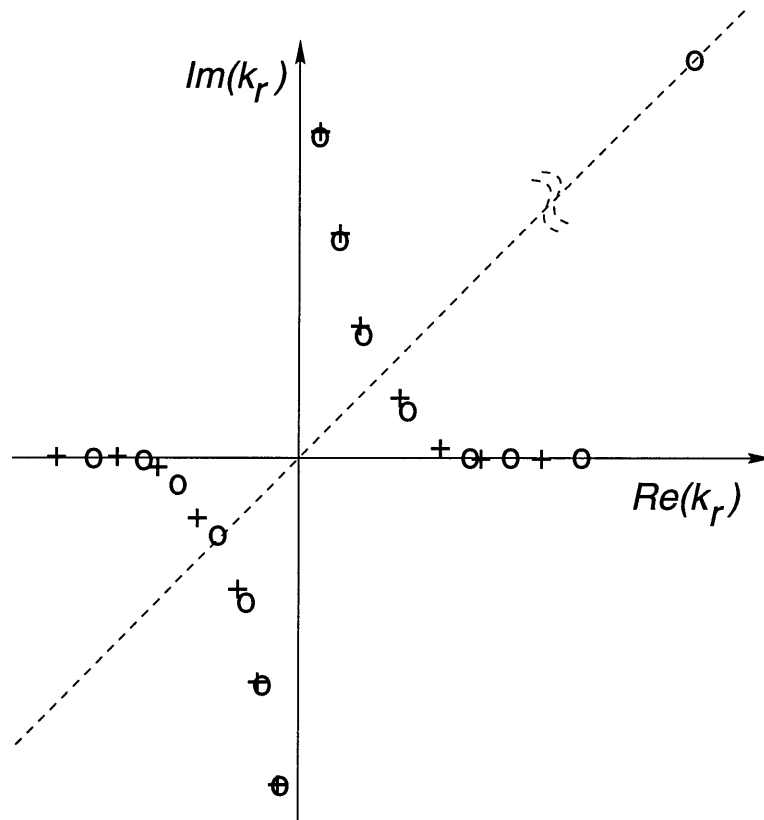
Figure 3-1: Complex plane of modal wavenumbers. Crosses: roots in the absence of current. Circles: roots in the presence of current for the same environment. Dotted line: first diagonal (Re(k) = Im(k))
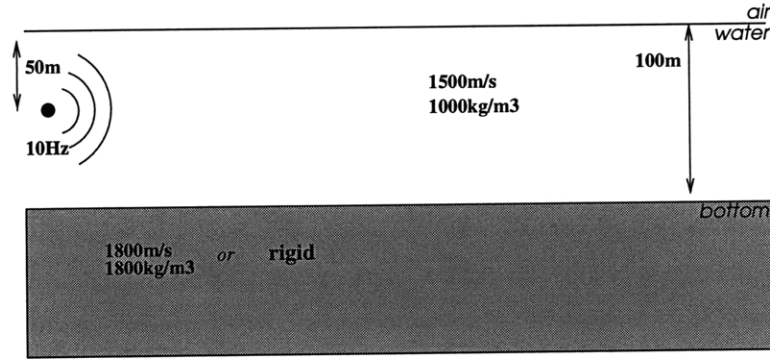
Figure 3-2: Shallow water waveguide with a uniform current of 100m/s in the water column. Two kinds of bottoms were considered : rigid and fluid.

ber shift. Having computed the normal modes $\{\psi_n\}$ with a code such as KRAKEN [61] the coefficients $\{\kappa_{nn}\}$ can be straightforwardly evaluated and included in sum (3.18), yielding an adiabatic estimate of the acoustic pressure field in the presence of a stratified flow. However, as shown in the next section, this result is limited to smooth current profiles and no bottom penetration.

3.3   Numerical results

Practical applications of the wavenumber and normal mode representations are presented below for two simple isovelocity waveguides. Versions of KRAKEN and OASES modified as indicated in the previous section are compared for a low frequency scenario. A high frequency source for a similar environment is subsequently considered. In both cases the validity of the closed-form solution outlined in section 3.2.4 is discussed. A simple application to matched-field current tomography is then presented.

3.3.1   Low frequency case

Rigid bottom   The case of a 10Hz omnidirectional source in a rigid bottom waveguide with a uniform current in the water column is considered here (see figure 3-2). An unrealistic current speed of 100m/s is chosen here in order to emphasize the

qualitative features of the acoustic field. A single mode is propagating in the water column. As no energy is exchanged with the bottom, this is somewhat akin to a cylindrical wave propagating in free space. As shown on figure 3-3 the current-modified versions of KRAKEN and OASES as well as the modal closed-form solution agree to within 1dB beyond 1km in range both upstream and downstream. The acoustic field is, for all practical purposes, axisymmetric as shown figure 3-4. This result is at variance with previous experimental measurements by Ingard and Singhal [41], as well as with numerical simulations recently performed by Collins [14]. On the other hand figures 3-3 and 3-4 are in agreement with Godin's result for a spherical wave in free space [7]. Ingard and Singhal's result is based on single mode propagation through a duct. A careful examination of their analysis shows shear effects near the duct boundaries were completely ignored in spite of their physical relevance. Their measurements showing asymmetry between upstream and downstream propagation appears, in light of the present analysis, to be due to these strong shear effects taking place at the surface of the duct. Following discussions between Collins and the author of this thesis, the parabolic equation computations of the former were shown to be biased due to an energy conservation problem and now agree with figures 3-3 and 3-4 [15]. Consequently, the magnitude of the acoustic field generated by a point source in a uniform flow in the absence of boundary interaction is isotropic, i.e. azimuthally symmetric. This of course does not apply to the phase of the acoustic field.

Signals received 5km upstream and downstream at the same depth (50m) were computed using OASES and are shown figure 3-5. The difference in arrival times matches the theoretical value of 0.4s. Amplitudes are identical, as expected from figure 3-4.

Fluid bottom   The same source is now placed in a waveguide of identical dimensions with a fluid bottom (see figure 3-2). The outputs of KRAKEN and OASES are compared in figure 3-6 and show very good agreement with each other, whereas a large discrepancy with the closed-form solution can be noted. Although no azimuthal
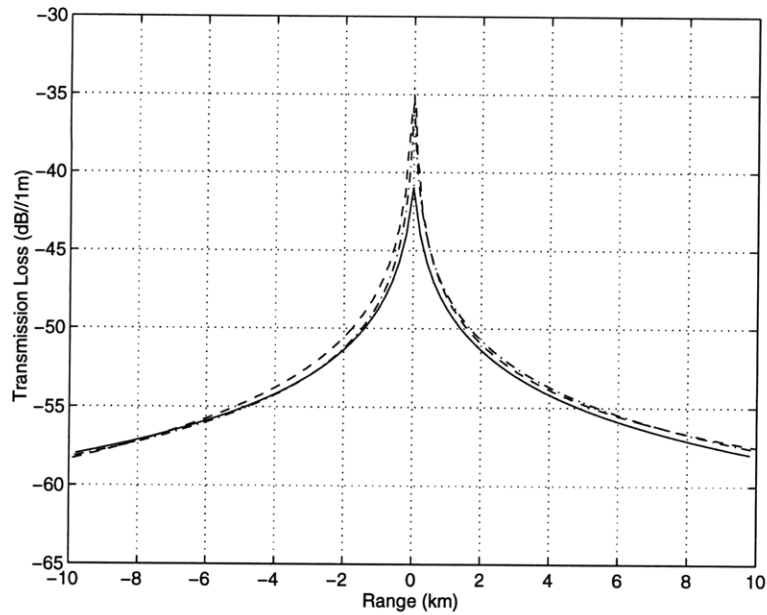
Figure 3-3: Transmission loss vs range for a 10Hz source in a free/rigid waveguide with a uniform current (100m/s) flowing towards positive ranges. Solid line : KRAKEN. Dashed line : OASES. Dash-dotted line : closed-form solution.
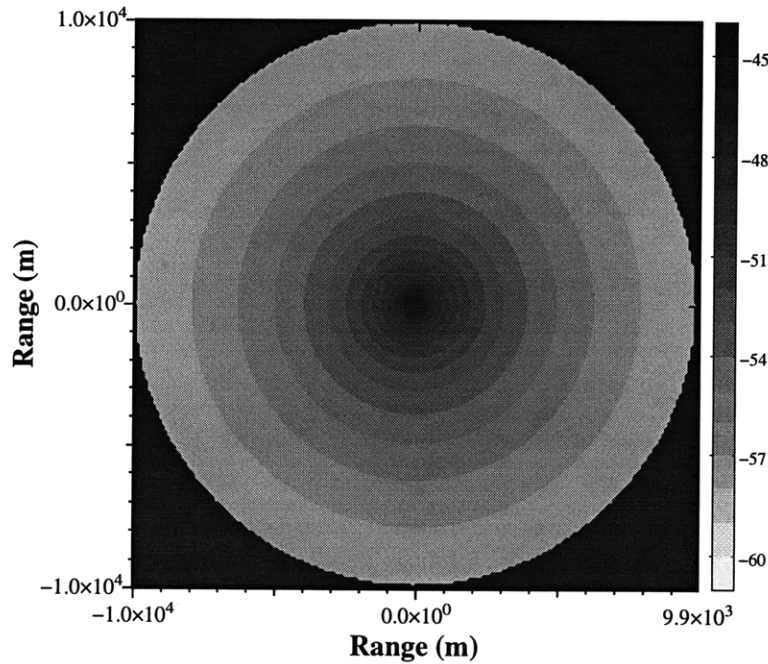
Figure 3-4: Transmission loss vs azimuth for a 10Hz source in a free/rigid waveguide with a uniform current (100m/s) flowing eastwards. Receiver depth : 50m.
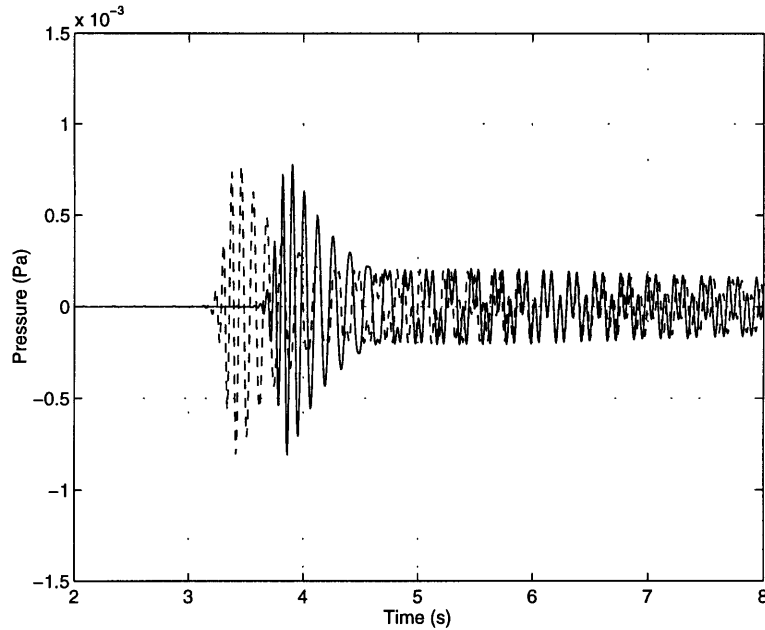
Figure 3-5: Received signal for a source signal of bandwidth 20Hz and center frequency 10Hz. in a free/rigid waveguide with a uniform current (100m/s). Receiver depth : 50m. Receiver range : 5km. Solid line : receiver is upstream. Dotted line : receiver is downstream

coupling was taken into account, the nature of the bottom has a clear impact on the azimuthal dependence of the acoustic field. In particular the bottom reflection coefficient is going to be lower downstream due to a decreased equivalent sound speed contrast at the interface, resulting in a higher level of energy transmitted in the bottom and a larger transmission loss in the water column. The transmission loss pattern in the horizontal plane is dictated by this mechanism (see figure 3-7). This furthermore provides an interpretation of the failure of the closed-form solution to match KRAKEN and OASES's result : based on the medium-at-rest mode set, this solution merely shifts modal wavenumbers by a certain amount and does not take into account changes in the bottom reflection coefficient.

Similarly to the rigid bottom case, time arrivals are shifted by roughly half a second (see figure 3-8). As expected from figure 3-7 the upstream signal is stronger. It is preceded by a head wave, which reaches the receiver at the same time regardless of the direction of propagation since the bottom is azimuthally symmetric.

49
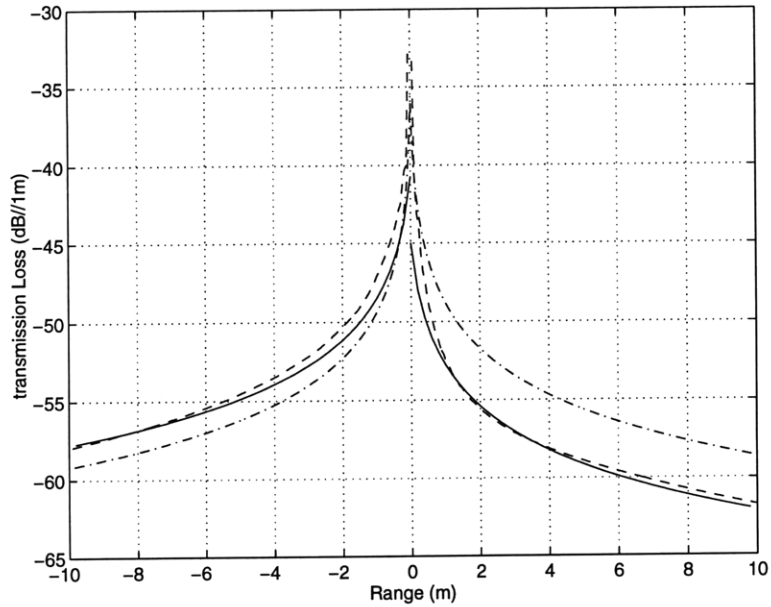
Figure 3-6: Transmission loss vs range for a 10Hz source in a free/fluid waveguide with a uniform current (100m/s) flowing towards positive ranges. Full line : KRAKEN. Dashed line : OASES. Dash-dotted line : closed-form solution
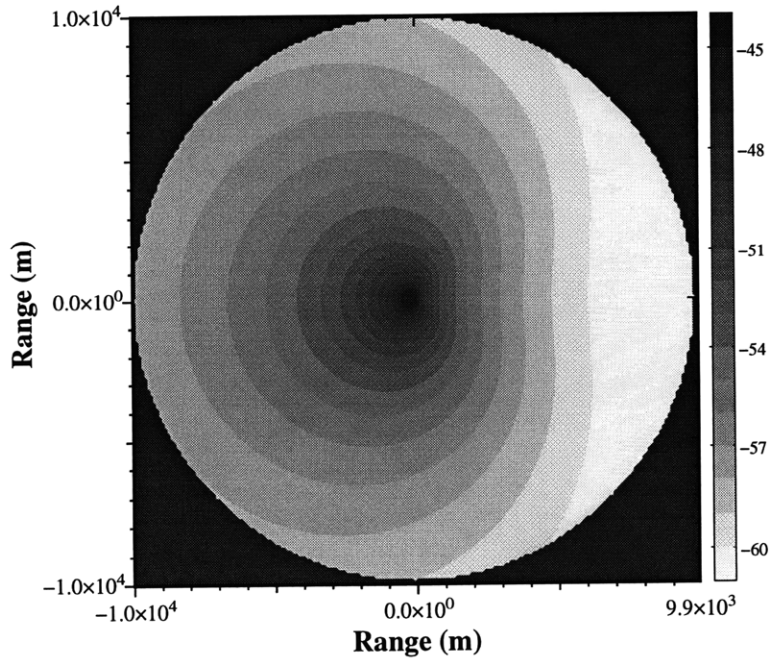
Figure 3-7: Transmission loss vs azimuth for for a 10Hz source in a free/fluid waveguide with a uniform current (100m/s) flowing eastwards. Receiver depth : 50m.

50
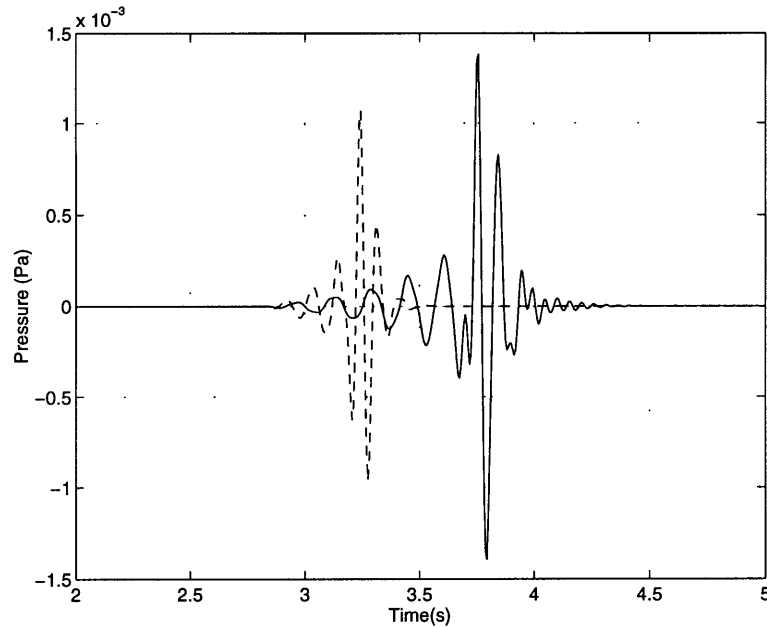
Figure 3-8: Received signal for a source signal of bandwidth 20Hz and center frequency 10Hz. in a free/fluid waveguide with a uniform current (100m/s). Receiver depth : 50m. Receiver range : 5km. Solid line : receiver is upstream. Dotted line : receiver is downstream

3.3.2 High frequency case

The high frequency shallow water environment considered in this section is shown in figure 3-9. Its features are very similar to that of the Haro Strait tomography experiment (British Columbia, Canada) [72]. Upwelling however is explicitly neglected. The current magnitude is chosen ten times larger than its actual value in order to emphasize qualitative features of the acoustic field. The time-domain output of a vertical line array spanning the entire water column was computed separately by KRAKEN and OASES. The corresponding synthetic I/Q demodulated time series shown in figures 3-10 and 3-11 exhibit a remarkable agreement. The array range is 2km. The bottom is at a depth of 225m. The different types of wave predicted by Jones and Morgan [43] are present as outlined on figure 3-10 : a primary wave in the non-moving layer (45 to 225m), various specularly reflected waves, a transmitted wave in the moving layer (0 to 45m) and a head wave linking the transmitted and direct waves. The gray scale is in Pascals. No unstable interface wave is present since we

51

did not impose any causality constraint. Numerical noise caused by wrap-around is absent of the OASES output as a complex frequency was used in the Fourier synthesis [42].

The modal closed-form solution output is plotted in figure 3-12 and shows a strong discrepancy with the previous numerical solutions. The transmitted wave and the head wave have vanished. In addition the whole primary wave front is shifted slightly towards earlier arrivals. This stems from the fact that the wavenumber shift κ_{nn} is proportional to the current velocity integrated over the entire water column. The current profile being sharp enough to break the orthogonality of the medium-at-rest mode set, the current coupling matrix $\mathbf{K}$ in equation (3.10) can no longer be considered diagonal. It is worth noticing that this coupling depends on the current profile and not its magnitude, which can be factored out. In other words the pertinent variable from an acoustic perspective is not the current magnitude but its length scale L as defined in section 3.2.2. More generally, current effects are averaged over the entire water column in the adiabatic approach and mode shapes remain those of the medium at rest. It is then impossible to observe any transmitted or head wave regardless of the current magnitude, because the adiabatic representation is fundamentally unsuited to describe the relevant propagation mechanisms.

An important consequence of this result is that if the medium-at-rest mode set is to be used, e.g. for tomographic purposes, the propagation cannot be considered adiabatic. Modes are then inherently coupled through $\mathbf{K}$ and expression (3.16) must be used. In terms of computational efficiency this makes the forward as well as the inverse problem at least one order of magnitude more intensive.

3.3.3 Matched-field current tomography

Reciprocal matched-field current tomography can be simulated as described in [42] using the model developed in this paper. Two vertical receiver arrays are moored 2km apart and consist of 32 elements equally spaced along a cable spanning the upper 100m
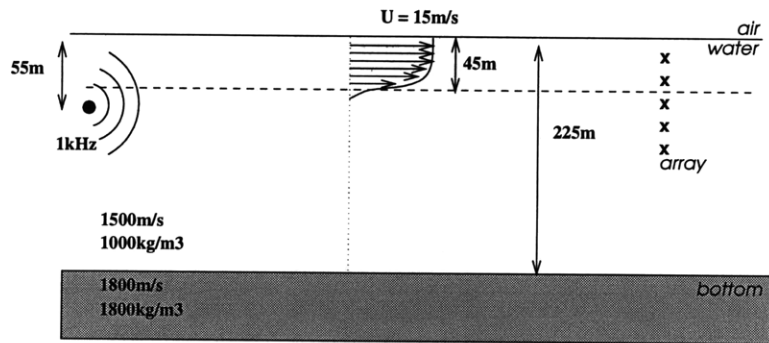
Figure 3-9: High frequency shallow water waveguide with a uniform current (15m/s) in the upper 45m. The transition zone is 10m deep (40 to 50m).
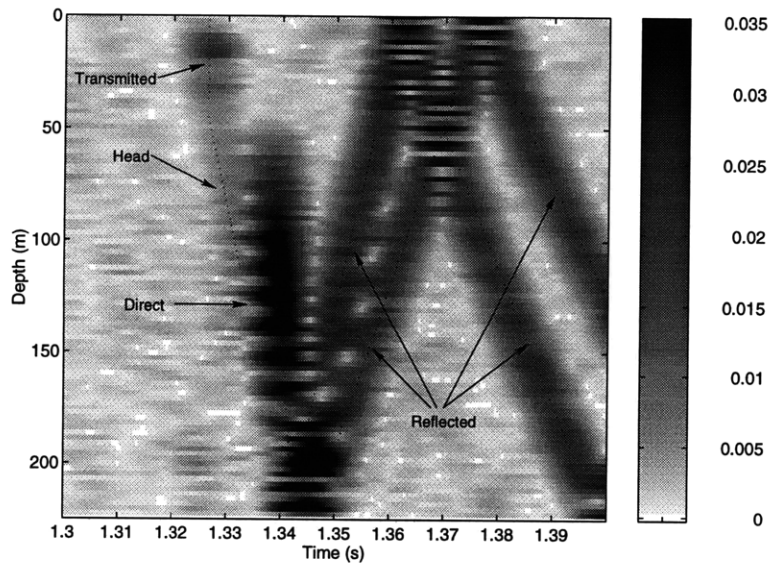
Figure 3-10: KRAKEN synthetic data : signal received at 2km for a 1kHz source of bandwidth 200Hz in a free/fluid waveguide with a uniform current (15m/s) in the upper 45m. The transition zone is 10m deep (40 to 50m).
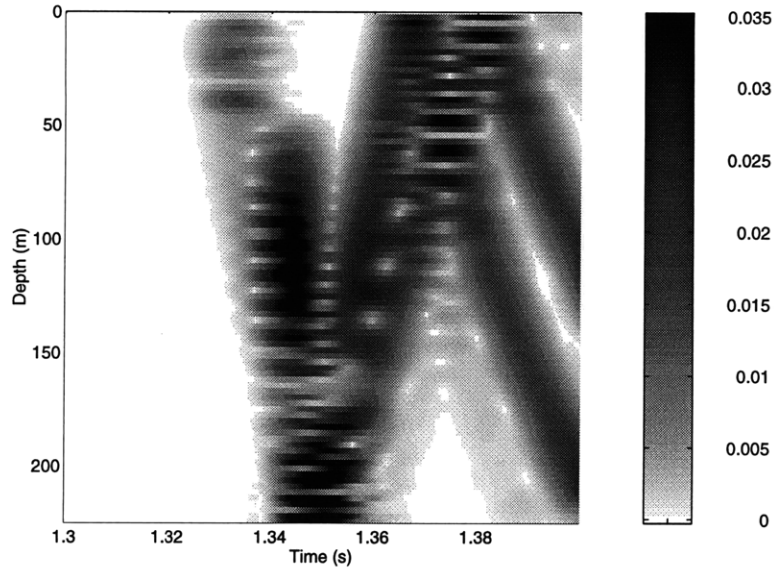
Figure 3-11: OASES synthetic data : signal received at 2km for a 1kHz source of bandwidth 200Hz in a free/fluid waveguide with a uniform current (15m/s) in the upper 45m. The transition zone is 10m deep (40 to 50m).
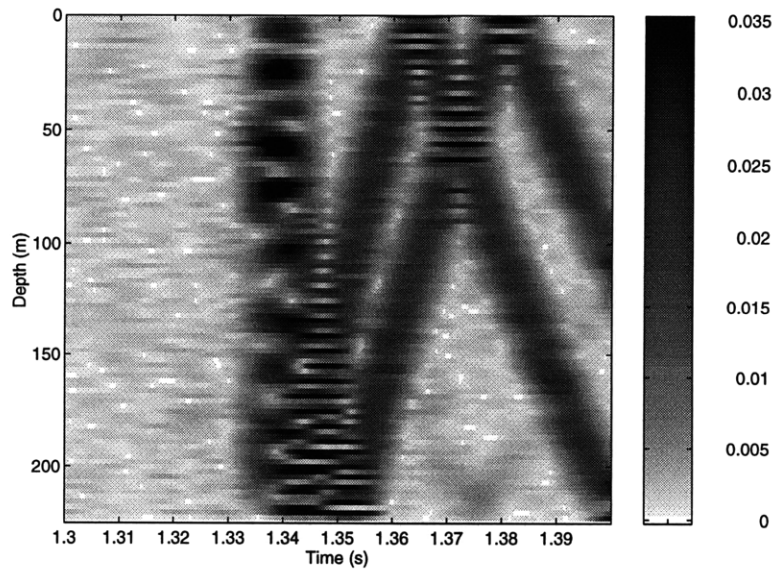
Figure 3-12: Closed-form solution synthetic data : signal received at 2km for a 1kHz source of bandwidth 200Hz in a free/fluid waveguide with a uniform current (15m/s) in the upper 45m. The transition zone is 10m deep (40 to 50m).

54

of the water column (similar to the high frequency scenario, see figure 3-9). A 55m-deep source on each array transmits a CW signal at 8 different frequencies equally spaced from 200 to 250Hz. The source level is 120 dB re $1\mu Pa$. Both sources transmit alternately so that reciprocal transmissions are available for the eight frequency bins. Replicas of the channel response function are generated by KRAKEN for various current velocities and various current layer depths. Each replica is then subtracted from its reciprocal counterpart, so that the quantity matched is the *coherent difference* in acoustic pressure between upstream and downstream propagation.

The true current layer extends from 0 to 45m. The actual transition zone goes from 40 to 50m. Current shear can then be neglected as argued in section 3.2.2. The true current magnitude is 1.5m/s and the true current depth is 45m for MFP purposes. The corresponding broadband ambiguity surface, generated using a minimum-variance beamformer, is the frequency average of the output in decibels of an MLM beamformer [1](see fig. 3-13). The true current velocity and current layer depth can be resolved with an accuracy of +/-0.1 m/s and +/-5 m, respectively. The depth resolution is limited by the smooth transition zone from 40 to 50m where the true current goes from 1.5m/s to 0m/s. The width of the main lobe is extremely narrow considering that the Mach number is very small (0.001).

Environmental mismatches are known to dramatically decrease the performance of MLM beamformers [35]. This is due to the fact that the MLM main lobe is extremely narrow at high signal-to-noise ratios, making this beamformer highly sensitive to any parameter offset. Bartlett beamformers on the other hand have a good mismatch tolerance at the expense of an increase in main lobe width. In the case of current tomography, the Bartlett main lobe is so wide that no current inversion is possible. Since the MLM beamformer degenerates into a Bartlett beamformer at low signal-to-noise ratios, artificially increasing the level of noise in the data provides the means of controlling the MLM mainlobe width. By increasing the noise level we are effectively destroying information, degrading the array gain but also decreasing the sensitivity
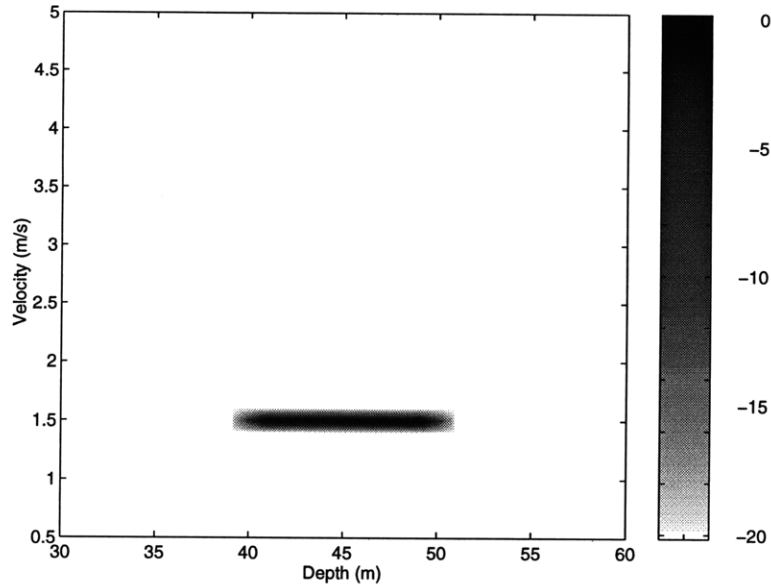
Figure 3-13: Ambiguity surface for a vertical 32-element receiver array (dB scale). Receiver range : 2km. Source frequency : 200-250kHz. Current velocity : 1.5m/s. Current layer depth : 45m. MLM beamformer. White noise level : -50dB.

to mismatch while achieving a controllable main lobe width. The ambiguity surface for a white noise level of 40dB is shown in figure 3-14. The velocity resolution is expectedly somewhat lower than that of the no noise case (about +/-0.2m/s). The depth resolution remains unchanged. The same ambiguity surface is shown in figure 3-15 in the case of a range mismatch of 2m and a bottom mismatch of 25m/s. The range mismatch corresponds to an error of 1.3ms in travel time assuming a high frequency range positioning device is available. The main lobe level is 5dB lower than in the no mismatch case, and the -8dB ambiguity ridge is only 3dB below, making the inversion less accurate. Adding more noise to the data would broaden the main lobe, making it even less distinguishible from the -8dB ridge. Less noise on the other hand would lower the main lobe further below.

Shallow water current tomography appears to be an achievable goal provided accurate information about the medium is available. This result is at variance with Godin's result for the deep ocean case [32]. Godin considered a 50Hz CW signal with

56
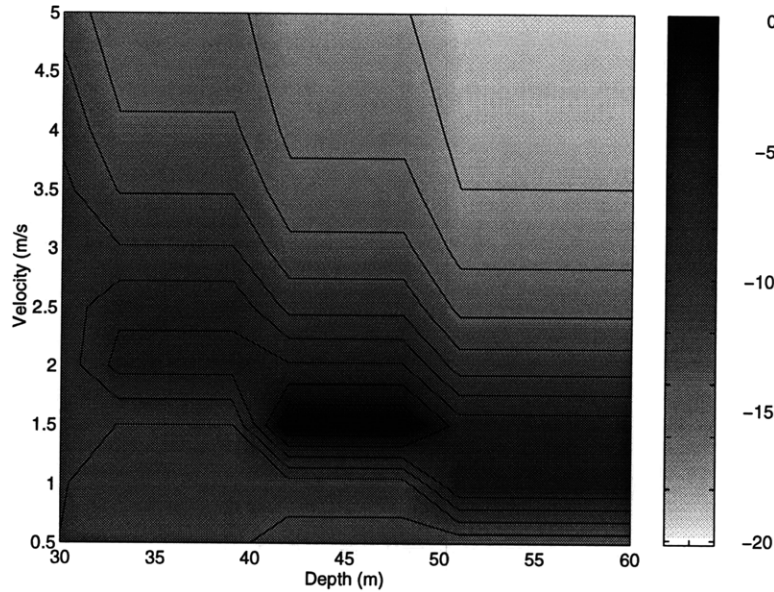
Figure 3-14: Ambiguity surface for a vertical 32-element receiver array (dB scale). Receiver range : 2km. Source frequency : 200-250kHz. Current velocity : 1.5m/s. Current layer depth : 45m. MLM beamformer. White noise level : +40dB. Contour lines are 2dB apart. Main lobe level : 0dB.

a range mismatch close to one wavelength and showed that reciprocal matched-field tomography was not feasible if mismatches were present. The present paper however assumes the source is broadband (200–250Hz) and the range mismatch is only one third of a wavelength. Furthermore we use an MLM beamformer where Godin simply looked at the normalized difference between the actual and the synthetic field.

3.4 Conclusion

The classical depth-separated and modal equations have been modified to account for the effect of a low Mach number, horizontal, depth varying current profile. It has been demonstrated that these equations can be solved by making minor modifications of existing wavenumber integration and normal mode codes. Numerical results for low and high frequency sources in a simple waveguide show a high degree of agreement between the two solutions, and confirm previous theoretical results [43, 7, 73]. An
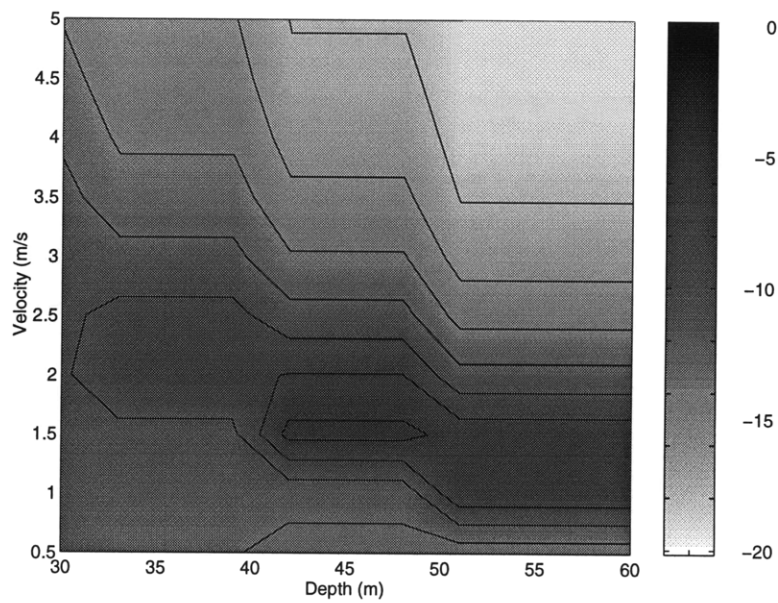
Figure 3-15: Ambiguity surface for a vertical 32-element receiver array (dB scale). Receiver range : 2km. Source frequency : 200-250kHz. Current velocity : 1.5m/s. Current layer depth : 45m. Range mismatch : 2m. Bottom sound speed mismatch : 25m/s. MLM beamformer. White noise level : +40dB. Contour lines are 2dB apart. Main lobe level : -5dB.

analytical solution was also derived based on the mode set of the medium at rest. In so doing the waveguide propagation was however assumed to occur adiabatically. Comparison with the numerical model presented in this paper shows this assumption breaks down if there is bottom penetration or if the current profile exhibits sharp variations with respect to depth. The theoretical feasibility of reciprocal matched-field current tomography is then demonstrated. Assuming accurate knowledge of the acoustic waveguide, a current velocity of 1.5m/s can be measured at a range of 2km with a resolution of 0.2m/s using a multi-tone CW signal spanning 200–250Hz.

Chapter 4

Inverse problem analysis

4.1 Introduction

Although reciprocal coherent matched-field processing was suggested in the pre-
vious chapter as a theoretically feasible inversion scheme for the Haro Strait envi-
ronment, practical and experimental constraints have led to the development of an
inversion scheme along substantially different lines. In order to reliably model acous-
tic propagation in the actual Haro Strait environment, direct and surface ray arrival
times were extracted from the data set. The purpose of this analysis being water
column imaging, bottom effects were altogether filtered out and ignored. In order
to draw on the strengths of the various data sets available the inversion combines
acoustic and non-acoustic data. The resulting field estimate can then be thought of
as the best picture which can be produced in real time *given the uncertainty and the
nature of the available data*. The data sets available in Haro Strait were of two kinds:
acoustic data was provided by the three acoustic moorings deployed around the area;
non-acoustic data was provided by two current and temperature sensor arrays located
at two corners of the area surveyed. The inversion scheme presented in this chapter
takes advantage of these two different data sets. A more complete description of the
Haro Strait experiment will be given in chapter 5.

The inversion strategy can be summarized as follows: local current-meter measurements are combined with acoustic array shape data by objective analysis, then externally assimilated into a tidal model of the region in order to produce the current field estimate. The sound speed profiles computed by Gauss-Markov inversion of the acoustic data are subsequently combined with local non-acoustic temperature and salinity measurements through objective analysis again in order to produce the sound speed field estimate. The advantages and limitations of this approach will be discussed in chapter 6 and 7.

4.2 Preliminary results

4.2.1 Maximum-likelihood estimation

The observation model of many oceanic field estimation problems can be written as:

$$\mathbf{y} = b\mathbf{h}(\mathbf{x}) + \mathbf{n} \tag{4.1}$$

where $\mathbf{y}$ represents a vector of data points, e.g., pressure field values or ray travel times; $\mathbf{x}$ represents the oceanic field being estimated, e.g., temperature or current at different locations; and $\mathbf{n}$ represents additive noise. Although $\mathbf{n}$ is in general also a function of $\mathbf{x}$, it will be assumed here to be independent of $\mathbf{x}$ in order to make the analysis tractable. The function $\mathbf{h}$ is in general non-linear. The factor b accounts for multiplicative noise terms such as phase randomization. All four random terms are assumed to be jointly Gaussian. Individual distributions are as follows:

$$\mathbf{y} \sim N(\mathbf{y}_0, \mathbf{R}_{yy}) \tag{4.2}$$

$$b \sim N(\beta, \sigma_b^2) \tag{4.3}$$

$$\mathbf{x} \sim N(\mathbf{x}_0, \mathbf{R}_{xx}) \tag{4.4}$$

$$\mathbf{n} \sim N(0, \mathbf{R}_{nn}) \tag{4.5}$$

where $N(\mathbf{0}, \mathbf{I})$ is the standard vector normal probability density of mean $\mathbf{0}$ and covariance $\mathbf{I}$. The random variables b, $\mathbf{x}$ and $\mathbf{n}$ are further assumed to be statistically independent of one another. Using classical Bayesian analysis the maximum a posteriori estimator of $\mathbf{x}$ can be derived as:

$$\widehat{\mathbf{x}}_{ML} = \underset{\mathbf{x}}{argmax}\,[p_y(\mathbf{y}|\mathbf{x})p_x(\mathbf{x})] \tag{4.6}$$

where $p_y(.|.)$ is the probability density function of $\mathbf{y}$ conditionned on $\mathbf{x}$, and p_x is the probability density function of $\mathbf{x}$. Combining equations (4.2) to (4.6) leads to the following expression for $\widehat{\mathbf{x}}_{ML}$ (see appendix):

$$\widehat{\mathbf{x}}_{ML} = \underset{\mathbf{x}}{argmin}[(\mathbf{y} - \beta\mathbf{h}(\mathbf{x}))^{\dagger}\left(\mathbf{R}_{nn} + \sigma_b^2\mathbf{h}(\mathbf{x})\mathbf{h}(\mathbf{x})^{\dagger}\right)^{-1}(\mathbf{y} - \beta\mathbf{h}(\mathbf{x}))$$
$$+ (\mathbf{x} - \mathbf{x}_0)^{\dagger}\mathbf{R}_{xx}^{-1}(\mathbf{x} - \mathbf{x}_0)] \tag{4.7}$$

Expression (4.7) can be simplified in a number of cases.

Case 1: Travel time tomography

In the case of perturbational travel time tomography, the transfer function $\mathbf{h}(\mathbf{x})$ is linear and can be written as $\mathbf{Hx}$. The phase randomization term is assumed to be deterministic; its mean β is equal to 1 and its probability density function tends to a Dirac delta function as σ_b^2 tends to zero. Equation (4.7) then becomes:

$$\widehat{\mathbf{x}}_{ML} = \underset{\mathbf{x}}{argmin}[(\mathbf{y} - \mathbf{Hx})^{\dagger}\mathbf{R}_{nn}^{-1}(\mathbf{y} - \mathbf{Hx}) + (\mathbf{x} - \mathbf{x}_0)^{\dagger}\mathbf{R}_{xx}^{-1}(\mathbf{x} - \mathbf{x}_0)] \tag{4.8}$$

which can be solved analytically as [57]:

$$\widehat{\mathbf{x}}_{ML} = \mathbf{x}_0 + \mathbf{K}(\mathbf{y} - \mathbf{Hx_0}) \tag{4.9}$$

$$\mathbf{K} = \mathbf{R}_{xx}\mathbf{H}^{\dagger}\left(\mathbf{HR}_{xx}\mathbf{H}^{\dagger} + \mathbf{R}_{nn}\right)^{-1} \tag{4.10}$$

and the error covariance matrix of the estimate $\widehat{\mathbf{x}}_{ML}$ is:

$$\mathbf{P}_x = (\mathbf{I} - \mathbf{K}\mathbf{H})\,\mathbf{R}_{xx} \tag{4.11}$$

Case 2: Matched-Field Tomography

In the case of Matched-Field Tomography the transfer function $\mathbf{h}(\mathbf{x})$ represents the Green's function of a given source-receiver pair, and is strictly non-linear. The phase randomization term is zero-mean, i.e., β is equal to zero. The model vector $\mathbf{x}$ is now assumed to be a unknown, non-random parameter. Its inverse covariance matrix therefore tends to zero. In scalar terms the variance of $\mathbf{x}$ tends to infinity as no a priori information is available. Equation (4.7) becomes then:

$$\widehat{\mathbf{x}}_{ML} = \underset{\mathbf{x}}{argmin}\left[\mathbf{y}^\dagger \left(\mathbf{R}_{nn} + \sigma_b^2 \mathbf{h}(\mathbf{x})\mathbf{h}(\mathbf{x})^\dagger\right)^{-1} \mathbf{y}\right] \tag{4.12}$$

As $\mathbf{h}$ is strictly non-linear, $\widehat{\mathbf{x}}_{ML}$ is likely to be biased and its variance will not be minimal. For these reasons $\widehat{\mathbf{x}}_{ML}$ is replaced in practice by its so-called minimum-variance counterpart:

$$\widehat{\mathbf{x}}_{MV} = \underset{\mathbf{x}}{argmin}\left[\mathbf{h}(\mathbf{x})^\dagger \left(\mathbf{R}_{nn} + \sigma_b^2 \mathbf{h}(\mathbf{x}_0)\mathbf{h}(\mathbf{x}_0)^\dagger\right)^{-1} \mathbf{h}(\mathbf{x})\right] \tag{4.13}$$

which can be derived in a linear systems context [1]. The minimum variance estimator is a valid estimator, i.e., it does not require prior knowledge of $\mathbf{x}_0$, as the covariance matrix $[\mathbf{R}_{nn} + \sigma_b^2 \mathbf{h}(\mathbf{x}_0)\mathbf{h}(\mathbf{x}_0)]$ is estimated using the data $\mathbf{y}$.

4.2.2 General inverse formulation

Oceanic fields such as temperature and current are estimated using a priori as well as a posteriori information. A posteriori information refers to measurements made locally or globally, using intrusive as well as remote-sensing techniques. The data thus gathered can be related to the field being estimated through an *observation model*. Although this observation model is often non-linear, e.g., the Matched-Field

63

Tomography case, it may be cast in a linear form under certain circumstances, namely in the cases of local field measurements and perturbational travel time tomography. Equation (4.1) then becomes:

$$\mathbf{y} = \mathbf{Hx} + \mathbf{n} \tag{4.14}$$

This system of equations may include several types of data measured at different locations in space and time. A priori information about the field $\mathbf{x}$ is provided by a statistical characterization of $\mathbf{x}$, $\mathbf{y}$ and $\mathbf{n}$, and by the state model:

$$\mathcal{B}\mathbf{x} = \mathbf{f} \tag{4.15}$$

where the operator $\mathcal{B}$ relates the forcings and boundary conditions $\mathbf{f}$ imposed on a given oceanic region to the field $\mathbf{x}$ being estimated. In some cases, e.g., using a finite-difference scheme, (4.15) can be cast in a linear form and subsequently combined with (4.14). This leads to a global linear inverse problem in which the field is estimated by interpolating the available data $\mathbf{y}$ while taking into account the statistics of the model and the data as well as the physical equations governing the evolution of the field of interest. This approach is unfortunately intractable in many cases, either because of the large size of the matrices involved, or because the physical model $\mathcal{B}$ is simply not linearizable over the space and time spans involved.

Assimilating oceanic data into models has been the object of intense research efforts by the oceanographic community over the past 15 years. Many assimilation techniques have been developed, and the reader is refered to [51, 57] for an exhaustive description of the various methods available today. For a variety of reasons discussed in Chapter 1 the present study focuses on linear melding techniques in order to combine different types of data as well as data and models when the latter are available. More specifically, the assimilation technique used in this chapter is based on *optimal interpolation* [51]. Optimal interpolation is performed in two stages:

- *Objective analysis*: the available data are combined through equation (4.14) and a data-only estimate of $\mathbf{x}$ and its associated error covariance matrix $\mathbf{P}_{xx}$ are computed using (4.9) and (4.11). In an oceanographic context, where $\mathbf{y}$ consists mostly of sparse, local measurements of $\mathbf{x}$, objective analysis is interpreted as regridding the data on a regular grid using a Gauss-Markov interpolation scheme. In a perturbational acoustic-tomographic context, objective analysis is viewed as performing the tomographic inversion itself.

- *Blending*: the data-only estimate of $\mathbf{x}$ and its theoretical prediction are linearly combined in order to produce the final field estimate. The respective weights are assigned using error estimates. This step is also refered to as *external melding*, as it does not require any additional model run making use of the data.

The following section describes the various observation models used with the Haro Strait data set. These models are the necessary components of the objective analysis stage.

4.3 Observation models

The current and temperature (sound speed) fields are probed using acoustic means, which are global in nature, or non-acoustic means, which are local in nature. Although the two types of data may appear to be fundamentally different they are only different projections of the same field being measured, namely sound speed or current. In order to be able to reconstruct the original field which generated the data set, the observation process must first be understood and modeled. An observation process typical of the Haro Strait experiment is shown in figure 4-1. Local non-acoustic probing of current and sound speed is symbolized by the two "local sampling / IOS" boxes. The observation consists simply of directly measuring sound speed and temperature at a given point in space and time, with some noise added to it. The current field is also locally measured by the acoustic array displacements. Array displacements are measured by acoustic probing, which itself also provides a global measure of the

65

sound speed and current field.

As the reader may guess the mix of local/global and acoustic/non-acoustic data eventually leads to an observation system which is non-trivial. In order to be able to combine the various data sets and estimate the original sound speed and current fields each individual part of the observation process must be carefully modeled. Three individual observation models need to be developed:

- an acoustic sensor model, relating the acoustic array displacements to the local current field perturbation.

- a current model, relating local non-acoustic current measurements to the current field perturbation. Incidentally this model will assume a form very similar to that of the local non-acoustic sound speed observation model.

- an acoustic model, relating ray travel time perturbations to the global sound speed field perturbation

Each individual observation model will also incorporate a priori knowledge in the form of first- and second-order statistical moments of both the additive observational noise and the sound speed and current fields.

4.3.1 Sensor model

The horizontal displacements of a moored line array placed in a uniform flow can be expressed as [44]:

$$\delta r = a \left[z - b \ln(1 - \frac{z}{c}) \right] \nu = af(z)\nu \tag{4.16}$$

66
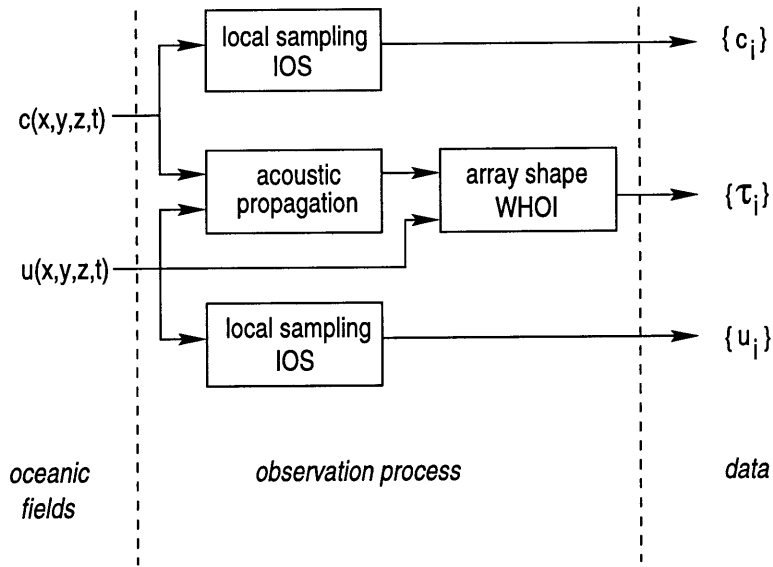
Figure 4-1: Measurement model of the sound speed and current fields through global acoustic means (WHOI) and local non-acoustic means (IOS)

where $\boldsymbol{\nu}$ is a unit vector in the direction of the flow,

$$a = \frac{d}{w} \tag{4.17}$$

$$b = \frac{D}{d} - \frac{W}{w} \tag{4.18}$$

$$c = \frac{W}{w} + L \tag{4.19}$$

and d is the cable drag per unit length, w is the cable weight per unit length, D is the drag of the subsurface buoy, W is the buoyancy of the subsurface buoy, L is the total length of the cable. The coefficients b and c are true constants which depend on the design of a given array. The coefficient a depends quadratically on current magnitude and may be more conveniently expressed as $a = \alpha U^2$, where U is the current magnitude at the location of the array. An acoustic transmission in the horizontal direction $\mathbf{p}$ will then be affected by the projection δR of the array displacements in that direction:

$$\delta R = af(z)(\boldsymbol{\nu}^T \mathbf{p}) \tag{4.20}$$

Let us now assume the uniform current $\mathbf{U}$ at the array can be decomposed into a reference state $U_o\boldsymbol{\nu}$ and a perturbation $\mathbf{u}'$. Let us further assume the term $\boldsymbol{\nu}^T\mathbf{p}$ is included in a. The coefficient a can then be expressed as:

$$a = a_o + a' = a_o + 2\alpha U_o(\boldsymbol{\nu}^T\mathbf{p})\boldsymbol{\nu}^T\mathbf{u}' \qquad (4.21)$$

where the subscript o refers to the reference state and second-order terms have been neglected. In the case of short range transmissions, an acoustic estimate $\widetilde{a}$ of a' can be easily computed by minimizing the mean square error between measured ray arrival times at the array and their theoretical value using an adequate sound speed profile (uniform or historical average) and a reference current vector $U_o\boldsymbol{\nu}$. The measured array shape perturbation can be written as:

$$\widetilde{a} = 2\alpha(\boldsymbol{\nu}^T\mathbf{p})\boldsymbol{\nu}^T\mathbf{u}' + n_a \qquad (4.22)$$

where the noise term n_a is assumed to be Gaussian. Equation (4.22) establishes a direct linear relationship between the measured value $\widetilde{a}$ and the current perturbation $\mathbf{u}'$ at the array.

4.3.2 Current model

An accurate three-dimensional, baroclinic finite-element model of tidal currents in the Haro Strait region was recently developed by Foreman et al. [26]. In order to decrease the computational load involved in predicting local currents, a two-dimensional, barotropic version of Foreman's model is used in this paper. The latter model is able to properly account for 90% of the tidal flow variance at the SW IOS mooring and 72% at the NE IOS mooring in Haro Strait (see chapter 5). For the purpose of this analysis, Foreman's model can be summarized as:

$$\mathbf{U_o} = g(\mathbf{r}, t) \qquad (4.23)$$

where $\mathbf{U_o}$ is the predicted tidal current at the location $\mathbf{r}$ at the time t. The predicted field is used throughout the analysis as the background field. The current perturbation $\tilde{\mathbf{u}}$ measured by the IOS current-meters can be related to the true value $\mathbf{u}'$ as:

$$\tilde{\mathbf{u}} = \mathbf{u}' + \mathbf{n}_{u,cm} \tag{4.24}$$

where the measurement noise vector $\mathbf{n}_{u,cm}$ is assumed to be Gaussian.

4.3.3 Acoustic model

For a given source-receiver geometry acoustic travel times perturbations τ can be related to sound speed perturbations by the following linear expression [57]:

$$\tau = \mathbf{E}\mathbf{c}' + \mathbf{n}_{u,a} \tag{4.25}$$

where the noise vector $\mathbf{n}_{u,a}$ is assumed to be Gaussian of covariance matrix $\mathbf{R}_{nn}^{(a)}$. In order to reduce the number of degrees of freedom of the original inverse problem the range-independent sound speed perturbation $\delta c(z)$ is decomposed using an arbitrary set of orthogonal functions:

$$\delta c(z) = \boldsymbol{\phi}(z)^T \mathbf{c}' \tag{4.26}$$

In the present paper the functions $\phi_j(z)$ are assumed to be "gate" functions, set to zero everywhere except within a specified depth interval $[z_j, z_{j+1}]$ where it is set to unity. These depth intervals are non-overlapping and cover the entire water column (from 0 to 200m). The matrix $\mathbf{E}$ can then be expressed as:

$$[\mathbf{E}]_{ij} = -\int_{ray\#i} \frac{\phi_j(z_i)}{c_o^2(r_i, z_i)} ds_i \tag{4.27}$$

where c_o is the background sound speed profile. The range r_i and depth z_i along the ith ray are an implicit function of the ray curvilinear abscissa s_i.

69
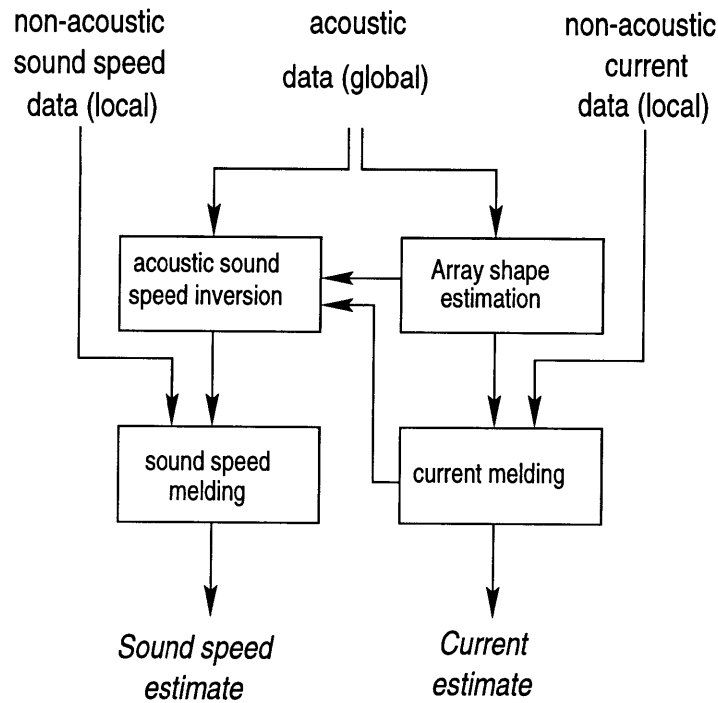
Figure 4-2: Flow chart of the current and temperature field estimation scheme

4.4   Inversion formalism

Now that relationships relating observed quantities to original fields have been derived, the different data sets available can be combined in order to produce a field estimate (see figure 4-2). In a first stage an estimate of the current field is computed by objective analysis of the available current data [8]. The current estimate is then externally melded with the tidal current model prediction following a standard data assimilation procedure. The sound speed field is then objectively analyzed using range-averaged acoustic tomographic estimates and local non-acoustic data.

4.4.1   Current inversion

Three types of information can be combined in the estimation of the current field: point measurements of current at non-acoustic moorings, array shape acoustic estimates at the acoustic moorings and a priori predictions by the tidal model. The available point measurements of current can be consolidated through equation (4.24)

as:

$$\begin{bmatrix} \widetilde{\mathbf{u}}_{x,cm} \\ \widetilde{\mathbf{u}}_{y,cm} \end{bmatrix} = \begin{bmatrix} \mathbf{I} & \mathbf{O} \\ \mathbf{O} & \mathbf{I} \end{bmatrix} \begin{bmatrix} \mathbf{u}'_{x,cm} \\ \mathbf{u}'_{y,cm} \end{bmatrix} + \begin{bmatrix} \mathbf{n}_{x,cm} \\ \mathbf{n}_{y,cm} \end{bmatrix} \tag{4.28}$$

where the x subscript refers to the east-west direction and the y subscript refers to the north-south direction. Similarly, the array shape data can be consolidated using equation (4.22) as:

$$\widetilde{\mathbf{a}} = \begin{bmatrix} \mathbf{H}_1 & \mathbf{H}_2 \end{bmatrix} \begin{bmatrix} \mathbf{u}'_{x,a} \\ \mathbf{u}'_{y,a} \end{bmatrix} + \begin{bmatrix} \mathbf{n}_{x,a} \\ \mathbf{n}_{y,a} \end{bmatrix} \tag{4.29}$$

The matrices $\mathbf{H}_1$ and $\mathbf{H}_2$ are both diagonal and

$$[\mathbf{H}_1]_{jj} = 2\alpha_j(\boldsymbol{\nu}_j^T \mathbf{p}_j)\nu_{j,x} \tag{4.30}$$

$$[\mathbf{H}_2]_{jj} = 2\alpha_j(\boldsymbol{\nu}_j^T \mathbf{p}_j)\nu_{j,y} \tag{4.31}$$

The term α_j corresponds to the shape factor α of the acoustic array involved in the jth transmission. Combining (4.28) and (4.29) leads to the global observation model of the current field:

$$\begin{bmatrix} \widetilde{\mathbf{u}}_{x,cm} \\ \widetilde{\mathbf{u}}_{y,cm} \\ \widetilde{\mathbf{a}} \end{bmatrix} = \begin{bmatrix} \mathbf{I} & \mathbf{O} & \mathbf{O} & \mathbf{O} & \mathbf{O} & \mathbf{O} \\ \mathbf{O} & \mathbf{O} & \mathbf{O} & \mathbf{I} & \mathbf{O} & \mathbf{O} \\ \mathbf{O} & \mathbf{H}_1 & \mathbf{O} & \mathbf{O} & \mathbf{H}_2 & \mathbf{O} \end{bmatrix} \begin{bmatrix} \mathbf{u}'_{x,cm} \\ \mathbf{u}'_{x,a} \\ \mathbf{u}'_{x,i} \\ \mathbf{u}'_{y,cm} \\ \mathbf{u}'_{y,a} \\ \mathbf{u}'_{y,i} \end{bmatrix} + \begin{bmatrix} \mathbf{n}_{x,cm} \\ \mathbf{n}_{x,a} \\ \mathbf{n}_{x,i} \\ \mathbf{n}_{y,cm} \\ \mathbf{n}_{y,a} \\ \mathbf{n}_{y,i} \end{bmatrix} \tag{4.32}$$

where $\mathbf{u}'_{x,i}$ and $\mathbf{u}'_{y,i}$ represent the current field perturbation interpolated at the nodes of a specified grid. Equation (4.32) can be recast in a more compact format as:

$$\widetilde{\mathbf{u}} = \mathbf{H}\mathbf{u}' + \mathbf{n}_u \tag{4.33}$$

The covariances matrices $\mathbf{R}_{uu}$ of $\widetilde{\mathbf{u}}$ and $\mathbf{R}_{nn}^{(u)}$ of $\mathbf{n}_u$ can be computed using the space-time correlation function Γ_u of the current field. The model covariance matrix in (4.33) is defined by:

$$\mathbf{R}_{uu} = E\left[\mathbf{u}'\mathbf{u}'^{T}\right] \tag{4.34}$$

where the first half of $\mathbf{u}'$ includes East-West components and the second half includes North-South components. Due to the complexity and the variability of the cross-correlation between the East-West and North-South components, each component is assumed to be uncorrelated with its counterpart. The model covariance matrix can therefore be written as:

$$\mathbf{R}_{uu} = \begin{bmatrix} \mathbf{R}_{u,x} & \mathbf{O} \\ \mathbf{O} & \mathbf{R}_{u,y} \end{bmatrix} \tag{4.35}$$

and

$$\left[\mathbf{R}_{u,x/y}\right]_{ij} = \sigma_{u,x/y}^2 \Gamma_u(\mathbf{r}_i, \mathbf{r}_j, t_i, t_j) \tag{4.36}$$

where $\mathbf{r}_i$ and t_i refer to the location in space and time of the ith node. The experimental estimation of the correlation function Γ_u and the variances $\sigma_{u,x}^2$ and $\sigma_{u,y}^2$ is discussed in the next chapter.

Similarly the noise covariance matrix $\mathbf{R}_{nn}^{(u)}$ is given by:

$$\mathbf{R}_{nn}^{(u)} = \begin{bmatrix} \widetilde{\mathbf{R}}_{u,x} & \mathbf{O} & \mathbf{R}_{au,x}^T \\ \mathbf{O} & \widetilde{\mathbf{R}}_{u,y} & \mathbf{R}_{au,y}^T \\ \mathbf{R}_{au,x} & \mathbf{R}_{au,y} & \mathbf{R}_{aa} \end{bmatrix} \tag{4.37}$$

where the matrices $\widetilde{\mathbf{R}}_{u,x/y}$ are computed using the definition of $\mathbf{R}_{u,x/y}$ with the actual measurement locations. The covariance of the array shape factors $\widetilde{a}$ with the current

72

components $u_{x/y}$ can be expressed as:

$$\mathbf{R}_{au,x} = \mathbf{H}_1 E \left[\mathbf{u}_{x,a} \mathbf{u}_x^T \right] \qquad (4.38)$$

$$\mathbf{R}_{au,y} = \mathbf{H}_2 E \left[\mathbf{u}_{y,a} \mathbf{u}_y^T \right] \qquad (4.39)$$

where $\mathbf{H}_1$ and $\mathbf{H}_2$ are given by (4.30) and (4.31) and the expectations by (4.36). For simplicity's sake the covariance of array shape factors is assumed to be:

$$\mathbf{R}_{aa} = \sigma_a^2 \mathbf{I} \qquad (4.40)$$

where the standard deviation σ_a is estimated by comparison of the array shape data with the predictions based on the tidal model (see chapter 5).

Once the covariance matrices are computed, equation (4.33) can then be inverted as [80, 57]:

$$\widehat{\mathbf{u}'} = \mathbf{K}_u \widetilde{\mathbf{u}} \qquad (4.41)$$

where the gain matrix $\mathbf{K}_u$ is given by:

$$\mathbf{K}_u = \mathbf{R}_{uu} \mathbf{H}^T \left(\mathbf{H} \mathbf{R}_{uu} \mathbf{H}^T + \mathbf{R}_{nn} \right)^{-1} \qquad (4.42)$$

The associated error covariance matrix of the current perturbation estimate is [57]:

$$\mathbf{P}_u = (\mathbf{I} - \mathbf{K}_u \mathbf{H}) \mathbf{R}_{uu} \qquad (4.43)$$

This concludes the first stage (objective analysis) of the current data assimilation procedure.

The current perturbation estimate $\mathbf{u}'$ can then be merged with the model prediction using the following melding scheme. The final field estimate at a given node $\mathbf{r}$ for a given component is asssumed to be a linear combination of the predicted field and the measured field [49]:

$$\widehat{U}(\mathbf{r}) = (1 - \lambda(\mathbf{r})) U_o(\mathbf{r}) + \lambda(\mathbf{r}) \left(U_o(\mathbf{r}) + \widehat{u}'(\mathbf{r}) \right) \tag{4.44}$$

The north/south and east/west components are melded independently of each other. Based on the statistical properties of the model and measurement errors a minimum variance estimate of λ can be derived [49]:

$$\lambda_{MV}(\mathbf{r}) = \frac{\sigma_m^2(\mathbf{r}) - \rho(\mathbf{r})\sigma_m(\mathbf{r})\sigma_d(\mathbf{r})}{\sigma_m^2(\mathbf{r}) + \sigma_d^2(\mathbf{r}) - 2\rho(\mathbf{r})\sigma_m(\mathbf{r})\sigma_d(\mathbf{r})} \tag{4.45}$$

where $\sigma_m(\mathbf{r})$ is the estimated error of the model prediction $U_o(\mathbf{r})$, $\sigma_d(\mathbf{r})$ is the error of the data-based perturbation estimate $\widehat{u}'(\mathbf{r})$, and $\rho(\mathbf{r})$ is the correlation between the two. The measurement error $\sigma_d(\mathbf{r})$ is given by the relevant diagonal term of $\mathbf{P}_u$ in equation (4.43). In the absence of an accurate error model of the current prediction made by the tidal model, the optimal interpolation scheme used by the Harvard Ocean Prediction System is adopted [51]:

$$\lambda_{OI}(\mathbf{r}) = \frac{\sigma_{max} - \sigma_d(\mathbf{r})}{\sigma_{max} - \sigma_{min}} \tag{4.46}$$

where σ_{min} and σ_{max} are the minimum and maximum values of $\sigma_d(\mathbf{r})$. The melded estimate is therefore equal to the model prediction at points where the measurement error is maximal, and is set equal to the measured estimate at point where the measurement error is minimal. The robustness of this melding scheme was demonstrated in several oceanographic data assimilation experiments [52].

4.4.2   Sound speed inversion

Two types of information can be combined in the estimation of the sound speed field: point measurements of sound speed at the non-acoustic moorings and acoustic

travel times measured at the acoustic moorings. This is done in two stages: first the acoustic travel times are used to estimate range-averaged sound speed profiles and their error covariance along the available transmission tracks. These sound speed profiles are then merged with the point measurements and interpolated in order to yield an estimate of the sound speed field.

Similarly to the current inversion, the covariance matrix $\mathbf{R}_{cc}^{(a)}$ of the sound speed perturbation in equation (4.25) can be estimated using the space-time correlation function Γ_c of the sound speed field:

$$\mathbf{R}_{cc}^{(a)} = \sigma_c^2 \Gamma_c(\mathbf{r}_i, \mathbf{r}_j, t_i, t_j) \tag{4.47}$$

where $\mathbf{r}_i$ refers to the location (depth) of the ith node of a given acoustic inversion (single shot, range-independent). The times t_i and t_j are set equal to each other since all nodes are estimated at the same time during the acoustic tomographic inversion. The standard deviation σ_c can be estimated using CTD data (see chapter 5). The acoustic noise covariance matrix $\mathbf{R}_{nn}^{(a)}$ is modeled as:

$$\mathbf{R}_{nn}^{(a)} = \left(\sigma_t^2 + \left(\frac{\sigma_{u,z}}{c_o} \frac{R}{c_o} \right)^2 \right) \mathbf{I} \tag{4.48}$$

where R is the source range and c_o a reference sound speed. The first term accounts for local travel time errors induced by residual sensor displacements or local medium variability. The second term accounts for the presence of current variations in depth along the acoustic track, which are unaccounted for in the inversion. Both standard deviations are estimated by statistical analysis of the data set available.

Equation (4.25) can then be inverted as [57]:

$$\widehat{\mathbf{c}'} = \mathbf{K}_c^{(a)} \tau \tag{4.49}$$

where the gain matrix $\mathbf{K}_c^{(a)}$ is given by:

$$\mathbf{K}_c^{(a)} = \mathbf{R}_{cc}^{(a)}\mathbf{E}^T \left(\mathbf{E}\mathbf{R}_{cc}^{(a)}\mathbf{E}^T + \mathbf{R}_{nn}^{(a)}\right)^{-1} \tag{4.50}$$

The associated error covariance matrix of the range-averaged sound speed estimate is [57]:

$$\mathbf{P}_c^{(a)} = (\mathbf{I} - \mathbf{K}_c^{(a)}\mathbf{E})\mathbf{R}_{cc}^{(a)} \tag{4.51}$$

The range-averaged sound speed estimate at a given depth z_o can be expressed as:

$$\widehat{c'}(z_o) = \int_0^1 \beta(\mathbf{r}_{src}, \mathbf{r}_{rcv}, z_o, \eta)c'(\mathbf{r}_{src} + \eta\mathbf{r}_{rcv})d\eta \tag{4.52}$$

where $\mathbf{r}_{src}$ and $\mathbf{r}_{rcv}$ are the source and receiver location, c' is the true sound speed perturbation. The weighting or ray sampling function β is given by:

$$\beta(\mathbf{r}_{src}, \mathbf{r}_{rcv}, z_o, \eta) = \beta_o \sum_i \frac{\phi_j(z_i)}{\cos\theta_i} \tag{4.53}$$

where β_o is a normalization factor such that $\beta(\eta)$ integrates to one between 0 and 1. The term ϕ_j is the orthogonal function of equation (4.27) corresponding to the depth bin z_o. The sum is performed over all rays joining the source and the array of receivers. The local ray depth z_i and the local ray grazing angle θ_i are implicit functions of η. The weighting function β is equal to 1 for a source and a receiver located at the same depth in the absence of boundary interaction. The acoustic profile estimates of several transmissions can be consolidated for a given depth as:

$$\widetilde{\mathbf{c}}_a = \mathbf{F}\mathbf{c}'_i + \mathbf{n}_{c,a} \tag{4.54}$$

76

where $\mathbf{c}'_i$ is the interpolated sound speed field on a specified grid and $\mathbf{n}_{c,a}$ represents additive gaussian noise. The matrix $\mathbf{F}$ is given by:

$$[\mathbf{F}]_{kj} = \beta(\mathbf{r}_{src}^{(k)}, \mathbf{r}_{rcv}^{(k)}, z_o, \eta_j^{(k)}) \Delta\eta_j^{(k)} \tag{4.55}$$

where $\mathbf{r}_{src}^{(k)}$ and $\mathbf{r}_{rcv}^{(k)}$ are the end points of the kth transmission, $\eta_j^{(k)}$ is the local non-dimensional range corresponding to the jth node of the global interpolated grid $\mathbf{c}_i$ and $\Delta\eta_j^{(k)}$ is the non-dimensional length of the jth cell intercepted by the ray considered.

Similarly to what was done for the current data, the sound speed perturbation $\widetilde{\mathbf{c}}$ measured by the non-acoustic moorings at various times can be related to the true perturbation $\mathbf{c}'$ as:

$$\widetilde{\mathbf{c}}_{cm} = \mathbf{c}'_{cm} + \mathbf{n}_{c,cm} \tag{4.56}$$

where the measurement noise vector $\mathbf{n}_{c,cm}$ is assumed to be Gaussian. Equation (4.54) and (4.56) can combined to yield:

$$\begin{bmatrix} \widetilde{\mathbf{c}}_{cm} \\ \widetilde{\mathbf{c}}_a \end{bmatrix} = \begin{bmatrix} \mathbf{I} & \mathbf{O} \\ \mathbf{O} & \mathbf{F} \end{bmatrix} \begin{bmatrix} \mathbf{c}'_{cm} \\ \mathbf{c}'_i \end{bmatrix} + \begin{bmatrix} \mathbf{n}_{c,cm} \\ \mathbf{n}_{c,a} \end{bmatrix} \tag{4.57}$$

which can in turn be recast in the more compact form:

$$\widetilde{\mathbf{c}} = \mathbf{G}\mathbf{c}' + \mathbf{n}_c \tag{4.58}$$

Equation (4.58) can be inverted using the method outlined for equation (4.25). The model covariance matrix $\mathbf{R}_{cc}^{(c)}$ of $\mathbf{c}'$ is defined as:

$$\left[\mathbf{R}_{cc}^{(c)}\right]_{ij} = \sigma_c^2 \Gamma_c(\mathbf{r}_i, \mathbf{r}_j, t_i, t_j)$$

where $\mathbf{r}_i$ and t_i refer to the location in space and time of the ith node of the corresponding grid. A particular attention must be paid to the covariance matrix of

$\widetilde{\mathbf{c}}$. As pointed out by Cornuelle and Worcester, the covariance matrix of acoustic sound speed estimates is often non-diagonal and significant errors can be induced by neglecting covariance terms, which is often done in oceanographic data assimilation [19] The noise covariance matrix $\mathbf{R}_{nn}^{(c)}$ used in the inversion of (4.58) is computed as:

$$\left[\mathbf{R}_{nn}^{(c)}\right] = \begin{bmatrix} \widetilde{\sigma}_c^2 \mathbf{I} & \mathbf{O} \\ \mathbf{O} & \widetilde{\mathbf{P}}_c(a) \end{bmatrix}$$

The sound speed time series standard deviation $\widetilde{\sigma}_c$ is estimated using the IOS mooring data (see chapter 5). The relevant acoustic sound speed estimate error matrices $\mathbf{P}_c^{(a)}$ given by (4.51) are aggregated in $\widetilde{\mathbf{P}}_c^{(a)}$. The present method therefore allows error correlations among different acoustic sound speed estimates of the same profile to be taken into account by simply inserting the relevant terms of $\mathbf{P}_c^{(a)}$ (equation (4.51)) into the covariance matrix of $\widetilde{\mathbf{c}}$.

In the case of the Haro Strait data set the absence of a known source transmission time made it necessary to include a global acoustic sound speed offset in the model vector $\mathbf{c}'$ in equation (4.57), as only sound speed differences across depths and tracks could be acoustically resolved. Equation (4.57) was consequently rewritten as:

$$\begin{bmatrix} \widetilde{\mathbf{c}}_{cm} \\ \widetilde{\mathbf{c}}_a \end{bmatrix} = \begin{bmatrix} \mathbf{I} & \mathbf{O} & \mathbf{0} \\ \mathbf{O} & \mathbf{F} & \mathbf{1} \end{bmatrix} \begin{bmatrix} \mathbf{c}'_{cm} \\ \mathbf{c}'_i \\ \Delta c \end{bmatrix} + \begin{bmatrix} \mathbf{n}_{c,cm} \\ \mathbf{n}_{c,a} \\ n_{\Delta c} \end{bmatrix} \tag{4.59}$$

In the absence of any accurate model of the temperature and salinity fields in Haro Strait the field estimate produced by objective analysis was taken as the final field estimate. This can alternatively be viewed as an asymptotic case of blending where the a priori variance of the predicted field is infinite and the blended estimate is equal to the objectively analyzed estimate.

4.4.3 Computational issues

A flow chart of the complete current and temperature field estimation scheme is given in figure 4-2. The acoustic sound speed profiles were first computed along each propagation track and then melded with the non-acoustic data instead of being included directly in the three-dimensional inversion for several reasons. Due to the particular experimental configuration of Haro Strait, the acoustic inversion has virtually no resolution in range for a given shot. The acoustic data provides good resolution in depth and across shot tracks. This information can be efficiently extracted by processing shots individually before the global inversion. In addition the computational load associated with a global three-dimensional inversion is of order $O(N^6)$ for a grid of dimension N^3. On the other hand the segmented three-dimensional inversion is of order $O(N^5)$ if carried out depth by depth, or even $O(N^4)$ if a single depth or a few selected depths are of interest. This decrease of the computational load by one to two orders of magnitude is critical in enabling this inversion to be performed in a few minutes (on a DEC-Alpha 3000) and then fed back to the sampling network, in particular to the moving sources and AUV's. Segmenting the sound speed in this manner also facilitates inversion quality control by enabling the operator to verify the validity of the acoustically-derived sound speed profiles prior to melding with other data sets. The computational load of the inversion is further decreased by clipping the data sets. Data points within 3 correlation depths of the desired depth and acquired during a period of 3 correlation times before the time of inversion are taken into account. Other data points are discarded. The current field estimation was made first. It was then used as background field in the sound speed estimation.

4.5 Conclusion

A hybrid linear inversion scheme was presented in this chapter. This scheme combines global (acoustic) and local (non-acoustic) measurements while taking into account the specificities of each data set. Expressions were derived for the temperature and the current field estimates as well as their expected covariance matrices. The

performance of this inversion will be assessed in chapter 6 using synthetic data.

Chapter 5

The Haro Strait experiment

5.1 Introduction

The experimental setup used in the Haro Strait experiment is described in this chapter. The data conditioning procedures applied to the data before inversion are presented for both the acoustic and the non-acoustic data. Acoustic sensor localization is then discussed. Finally the current and sound speed correlation functions are estimated for the water mass surveyed during the Haro Strait experiment.

5.2 Experimental configuration

5.2.1 Arrays

Four vertical acoustic line arrays (hereafter called WHOI moorings) were initially deployed south of Stuart island (see figures 5-1 and 5-2). The southeastern mooring, located near Danger Shoal, was lost at an early stage of the experiment because of unexpectedly strong tidal currents. Each mooring consisted of 16 receivers, a 1.5-kHz tomographic source and a 15-kHz communication source (see figure 5-3). A chain of thermistors was added to moorings NW and NE. The acoustic data acquired on each receiver array was sent back to shore via a surface radio link at a rate of 35 *kbps*.

Four non-acoustic moorings (hereafter refered to as IOS moorings) were deployed along the Haro Strait channel (see figure 5-1). Local temperature, salinity, current magnitude and current direction were recorded by these moorings at discrete depths. Only the two IOS moorings closest to the network of acoustic arrays are used in this analysis. The IOS mooring sensors were located at a depth of 25, 70 (NE only) and 120m. During the two-hour time period studied in this analysis, current magnitudes of up to 3.5 kts and temperatures variations of up to $1.5^o C$ were observed.

5.2.2 Sources

The moving source consisted of ship-deployed light bulbs. Source locations were obtained using differential GPS data, and the locations corresponding to the shots used in this analysis are shown in figure 5-2. These shots were recorded on all three moorings, and were all deployed within a time period of approximately 90 minutes. Source depths ranged from 30m to 70m. Source levels were approximately 160 to170$dB//1\mu Pa$. The light bulbs were lowered to a specified depth in the casing apparatus shown in figure 5-4. The shot was then triggered by breaking the bulb at depth using an operator-released lead mass that dropped along the cable from the ship to the casing. Light bulbs generate a short reproducible bubble pulse waveform whose spectral density is plotted in figure 5-5 for two different source depths. The source spectral density was estimated by computing the spectrum of a single direct arrival and averaging across several shots. The peak frequency is strongly dependent on the depth of the source. It varies from 400 Hz to 600 Hz as the source depth goes from 30 m to 70 m. The 6-dB bandwidth of the measured source signal is approximately 200 to 300 Hz. Although there is significant spectral content to several kHz, the band was limited in this experiment by the relatively low sampling frequency of 1750 Hz. An example of the raw acoustic signal from one of the light bulbs is shown in figure 5-6.

Predicted surface currents at 1800Z, 1/7/1996
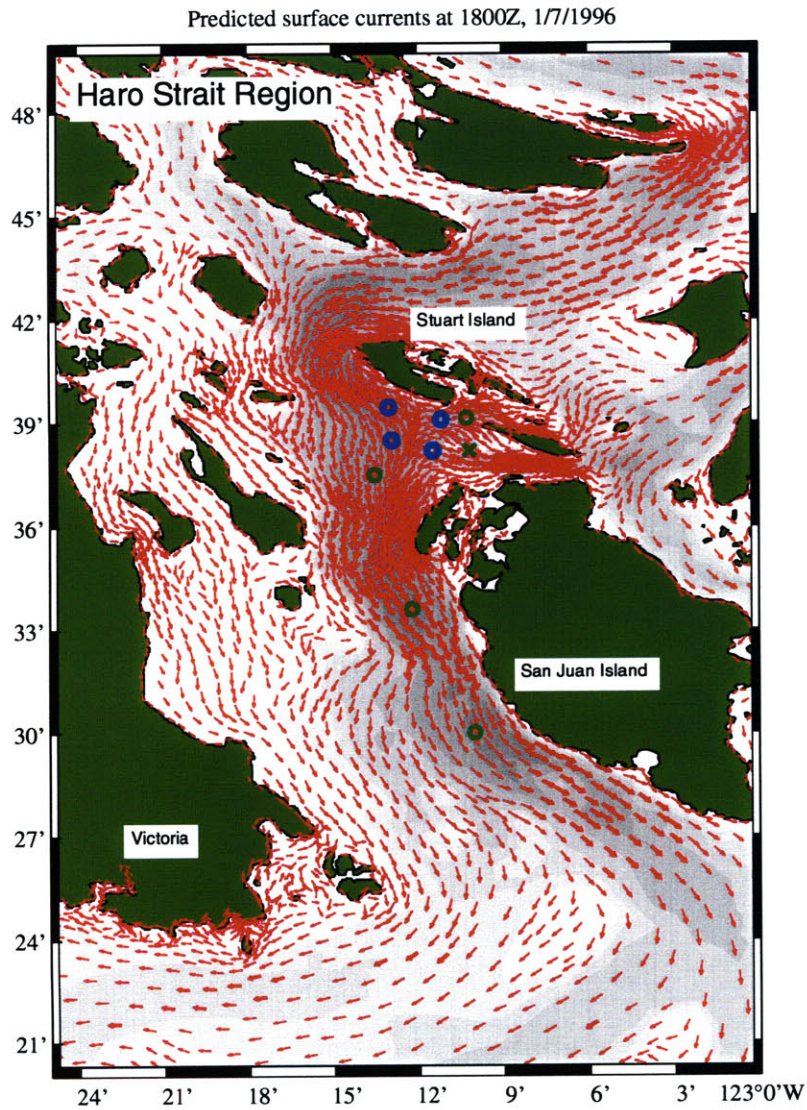
Figure 5-1: Topographic map of the Haro strait region with predicted ebb tide currents during the experiment. Tomographic arrays (blue circles) were deployed to investigate the front south of Stuart island. Current meter moorings (green circles) and a meteorological surface buoy (green cross) will help clarify the larger-scale circulation (courtesy of R.Pawlowicz, IOS).

83
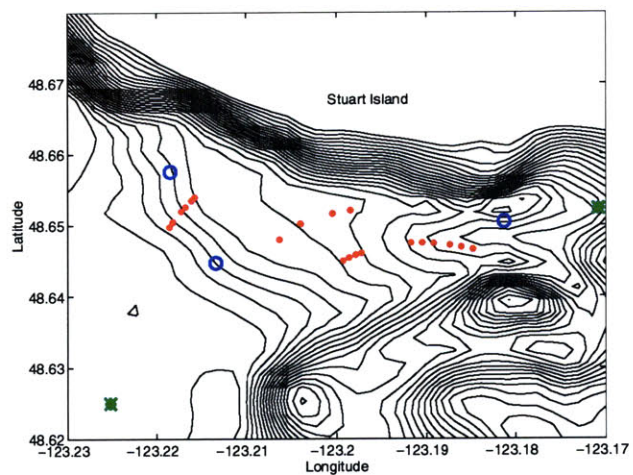
Figure 5-2: Bathymetric map of the experimental site. Contours are 10m apart. Blue circles : WHOI receiver arrays. Green starts: IOS moorings. Red dots: source locations.
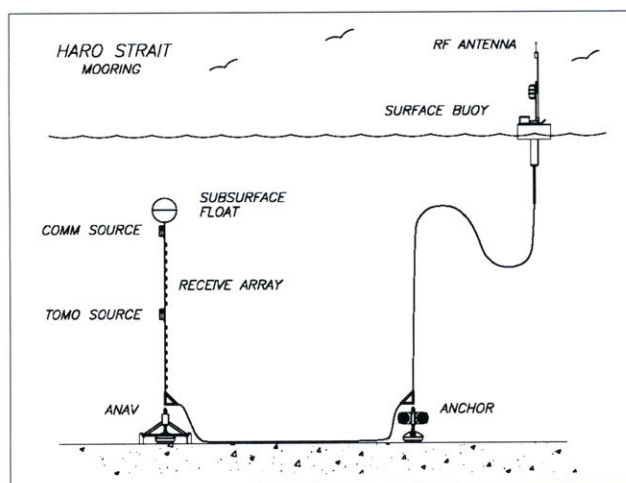
Figure 5-3: Haro strait mooring design
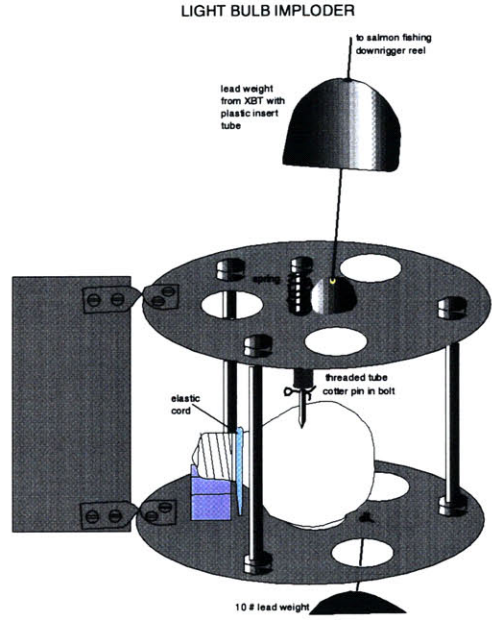
Figure 5-4: Source design (courtesy of N. Ross Chapman, University of Victoria)
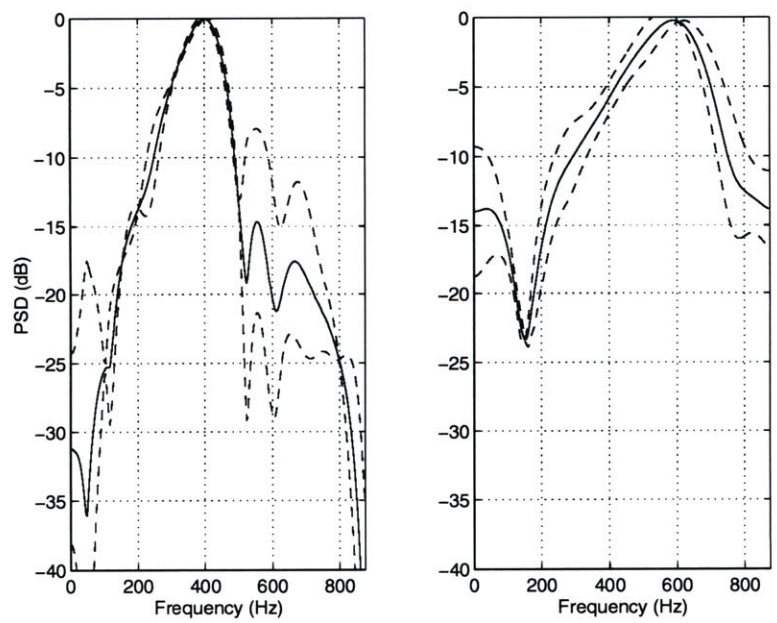
Figure 5-5: Normalized source power spectral density. Left panel: source depth of 30.5 m; right panel: source depth of 70m. Solid line: mean. Dashed line: 70% confidence interval.

5.3 Data conditioning

5.3.1 Acoustic time series

Individual acoustic time series were match-filtered using a single arrival as a substitute for the actual source signal. The magnitude of the matched filter output was then lowpass-filtered using a zero-phase third-order Butterworth filter with a cutoff frequency of 500Hz. Direct and surface ray arrival times were subsequently measured by identification of the corresponding local maxima of the filtered time series (see figure 5-7). Absolute timing was provided by the AMS-driven acoustic acquisition system [34]. A time stamp in seconds was provided with each acoustic time series. In addition, the number of time samples elapsed since the last second was also provided. The beginning t_{start} of a given time series was computed as:

$$t_{start} = t_{stamp} + f_s N + M \qquad (5.1)$$

where t_{stamp} is the time stamp in seconds, N is the number of samples elapsed since the last second, f_s is the sampling frequency, and M is an unknown integer number of seconds. The unknown M accounts for the fact that t_{stamp} is given with an accuracy of one second. The term M can therefore be -1, 0 or $1s$. This ambiguity was lifted by adding (subtracting) seconds to (of) the measured arrival times until they were consistent with an isovelocity estimate based on the a priori sensor locations.

5.3.2 Sound speed time series

Temperature and salinity time series were measured by the IOS moorings at a frequency of 12 samples per hour ($\Delta t = 5min$). These two parameters were converted to sound speed using Mackenzie's formula [50]. Individual samples were grouped by 50-minute bins and averaged (see figure 5-8). The average standard deviation of the resulting average was found to be of the order of $10cm/s$ (see table 5-1). Rms fluctuations of the time series were of the order of $50cm/s$. The vertical variability of the sound speed field was estimated using a set of CTD casts taken every day from
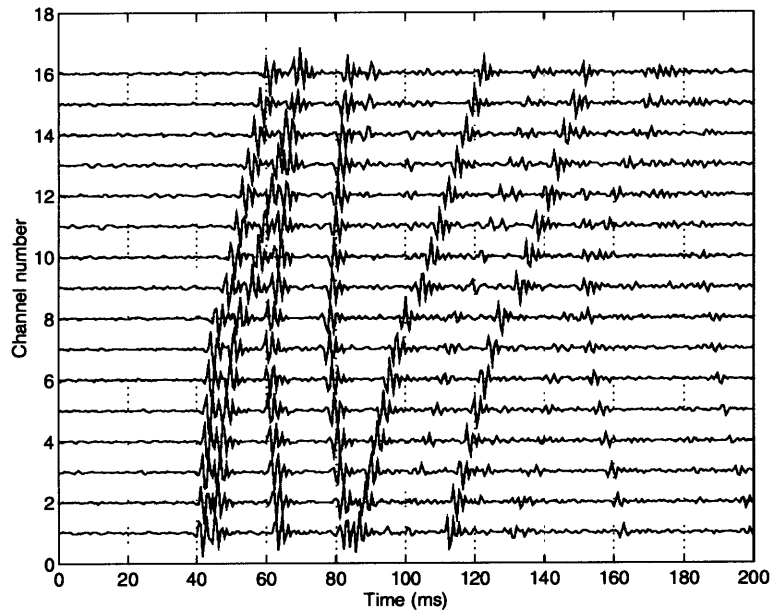
Figure 5-6: Raw time series : shot 32, 06/20/96 02:43 GMT, SW WHOI mooring. Time axis is relative (before synchronization).
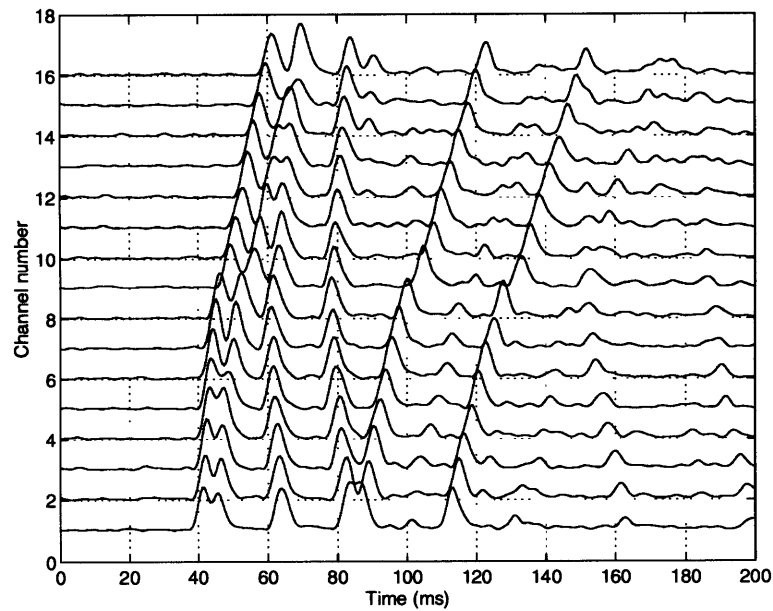
Figure 5-7: Filtered time series : shot 32, 02/20/96 02:43 GMT, SW WHOI mooring. Time axis is relative (before synchronization).

mooring	depth (m)	m/s	m/s
SW	25	0.155	0.332
SW	120	0.060	0.129
NE	25	0.137	0.355
NE	70	0.142	0.502
NE	123	0.102	0.480

Table 5.1: Temporal variability of the sound speed field, in m/s (IOS mooring data). First column: average standard deviation of the 50-minute average. Second column: standard deviation of the raw time series.
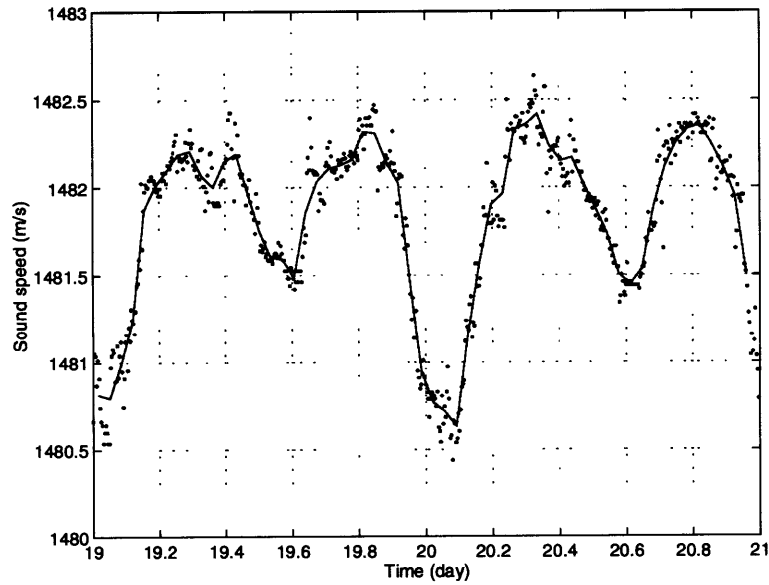
Figure 5-8: Local sound speed measured at the IOS NE mooring. Depth: 70m. Solid line: 50-minute moving average. Dots: raw data.
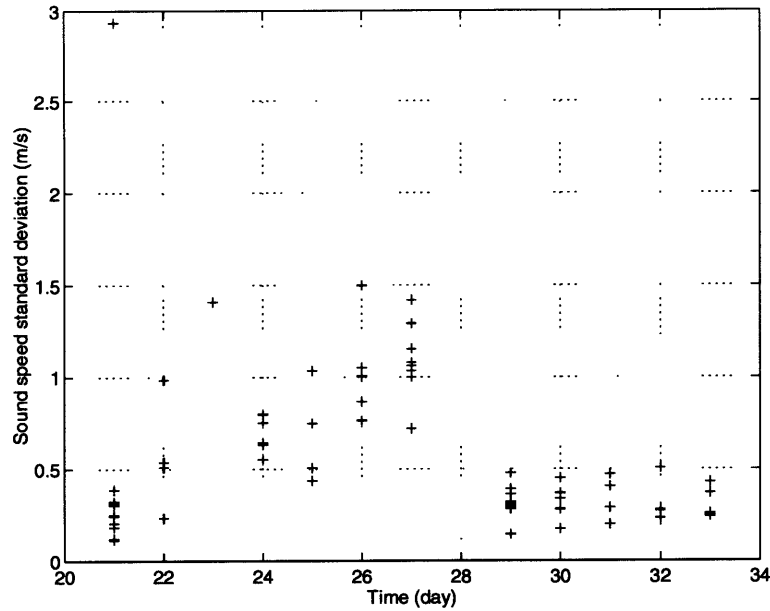
Figure 5-9: Depth variability of the sound speed field (CTD data)

06/21/96 to 07/03/96. The depth profile standard deviation was found to be of the order of $0.2m/s$ to $1.5m/s$, with variations in time (see figure 5-9).

5.3.3 Current time series

Current magnitude and direction were measured by the IOS moorings at a frequency of 12 samples per hour. Rather than lumping and averaging data points as in the case of the sound speed time series, the raw current time series was low-pass- and high-pass-filtered. The sampling frequency of the time series was thus kept at its initial value, therefore reducing interpolation and round-off errors when comparing the current data with Foreman's tidal model output. The low-frequency component was obtained by low-pass-filtering the raw data using a third-order zero-phase Butterworth filter with a cut-off frequency of $1h^{-1}$. The high frequency component was computed by subtraction of the low-frequency component from the raw data. The resulting time series are compared to Foreman's tidal model in figures 5-10 and 5-11. The standard deviation of the high frequency component was found to be between 6 and $13cm/s$. The rms variations of the current perturbation u' (actual current minus

mooring	component	$\widehat{u}'$	ϵ_u
SW	E/W	0.180	0.125
SW	N/S	0.217	0.129
NE	E/W	0.216	0.060
NE	N/S	0.155	0.062

Table 5.2: Temporal variability of the current field, in m/s. First column: rms magnitude of the current perturbation. Second column: standard deviation of the high frequency component (characteristic time shorter than 1 hour)
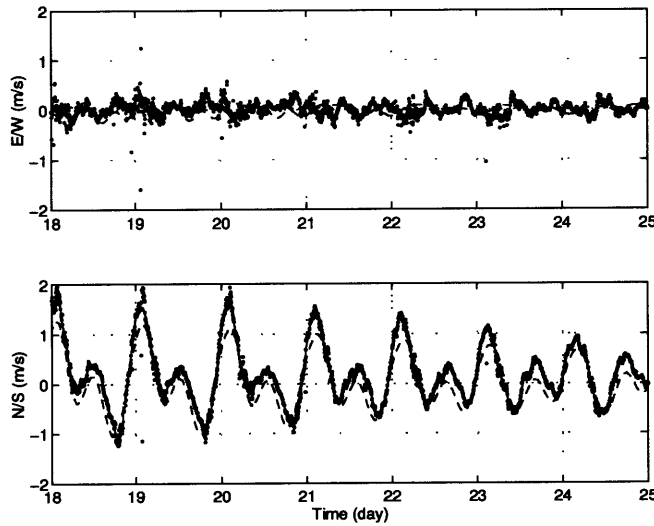
Figure 5-10: Tidal current at IOS SW mooring. Depth: 120m. Dots: raw data. Solid line: low-pass filtered data. Dotted line: Foreman's model prediction.

predicted current) were measured between 15 and $22cm/s$ (see table 5-2). The low-pass filtered current time series was used as input for the current field inversion. The high-frequency standard deviation was used as an estimate of the noise associated with the smoothed current time series.

5.4 Acoustic sensor localization

Acoustic sensor localization was carried out by minimizing the mean square difference between the measured arrival times and the arrival times predicted using the
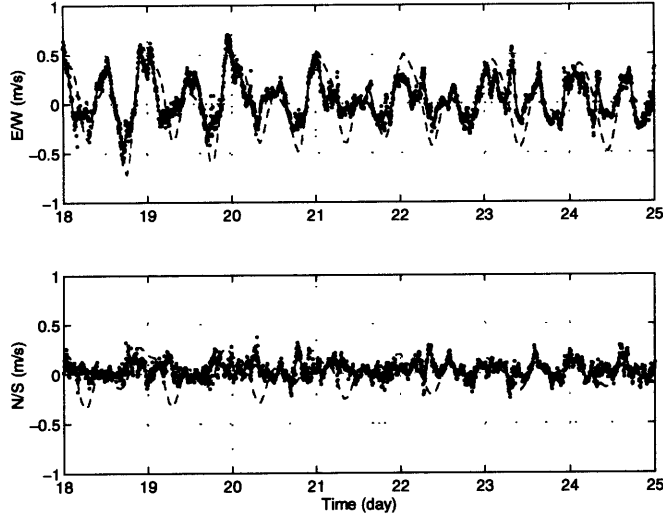
Figure 5-11: Tidal current at IOS NE mooring. Depth: 70m. Dots: raw data. Solid line: low-pass filtered data. Dotted line: Foreman's model prediction.

sensor model described in section 3.1. The cost function was expressed as:

$$\Phi(t_{src}, \{c_j\}_{j\in[1,M-1]}, \{a_j\}_{j\in[1,M]}) = \sum_{i,j}(\widetilde{T}_{i,j} - T_{i,j}(t_{src}, c_j, a_j))^2 \qquad (5.2)$$

where M is the number of moorings involved in the acoustic transmission (1, 2 or 3); $\widetilde{T}_{i,j}$ is the ith travel time measured at the jth mooring; $T_{i,j}$ is its theoretical prediction using an isovelocity profile; t_{src} is the time at which the shot was fired. Each acoustic array consisting of 16 elements, the number of arrival times per mooring was 32. For any given shot, travel times cannot be measured at all acoustic arrays either because the shot was not captured by the acquisition system, or because the direct and surface arrivals were undistinguishable. The actual acoustic receiver configurations observed in the data set are {SW,NW}, {SW,NE} and {SW,NW,NE}.

In order to keep the minimization of Φ well-constrained while estimating the source transmission time t_{src}, the sound speed along the SW track was set equal to an arbitrary value c_0. The SW track was chosen as the reference leg because of its reliability. The average sound speeds $\{c_j\}$ along the other legs were estimated using

91

mooring	b (m)	c (m)
SW	-269	437
NW	-269	417
NE	-249	377

Table 5.3: Sensor model parameters used for each acoustic array
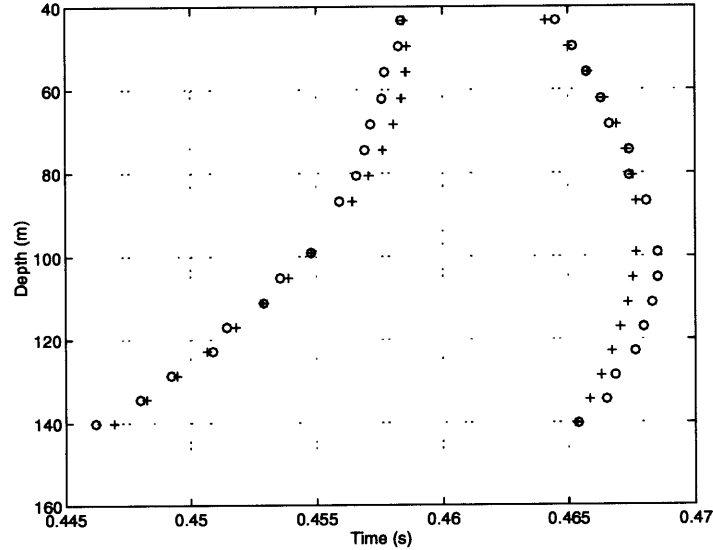
Figure 5-12: NW WHOI mooring shot 22. Circles: measured direct and surface arrival times. Crosses: predicted arrival times. Note the strong array shape effect. Source range: 670m. Time axis is absolute (post-synchronization).

(5.2) and are thus relative to c_0. A global sound speed offset term Δc was subsequently included in the sound speed inversion as discussed in chapter 4.

Predicted travel times incorporating array shape effects are shown in figure 5-12. The array shape factor a was estimated through the minimization of Φ (see equation 5.2). Note the negative convexity of the arrival pattern due to the strongly distorted array shape. The source range is approximately 670m. The rms difference between predicted and measured arrival times is $0.8ms$ in this case. Residuals were found to vary between 0.5 and $4ms$ over the two-hour period covered by the acoustic data set.
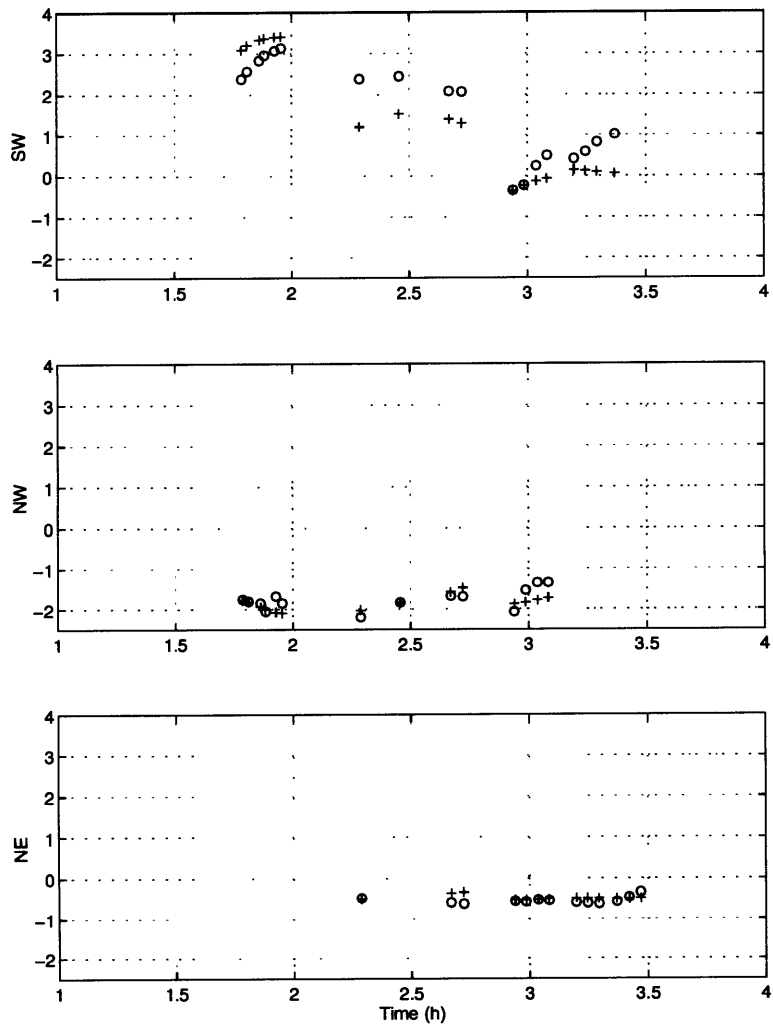
Figure 5-13: Array shape factor a vs time. Crosses: model prediction. Circles: data. Top panel: WHOI SW mooring. Middle panel: WHOI NW mooring. Bottom panel: WHOI NE mooring.

5.5 Correlation functions

5.5.1 Current field

The current field perturbation was assumed to be stationary in time and space. The temporal correlation function was estimated using the current time series measured at the IOS moorings (see figures 5-15). Figure 5-15 shows two types of correlations:

- the correlation measured in the main direction of the flow, i.e. North/South at the IOS SW mooring and East/West at the IOS NE mooring, is smooth and has a relatively broad peak.

- the correlation measured across the flow has a narrow peak and denotes the presence of turbulence. Inasmuch as this turbulence is not properly acounted for in the tidal model and cannot be spatially resolved by the array of moorings, it will be ignored in the present analysis.

The current correlation function in time is therefore fitted using the measurements made in the North/South direction in the middle of the channel, which accounts for most of the flow energy. In the absence of detailed experimental data regarding the spatial variability of the tidal flow, the current spatial correlation was estimated using the field predicted by Foreman's model (see figure 5-16). The correlation function of both flow components was assumed to be of the form [8]:

$$\Gamma_u(\Delta x, \Delta y, \Delta t) = e^{-\frac{1}{2}R_u^2} \tag{5.3}$$

where

$$R_u^2 = \left(\frac{\Delta x}{L_x}\right)^2 + \left(\frac{\Delta y}{L_y}\right)^2 + \left(\frac{\Delta t}{T_u}\right)^2$$

The correlation lengths L_x and L_y were both set equal to $1000m$ for the East/West component and $1500m$ for the North/South component. The correlation time T_u was estimated to be approximately 2 hours.

5.5.2 Sound speed field

The sound speed field perturbation was assumed to be stationary in time and space. The temporal correlation function was estimated using the sound speed time series measured at the IOS moorings (see figure 5.14). The sound speed correlation function in depth was estimated using a set of CTD casts taken over the month of June 1996 (see figure 5-14). Detailed experimental data of the sound speed spatial variability being scarce as well, the horizontal spatial correlation function of the sound speed field was assumed to be identical to that of the North-South component of the tidal flow. The temporal correlation function of the sound speed field was fitted using a modified Gaussian as suggested by Carter and Robinson [8]. The complete correlation function of the sound speed field was assumed to be as follows:

$$\Gamma_c(\Delta x, \Delta y, \Delta z, \Delta t) = \left[1 - \left(\frac{\Delta t}{T_c}\right)^2\right] e^{-\frac{1}{2}R_c^2} \qquad (5.4)$$

where

$$R_c^2 = \left(\frac{\Delta x}{L_x}\right)^2 + \left(\frac{\Delta y}{L_y}\right)^2 + \left(\frac{\Delta z}{L_z}\right)^2 + \left(\frac{\Delta t}{T_c}\right)^2$$

The correlation lengths L_x and L_y were set equal to $1500m$. The correlation depth T_z was estimated at $12m$. The correlation time T_c was estimated at 3.5 hours. The difference in correlation times between the current and the sound speed correlation functions is due to variations in the functional form used to fit to the data. The width of both main lobes is approximately the same.

Due to the periodic character of tidal forcing, the data shows a relatively high degree of temporal correlation over the course of several days, However the actual correlation level past the first 12 hours is highly dependent on location and, for current, orientation of the measurement. The model correlation functions Γ_c and Γ_u were consequently constrained to vanish for lags extending beyond approximately half a day, so that a single functional form could fit a wide variety of data. Data
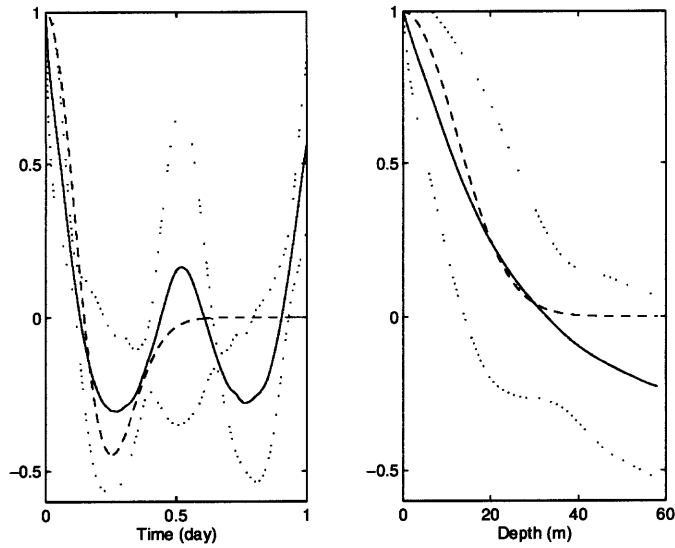
Figure 5-14: Sound speed correlation function. Left panel: temporal correlation (IOS mooring data). Right panel: correlation in depth (CTD data). Solid line: average measured correlation. Dotted line: 95% confidence interval. Dashed line: modeled correlation ($T_c = 3.5h$, $L_z = 12m$)

gathered more than a few correlation lengths or times away from the estimation time were therefore not taken into account.

5.6 Conclusion

In this chapter the Haro Strait experimental configuration was introduced. A priori statistics of the sound speed and current fields were estimated. A simple procedure for acoustic sensor localization was outlined. Armed with statistical moments of the oceanic fields in Haro Strait and the inversion procedure presented in the previous chapter, a quantitative assessment of the inversion performance can now be carried out.
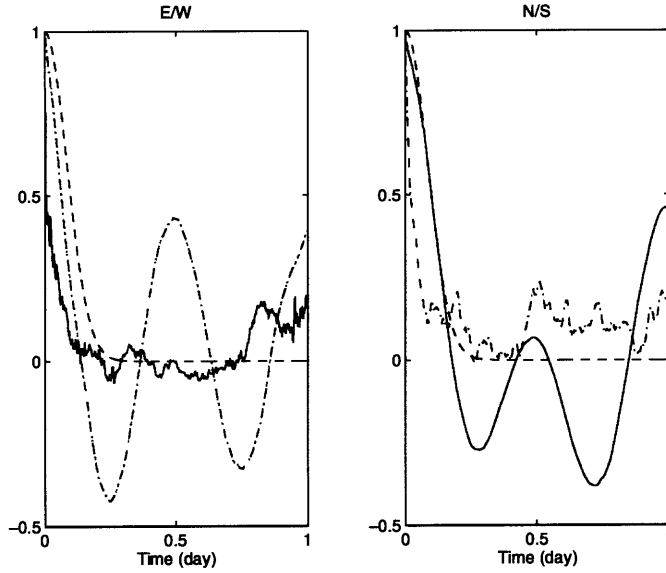
Figure 5-15: Current temporal correlation function. Left panel: east/west component. Right panel: north/south component. Solid line: IOS SW mooring. Dash-dotted line: IOS NE mooring. Dashed line: modeled correlation $(T_u = 2h)$
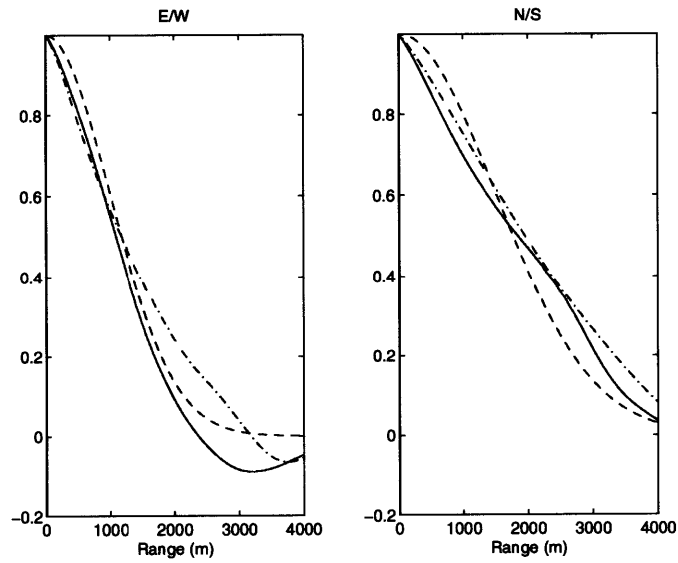
Figure 5-16: Current spatial correlation function. Left panel: east/west component. Right panel: north/south component. Solid line: correlation along the east/west axis. Dash-dotted line: correlation along the north/south axis. Dashed line: modeled correlation $(L_u = 1000m, L_v = 1500m)$

Chapter 6

Performance analysis

6.1 Introduction

6.2 Inverse resolution

6.2.1 Resolution formalism

The resolution matrix $\mathbf{T}$ relates the field perturbation estimate $\widehat{\mathbf{c}}$ to its true value $\mathbf{c}'$. For the case of the combined field estimate computed by inversion of (4.58), the resolution matrix satisfies the following identity [57]:

$$\widehat{\mathbf{c}} = \mathbf{K}_c \mathbf{G} \mathbf{c}' = \mathbf{T} \mathbf{c}' \tag{6.1}$$

where $\mathbf{G}$ is given by (4.58) and $\mathbf{K}_c$ is computed as outlined in equations (4.9-4.10). The resolution matrix is more conveniently expressed in dimensionless form:

$$\mathbf{T}^* = \mathbf{R}_{cc}^{-1/2} \mathbf{T} \mathbf{R}_{cc}^{1/2} \tag{6.2}$$

where the square root operator is defined for semi-definite positive matrices. The resolution matrix $\mathbf{T}^*$ can be be thought of as the prism through which the observer perceives reality. In the ideal case $\mathbf{T}^*$ is the identity matrix and the estimated quantity is equal to its true value. In practice it is rarely so. The kth column of $\mathbf{T}^*$ represents

the field estimate generated in response to a true field which is zero everywhere except at the kth node where it has a unit value. This response is sometimes called the resolution kernel; an example is shown in figure 6-1. The width of the resolution kernel, i.e., the resolution length, is a measure of the spatial distance over which the estimate is averaged, and as such gives an indication of the level of detail the inversion procedure might be able to resolve. Various metrics can be chosen in order to compute the resolution length. Chiu suggested computing the width of the region which contains half the total energy spread by the kernel around the original true value [10]. However this becomes a problem when sampling is very sparse and irregular as the resolution kernel is no longer necessarily well behaved and energy might be unevenly spread. By interpreting the resolution kernel (or its absolute value) as a two-dimensional probability density function, one can easily compute its second moment, which will provide a measure of resolution length. Thus if $T(x, y; x_0, y_0)$ is defined as the absolute value of the resolution kernel corresponding to the node located at (x_0, y_0), the first moments of T can be written as:

$$\mu_x = \int_{-\infty}^{+\infty} dx \int_{-\infty}^{+\infty} dy \, x \, T(x, y; x_0, y_0) \tag{6.3}$$

$$\mu_y = \int_{-\infty}^{+\infty} dx \int_{-\infty}^{+\infty} dy \, y \, T(x, y; x_0, y_0) \tag{6.4}$$

where T is normalized as:

$$\int_{-\infty}^{+\infty} dx \int_{-\infty}^{+\infty} dy \, T(x, y; x_0, y_0) = 1 \tag{6.5}$$

regardless of x_0 and y_0. The intended location of the field estimate is (x_0, y_0). The centroid (μ_x, μ_y) of the resolution kernel is interpreted as the effective location of the interpolated field. Let us for instance assume the interpolated estimate at location (x_0, y_0) is based mostly on field values at another location (x_1, y_1). The centroid will then be approximately (x_1, y_1), reflecting the fact that the estimated value is

really a mean of the measured field values at location (x_1, y_1). If we now assume the interpolated estimate is based on measured values which are approximately uniformly distributed around (x_0, y_0). The centroid (μ_x, μ_y) will then be approximately equal to (x_0, y_0), reflecting the fact that the vicinity of (x_0, y_0) was properly sampled when carrying the interpolation. The resolution bias of the inversion is consequently defined as the distance between the target location and the centroid:

$$b = \sqrt{(\mu_x - x_0)^2 + (\mu_y - y_0)^2} \tag{6.6}$$

The bias is in general close to zero within the sampling network and starts becoming non-negligible outside the network envelope. The resolution lengths are heuristically defined as the width along both x and y axes of the main lobe of the resolution kernel. This can be formally expressed as:

$$L_x^2(x_0, y_0) = \int_{-\infty}^{+\infty} dx \int_{-\infty}^{+\infty} dy \; (x - \mu_x)^2 T(x, y; x_0, y_0) \tag{6.7}$$

$$L_y^2(x_0, y_0) = \int_{-\infty}^{+\infty} dx \int_{-\infty}^{+\infty} dy \; (y - \mu_y)^2 T(x, y; x_0, y_0) \tag{6.8}$$

Thus far resolution lengths and bias have been defined for a two-dimensional inversion kernel $T(x, y; x_0, y_0)$. Similar definitions can be made for a one-dimensional kernel $T(x; x_0)$. The two-dimensional kernel of equations (6.3), (6.5) and (6.7) is simply replaced by $T(x; x_0)\delta(y)$, where δ is Dirac's delta function. The one-dimensional bias b becomes then $|\mu_x - x_0|$.

6.2.2   Acoustic inverse vertical resolution

As a first step we investigate the properties of the kernel of the acoustic inverse, i.e., the resolution and bias properties of the range-averaged sound speed field estimate computed using a single acoustic transmission. The simulated environment is inspired by the Haro Strait experiment and consists of 16 receivers equally spaced from 20 to

100
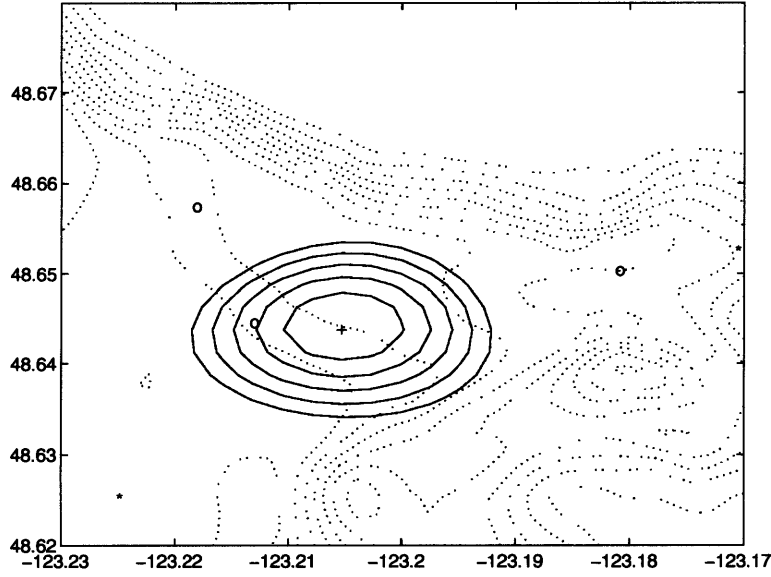
Figure 6-1: Resolution kernel of the sound speed inversion. Solid lines: isokernel lines (0.5 to 1.0). Dotted lines: isobaths. Stars: IOS moorings. Circles: WHOI moorings.

120 m in depth. Unless otherwise stated, the source is located at a range of 2 km and a depth of 50m. The acoustic inverse is formally defined by equation (4.49). The resolution matrix is written in non-dimensional form as:

$$\mathbf{T}^{(a)} = \mathbf{R}_{cc}^{(a)\,-1/2}\mathbf{K}_{c}^{(a)}\mathbf{E}\mathbf{R}_{cc}^{(a)\,1/2} \qquad (6.9)$$

and the resolution kernel is defined as:

$$T^{(a)}(z_i; z_j) = \left[\mathbf{T}^{(a)}\right]_{ij} \qquad (6.10)$$

where z_j is the target depth, or depth of the estimate, and z_i is the kernel's depth variable. The vertical resolution length is shown in figure 6-2 as a function of depth of estimate and source range. The resolution length is generally of the order of 15 m, which is a little above the medium's vertical correlation length (12 m). The large correlation length observed at short range around 80 to 100 m in depth is due to the fact that as the source range decreases, so does the insonification of the lower layers of the water column. Being poorly sampled, the lower layers are therefore poorly

101
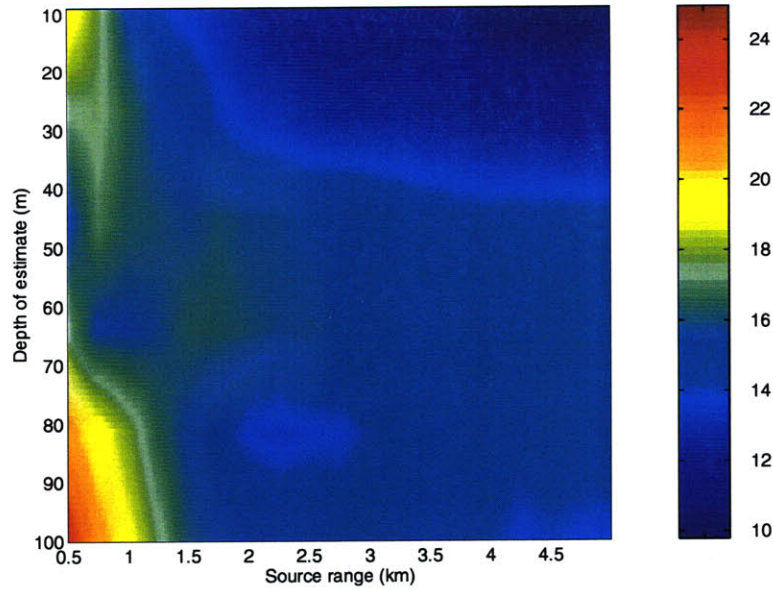
Figure 6-2: Vertical resolution length vs source range and depth of estimate. Source depth: 50 m.

resolved. The same reasoning applies to the surface layer as well and also explains the increased resolution length near the surface at short ranges. Another noticeable feature is the sharp decrease observed near the surface at larger ranges. Here again this feature is explained by the sampling of the corresponding layers; as the source range increases, acoustic rays intercept more of the surface layers and are therefore able to resolve them more accurately. Figure 6-3 shows the vertical resolution length as function of depth of estimate and source depth. For source depths below 120 m the vertical resolution length is, as previously computed, of the order of 10-15 m. A sharp increase is observed as the source depth increases past 120 m and the resolution length increases then to values of up to 25m.

The resolution bias is shown in figure 6-4 for various source ranges and depths of estimate. The source depth is 50 m. The bias is generally small, i.e. smaller than 3 m, except at small source ranges. The surface layer and the deeper layers are then poorly sampled by acoustic rays; the inverse is then based on the nearest available data points, which are all located on the source side of the estimated bin. This results
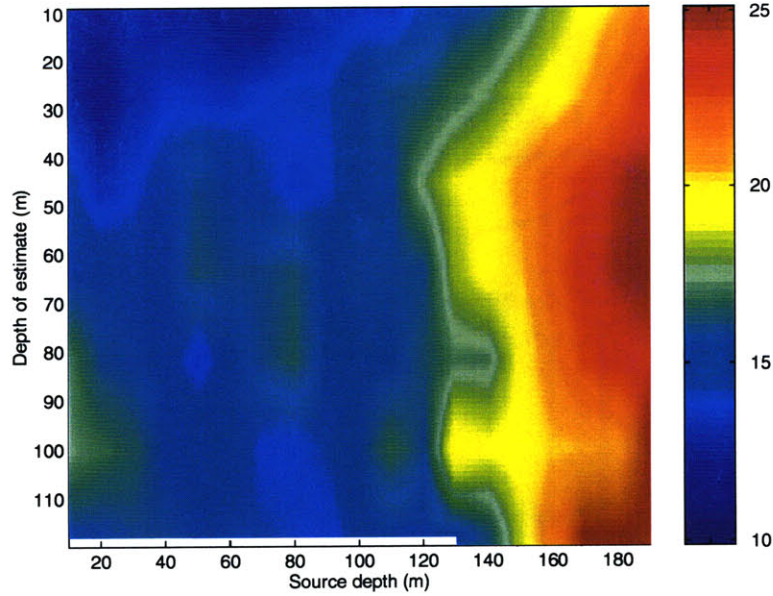
Figure 6-3: Vertical resolution length vs source depth and depth of estimate. Source range: 2 km.

in a non-negligible resolution bias. The same type of behavior is observed in figure 6-5 for the bias vs source depth and depth of estimate. The source range is 2 km. The bias is virtually zero everywhere except near the surface and the lower layers at selected source depths. The lower layers are biased for shallow source depths; the surface layer is biased for deeper source depths.

6.2.3 Combined inverse horizontal resolution

East-West and North-South resolution length maps for the combined field are shown in figures 6-6 and 6-7. The East-West and North-South resolution lengths are respectively about $950m$ and $1000m$ at the center of the network of arrays. The East-West resolution length estimate is biased near the eastern and western boundaries of the computational domains as the kernel cannot extend beyond the boundary and becomes distorted. The same effect is seen along the northern ans southern boundaries for the North-South resolution length estimate. In particular the low length region in the south-western corner is an artifact due to the proximity of the boundary combined

103
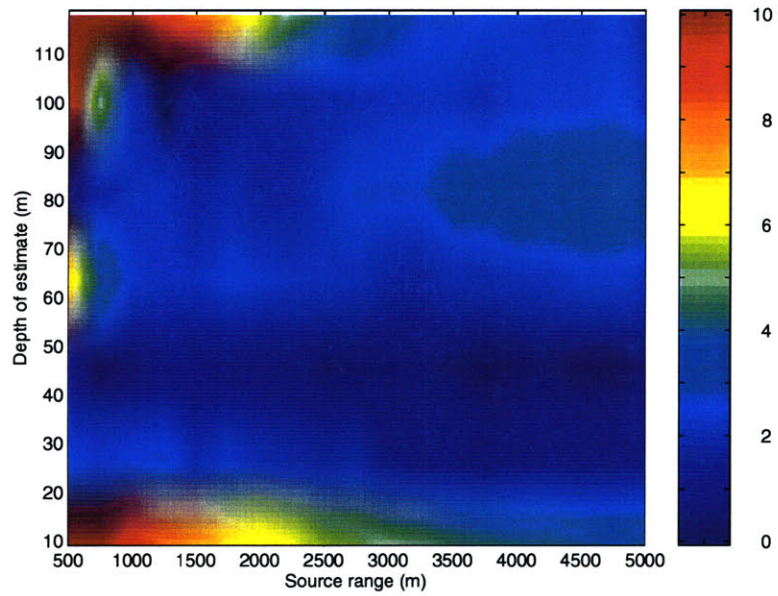
Figure 6-4: Vertical resolution bias vs source range and depth of estimate. Source depth: 50 m.
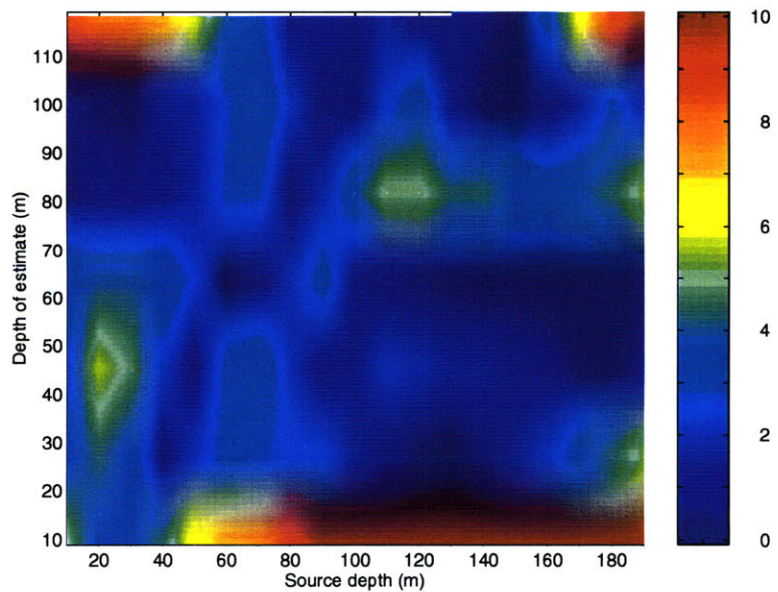
Figure 6-5: Vertical resolution bias vs source depth and depth of estimate. Source range: 2 km.
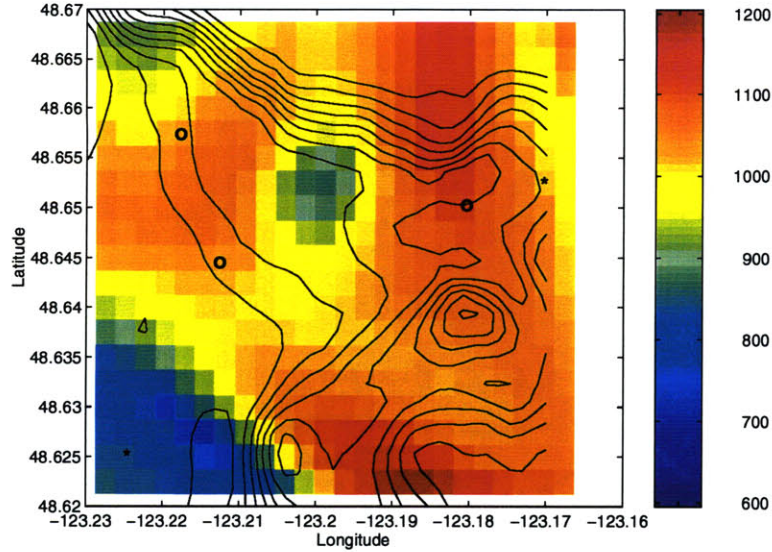
Figure 6-6: East-West resolution length of the sound speed inversion. Solid lines: isobaths. Stars: IOS moorings. Circles: WHOI moorings.

with the experimental geometry. The bias magnitude is shown in figure 6-8. As expected, it is small relative to the correlation length within the sampling network, and increases significantly outside. The correlation length is approximately 1 km. The bias outside the sampling network is due to the fact that although the interpolation takes place at the location (x_0, y_0), the available and relevant data points no longer surround the interpolation location. The resulting estimate is a weighted average of the nearest data points. These data points are located on the same side of (x_0, y_0), and the "true" location of the estimate as measured by the bias (b_x, b_y) is shifted towards the mean location of the interpolated data.

6.3   Inverse error and accuracy

In order to evaluate the accuracy of the inversion procedure a synthetic data set was generated. The simulated environment was identical to that of Haro Strait. The sound speed field was assumed to be split in two isovelocity regions: the water sound speed was equal to $1484 m/s$ on the eastern side of the -123.20 meridian, and

105
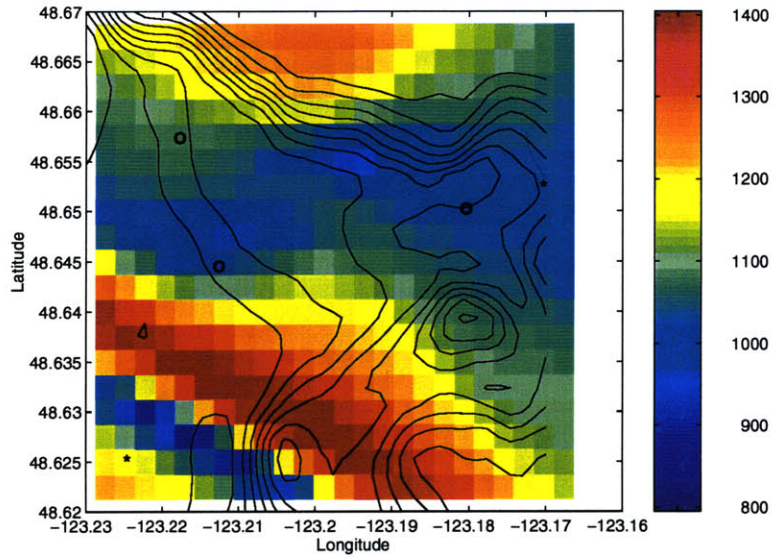
Figure 6-7: North-South resolution length of the sound speed inversion. Solid lines: isobaths. Stars: IOS moorings. Circles: WHOI moorings.
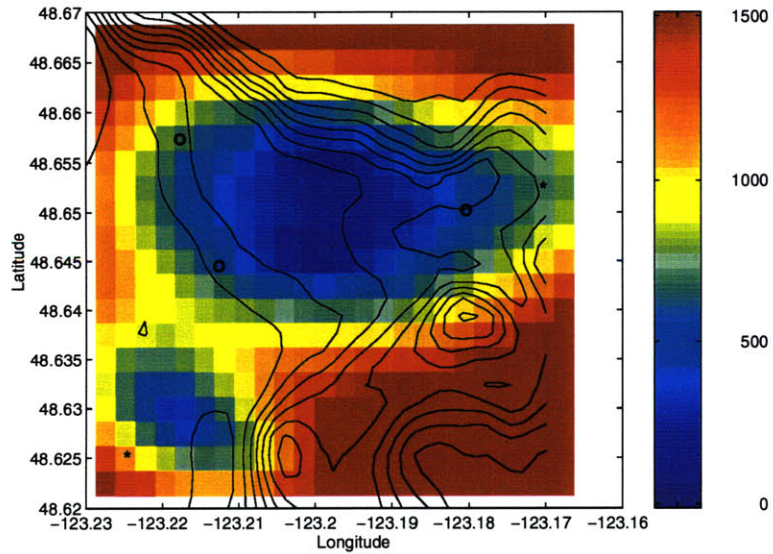
Figure 6-8: Horizontal resolution bias of the sound speed inversion. Solid lines: isobaths. Stars: IOS moorings. Circles: WHOI moorings.
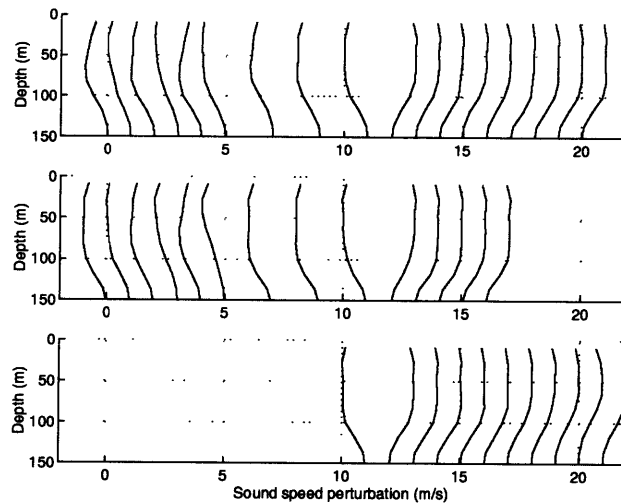
Figure 6-9: Inverted acoustic sound speed profiles (synthetic data, actual source positions). Shots 20 to 42. Shots which were not properly captured by the acquisition system, or for which surface and direct arrivals were undistinguishable, are missing. Top panel: SW WHOI mooring. Middle panel: NW WHOI mooring. Bottom panel: NE WHOI mooring.

$1482m/s$ on the western side. The transition at the meridian was set be discontinuous, which is not physical but allows a better understanding of the resolution limits of the inversion. The environment was assumed to be steady. In the absence of cyclical tidal variations, the sound speed correlation function was assumed to be a pure Gaussian. The respective impacts of the acoustic and non-acoustic data sets on the final sound speed field inversion were assessed by computing a field estimate using the acoustic data only, then the non-acoustic data only, and finally a combined field estimate.

6.3.1 Acoustic-only field estimate

The sound speed profiles computed using equation (4.49) are shown in figure 6-9. Actual profiles are isovelocity. The lower half of the water column is not insonified by the direct and surface rays and is therefore not resolved by the inversion. The surface layer is weakly resolved by the first few shots, which were fired at short range between the SW and NW WHOI moorings. Some inaccuracies are consequently observed in the corresponding sound speed profiles.

107

The final sound speed field estimate based on acoutic data only is computed by inverting equation (4.54). It is shown in figure 6-11. Actual source positions were taken into account (see figure 6-10). The associated error field is shown in figure 6-12. Two separate effects can be observed. First the sound speed field is smeared in space due to the assumed correlation. The front is no longer a sharp discontinuity but a smooth transition zone with a width of about 1200m, or a little less than a correlation length $(1500m)$. Then the front is shifted by about half a correlation length to the west of the actual front line at the latitude of maximum discrepancy. This is related to the confidence level in the acoustic data gathered between the two westernmost WHOI moorings. Due to the short ranges of the shots fired between these two moorings, the estimated error of the acoustic sound speed profiles is high relative to those measured along longer tracks east of the SW WHOI mooring. When the various acoustic profiles are merged with the local IOS measurements, the inverse estimate is contrained to be 1484m/s on the east side of the -123.20 meridian with a relatively low error and 1482m/s on the west side with a somewhat higher error level. The smoothness constraint imposed by the correlation function then shifts the estimated front position towards the region of higher uncertainty.

In order to validate this interpretation a synthetic data set was generated assuming source positions were uniformly distributed over the region encompassing the acoustic moorings (see figure 6-13). The resulting sound speed field estimate and its error field are shown in figures 6-14 and 6-15. As anticipated the front is no longer shifted. The estimate below the 48.64 N parallel is inaccurate as this region of the ocean was not insonified by the acoustic transmissions.

6.3.2 Time-series-only field estimate

The sound speed field estimate based on non-acoustic data only is computed by inverting equation (4.56). It is shown in figure 6-16. Its associated error field is shown in figure 6-17. The field is properly estimated within a correlation length of the IOS moorings. Since the measurements are local, no information is gained about
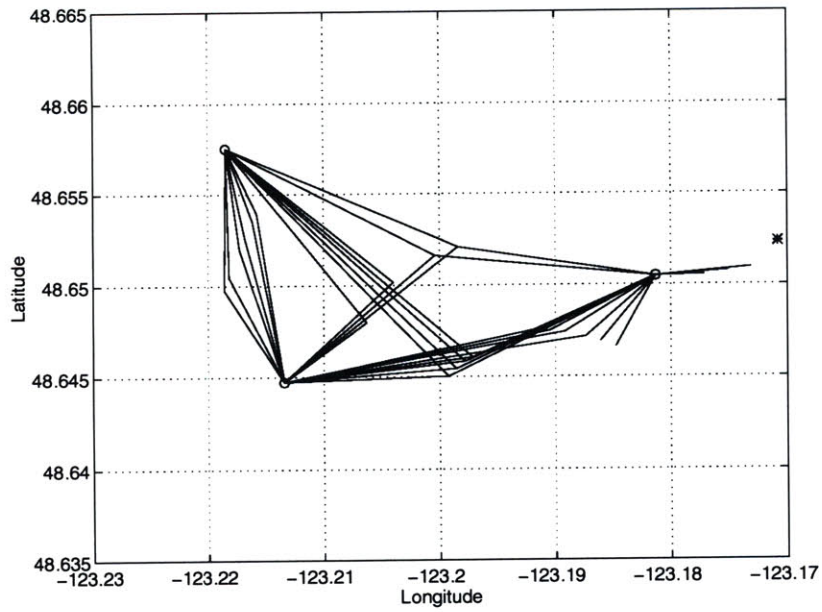
Figure 6-10: Acoustic transects, actual source positions.

Figure 6-11: Inverted sound speed field perturbation using acoustic data only (synthetic data, actual source positions). Solid lines: isobaths. Dash-dotted line: actual front location. Dotted lines: isovelocity lines (1482 and $1484m/s$) Stars: IOS moorings. Circles: WHOI moorings.

109

Figure 6-12: Estimated error of the inverted sound speed field perturbation using acoustic data only (synthetic data, actual source positions). Solid lines: isobaths. Stars: IOS moorings. Circles: WHOI moorings.
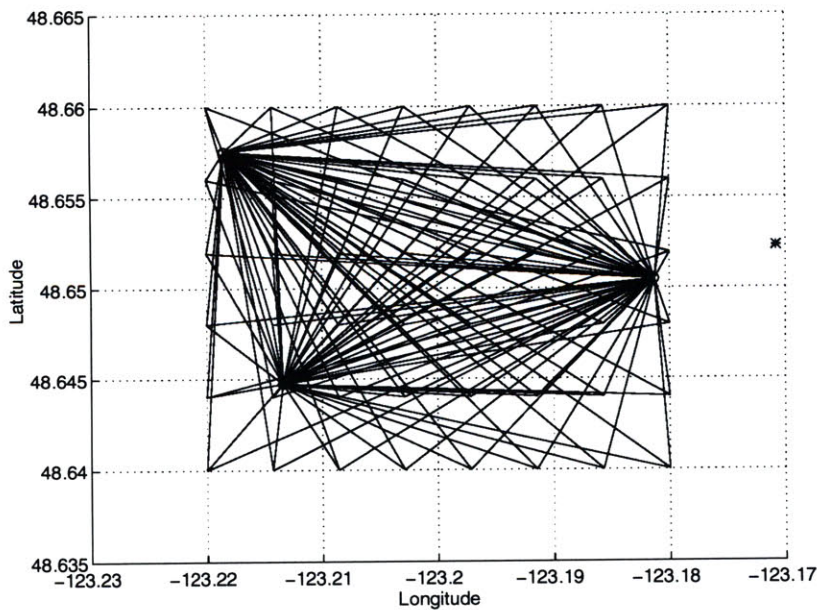
Figure 6-13: Acoustic transects, simulated source positions.
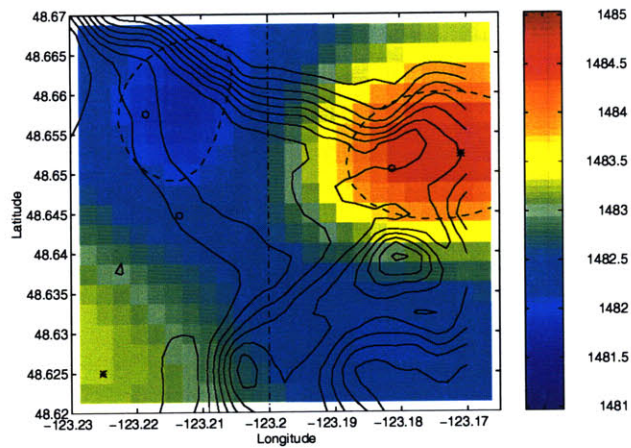
Figure 6-14: Inverted sound speed field perturbation using acoustic data only (synthetic data, simulated source positions). Solid lines: isobaths. Dash-dotted line: actual front location. Dotted lines: isovelocity lines (1482 and 1484m/s) Stars: IOS moorings. Circles: WHOI moorings.
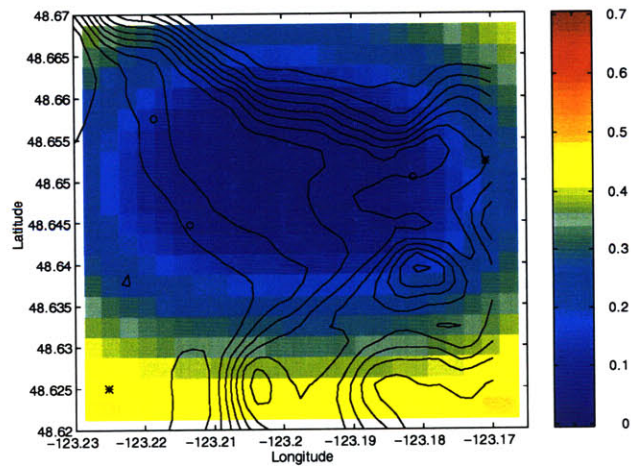
Figure 6-15: Estimated error of the inverted sound speed field perturbation using acoustic data only (synthetic data, simulated source positions). Solid lines: isobaths. Stars: IOS moorings. Circles: WHOI moorings.
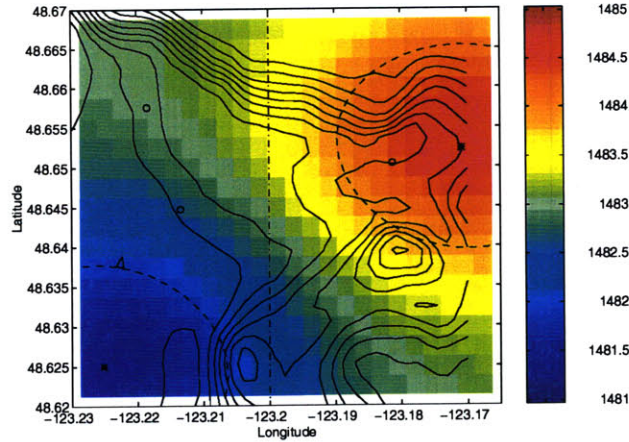
Figure 6-16: Inverted sound speed field perturbation using non-acoustic mooring data only (synthetic data). Solid lines: isobaths. Dash-dotted line: actual front location. Dotted lines: isovelocity lines (1482 and $1484m/s$) Stars: IOS moorings. Circles: WHOI moorings.

the sound speed field beyond the immediate vicinity of the moorings. The error level is relatively high compared to the acoustic estimate, reflecting the comparatively poor information content of the mooring data. This derives from the fact that the mooring data is essentially local in character, whereas the acoustic data is global to the extent that acoustic waves sample large masses of water and provide integral information about the ocean environment.

6.3.3 Combined field estimate

The sound speed field estimate combining acoustic and non-acoustic data was computed by inverting equation (4.58). The field estimate for actual source positions is shown in figure 6-18. Its associated error field is shown in figure 6-19. As discussed in section 6.3.1 the actual front location is shifted slightly to the west. The final field incorporates information gathered by both acoustic and non-acoustic means. The error field therefore shows decreased levels which are consistent (i) with the acoustic inverse error within the acoustic moorings, and (ii) with the non-acoustic inverse error near the non-acoustic moorings. Figure 6-20 shows the field estimate for the case of simulated source positions. The original field is properly recovered except in the
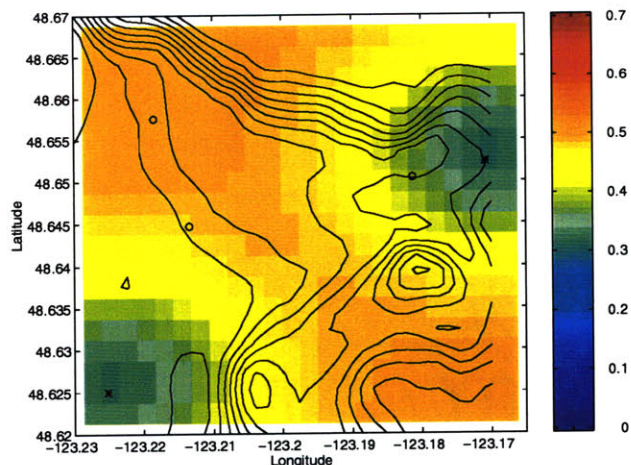
Figure 6-17: Estimated error of the inverted sound speed field perturbation using non-acoustic mooring data only (synthetic data). Solid lines: isobaths. Stars: IOS moorings. Circles: WHOI moorings.

lower right quadrant which was probed by neither acoustic nor non-acoustic means. The smoothing observed is inherent to the inversion and cannot be avoided.

The error field of the combined estimate is compared to the error field of the acoustic only field estimate in figure 6-30. The relative variance decrease due to the addition of local, non-acoustic data is plotted with respect to latitude and longitude. While the relative variance decrease is only of approximately 5% within the acoustic network, it grows rapidly up to 55% near the non-acoustic moorings. The impact of incorporating non-acoustic data in the inversion can also be assessed by computing the average estimated variance across the whole grid used for the inverted field. On average, 17.4% of the a priori variance can be accounted for by the non-acoustic only estimate (average residual variance of 82.6%); 48.4% of the a priori variance can be accounted for by the acoustic only estimate (average residual variance of 51.6%); 55.5% of the a priori variance can be accounted for by the combined estimate (average residual variance of 44.5%). Near the center of the acoustic network, these figures become 7.1% (92.9%), 84.8% (15.2%) and 85.2% (14.8%) respectively.

113

Figure 6-18: Inverted sound speed field perturbation using both acoustic and non-acoustic data (synthetic data, actual source positions). Solid lines: isobaths. Dash-dotted line: actual front location. Dotted lines: isovelocity lines (1482 and 1484m/s) Stars: IOS moorings. Circles: WHOI moorings.
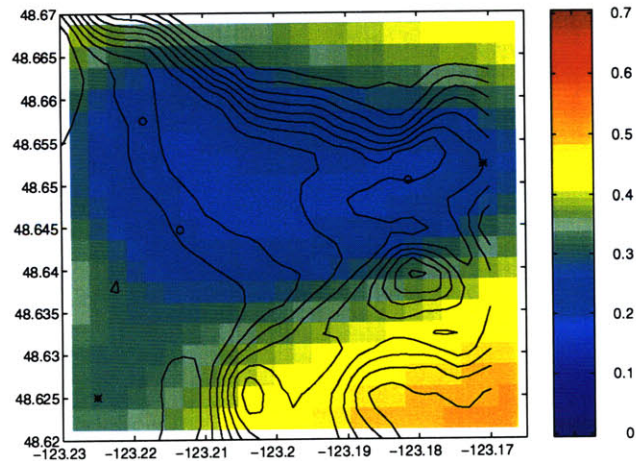
Figure 6-19: Estimated error of the inverted sound speed field perturbation using both acoustic and non-acoustic data (synthetic data, actual source positions). Solid lines: isobaths. Stars: IOS moorings. Circles: WHOI moorings.
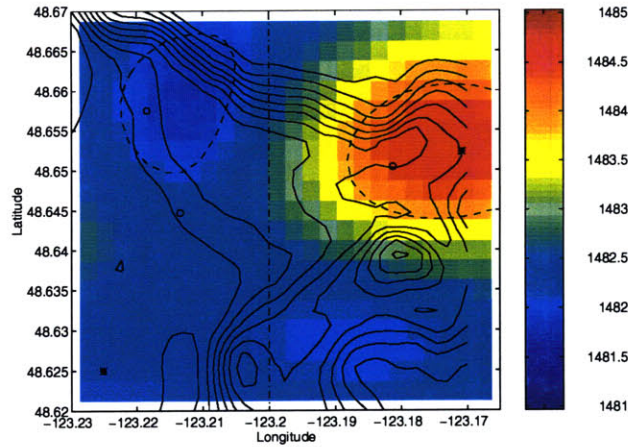
Figure 6-20: Inverted sound speed field perturbation using both acoustic and non-acoustic data (synthetic data, simulated source positions). Solid lines: isobaths. Dash-dotted line: actual front location. Dotted lines: isovelocity lines (1482 and $1484m/s$) Stars: IOS moorings. Circles: WHOI moorings.
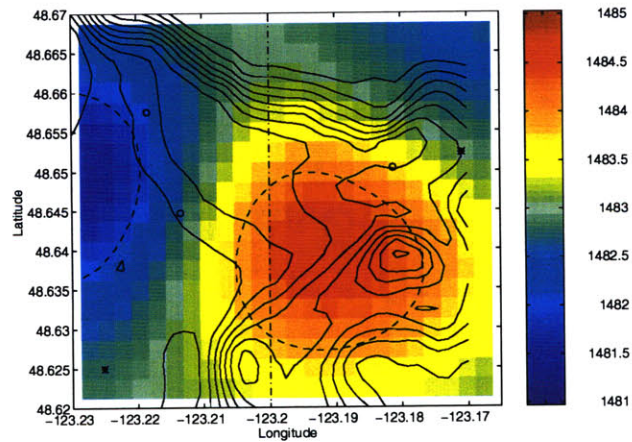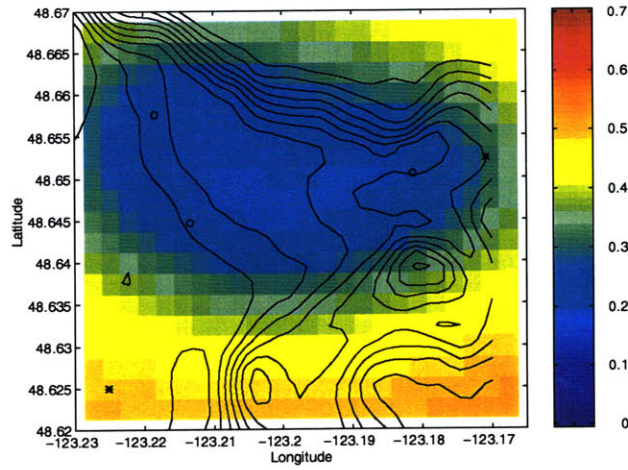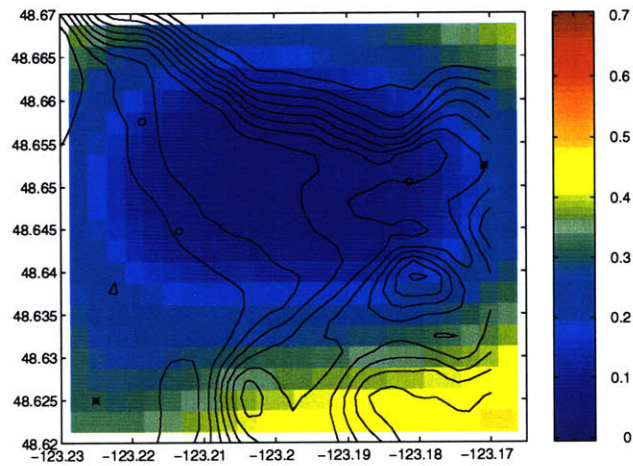

Figure 6-21: Estimated error of the inverted sound speed field perturbation using both acoustic and non-acoustic data (synthetic data, simulated source positions). Solid lines: isobaths. Stars: IOS moorings. Circles: WHOI moorings.

## 6.3.4 Effect of current mismatch

Tidal currents are taken into account in the sound speed inversion by including the barotropic (depth-independent) current field estimate in the sound speed reference state when estimating the sound speed field. The current field taken as a reference being an estimate itself, the effect of a possible mismatch is investigated in this section.

An examination of the predicted current field at the time the acoustic sources transmitted shows the effect of tidal currents is strongest between the NW and SW WHOI moorings. These two moorings are located near the center of the channel and are oriented in the direction of the main flow. Acoustic transmissions made when the source was between these two moorings, i.e., shots 20 to 25, are the most susceptible to a possible current mismatch. Other transmissions are significantly less prone to current mismatches simply because the local current or its projection on the acoustic track is significantly smaller. This fact is partially reflected by the array shape factors shown in the previous chapter (fig 5-13); the NE WHOI shape factor is significantly smaller and more stable than that of its NW and SW counterparts.

The effect of current mismatch was simulated by adding a uniform current of arbitrary amplitude to the region between the SW and the NW WHOI moorings in the combined field estimation. The reference sound speed field used in the inversion therefore included the effect of an added North-South current uniform between the two westernmost WHOI moorings and vanishing everywhere else. Figure 6-22 shows the influence of a 10-cm/s mismatch (0.2 kt). The magnitude of the current mismatch being consistent with the magnitude of the error field imposed on the inversion, the effect of the mismatch is barely perceptible. The 1484-m/s isospeed line is very slightly inflected as a result of the mismatch. Figure 6-23 shows the influence of a 50-cm/s mismatch (1.0 kt). The magnitude of the mismatch is now equal to the a priori sound speed standard deviation. The effect of the mismatch starts becoming more visible. The 1484-m/s isospeed line is shifted a little more south. However, the rest of the field is unaffected and the overall structure of the field is unchanged. Figure 6-24

shows the inflence of a 100-cm/s mismatch (2.0 kt). The frontal structure is now inflected a little more in the East-West direction, and the position of the recovered front starts being more markedly affected by the current mismatch.

When evaluating the performance of Forman's tidal model in the Haro Strait region, two measures of accuracy can be considered. The first and most easily observed is the temporal variability of the time series recorded at the SW and NE IOS mooring locations. The corresponding current perturbation (actual minus prediction) was shown in the previous chapter to have a measured a priori standard deviation of about 15 to 20 cm/s. The second measure of accuracy is given by the spatial variability of the perturbation, which is difficult to evaluate due to practical sampling considerations. However, the overall effect of spatial variations in an environment such as Haro Strait is likely to be very small as the different variations along the acoustic track are likely to cancel out one another. On the other hand the systematic current offsets which will build up along an acoustic ray are well captured by the temporal variability measured at the IOS moorings since they are to some extent spatially invariant. The magnitude of the actual mismatch is therefore expected to be at most 20cm/s, which is the maximum a priori standard deviation of the current field perturbation. In most cases the actual mismatch is smaller than 10 cm/s once the current data is assimilated. This of course does not include the small scale spatial variability which cannot be captured by an observational system such as the one deployed in Haro Strait. The effect of current mismatch on the final field estimate therefore appears to be minimal. This low sensitivity was enabled by the use of a reasonably accurate tidal model and by factoring the current uncertainty in the error estimate used in the field inversion.
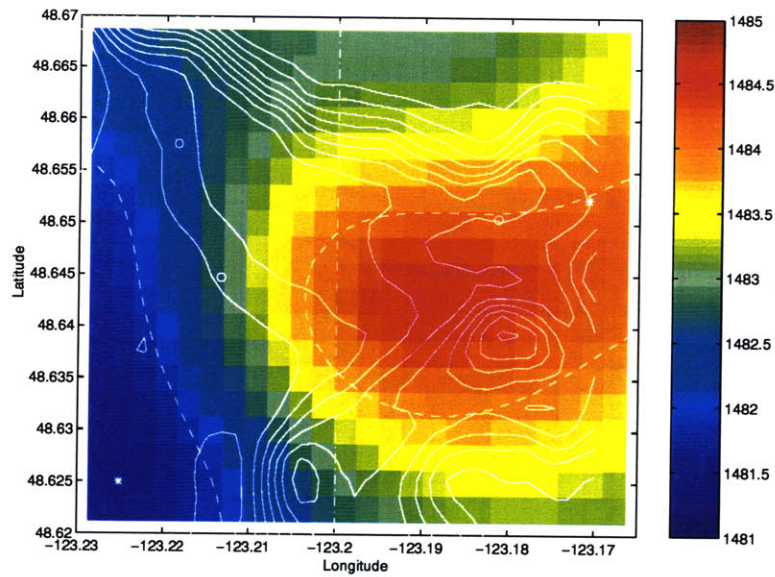
Figure 6-22: Inverted sound speed field perturbation using both acoustic and non-acoustic data (synthetic data, actual source positions) with a 10cm/s current mismatch in the northwestern section. Solid lines: isobaths. Dash-dotted line: actual front location. Dotted lines: isovelocity lines (1482 and 1484m/s). Stars: IOS moorings. Circles: WHOI moorings.
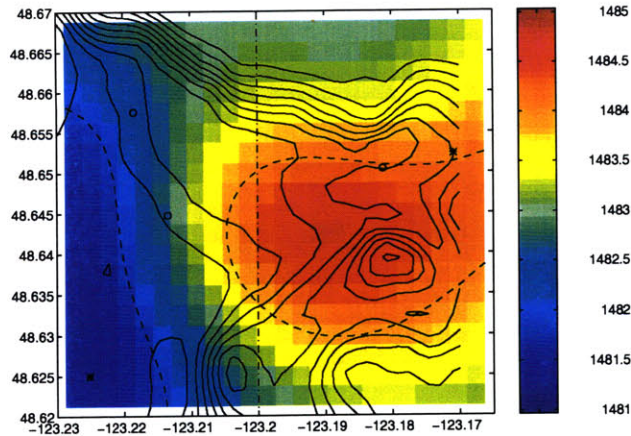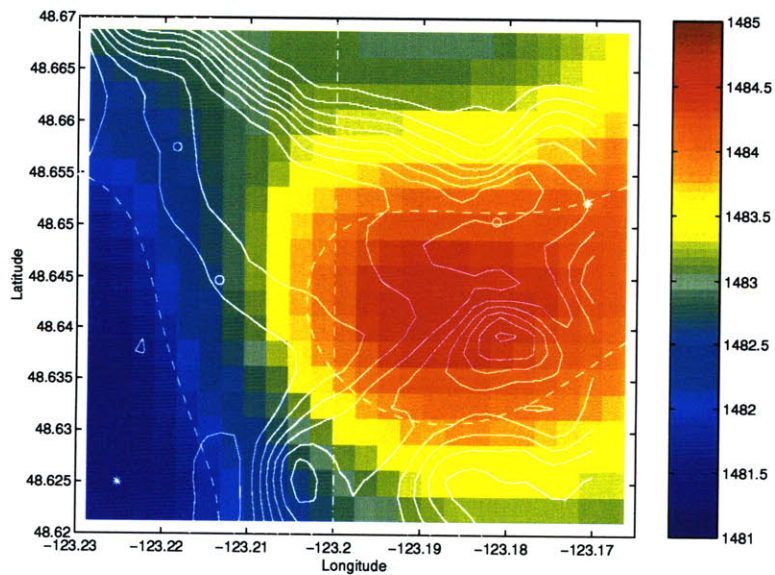

Figure 6-23: Inverted sound speed field perturbation using both acoustic and non-acoustic data (synthetic data, actual source positions) with a 50cm/s current mismatch in the northwestern section. Solid lines: isobaths. Dash-dotted line: actual front location. Dotted lines: isovelocity lines (1482 and 1484m/s). Stars: IOS moorings. Circles: WHOI moorings.

118
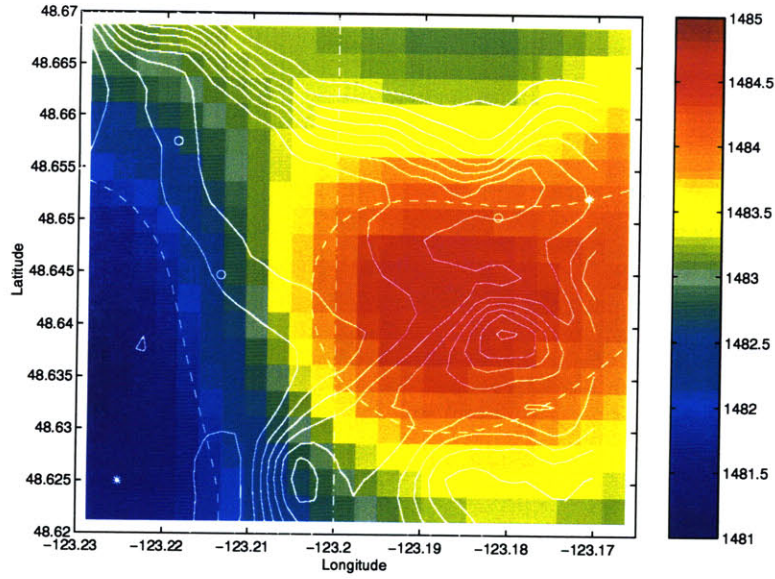
Figure 6-24: Inverted sound speed field perturbation using both acoustic and non-acoustic data (synthetic data, actual source positions) with a 1m/s current mismatch in the north-western section. Solid lines: isobaths. Dash-dotted line: actual front location. Dotted lines: isovelocity lines (1482 and 1484m/s). Stars: IOS moorings. Circles: WHOI moorings.

6.4 Acoustic inverse Cramer-Rao bounds

6.4.1 Background

The Haro strait acoustic data set was processed using a perturbational travel-time tomographic approach. The data set could presumably have been processed using for instance a classical incoherent matched-field processing aproach [42] In order to appraise the performance of both approaches in the context of the Haro Strait experiment, Cramer-Rao bounds of the acoustic inverse were computed. The Cramer-Rao bound is a theoretical limit of accuracy. It depends on the information content of the data only. In particular it does not depend on the inversion algorithm. Alternatively the Cramer-Rao bound can be interpreted as a measure of the sensitivity of the Green's function to any parameter of interest. For the case of a Gaussian parameter **a**, the Cramer-Rao bound **CRB** is given by its inverse, the Fisher Information Matrix

[2]:

$$\left[\mathbf{CRB}^{-1}\right]_{ij} = Tr\left(\mathbf{K}_r^{-1}\frac{\partial\mathbf{K}_r}{\partial a_i}\mathbf{K}_r^{-1}\frac{\partial\mathbf{K}_r}{\partial a_j}\right) + \left[\mathbf{R}_a^{-1}\right]_{ij} \qquad (6.11)$$

where Tr is the trace operator, $\mathbf{K}_r$ is the covariance of the total observation vector, and $\mathbf{R}_a$ is the covariance matrix of $\mathbf{a}$. The first term accounts for a posteriori information contained in the data. The second term accounts for a priori information contained in the probability density function of $\mathbf{a}$. Although an attempt was made in section 4.2.1 to present travel-time tomography and matched-field tomography under a single framework, the two approaches are still often presented and investigated independently of each other in the ocean acoustic literature. In particular, different assumptions are made about the field or parameter estimated. Matched field tomography assumes no a priori knowledge of $\mathbf{a}$, which is considered unknown but non-random ($\mathbf{R}_a^{-1}$ vanishes). Travel-time tomography on the other hand relies heavily on a priori knowledge of $\mathbf{a}$, which is considered random. In practice however, some degree of a priori information is required in both approaches. The key difference then appears to rest in the use of frequency coherence. Although nothing formally restricts the use of frequency-coherent matched-field tomography algorithms, matched-field tomography is traditionally frequency-incoherent for reasons of stability when estimating the data sample covariance matrix. Travel-time tomography on the other hand is by definition frequency-coherent since travel times can be interpreted as a coherent phase integral across frequency.

Cramer-Rao bounds were computed assuming both frequency-coherent and frequency-incoherent processing for the waveguide depicted in figure 6-25. This waveguide is an idealized model of the conditions of propagation in Haro Strait. The source frequency was lowered to 300Hz in order to decrease computational load. The actual light bulb source center frequency is approximately 500 Hz. However, the source spectral content below 500Hz only was used in the acoustic inversion (see chapter 5). The Source Level of 160 dB and the Noise Level of 90 dB are observed but pessimistic values.
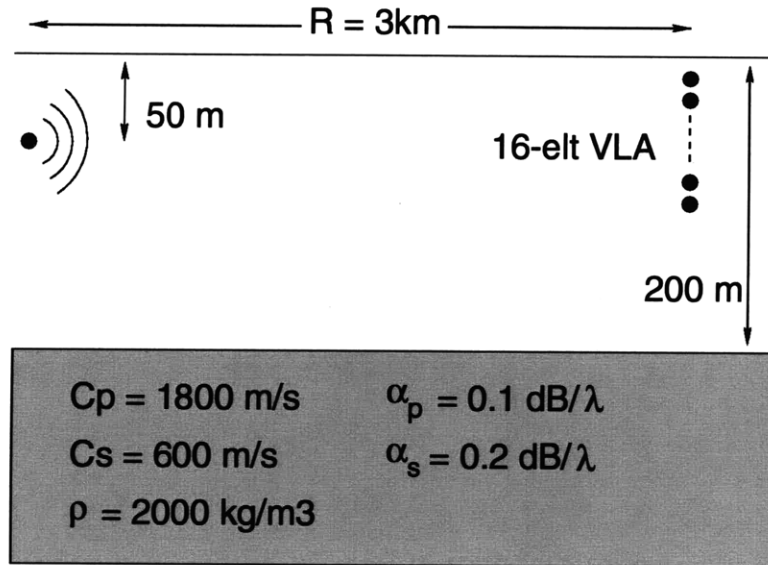
Figure 6-25: Simulated waveguide. Source Level: 160dB. Noise Level: 90dB. Source center frequency: 300Hz. Source bandwidth: 100Hz. Observation time: 1s.

The actual Source Level could be as high as 170 dB and the actual Noise Level could be as low as 70-80 dB. Although multiple arrivals can be observed over the course of several seconds at the ranges considered in the computations, in practice the Haro Strait light bulb signals rarely extended beyond one second due to bottom scattering. The observation time used in the computations was therefore set to 1 s. The bounds were evaluated using Green's functions generated by OASES [70].

6.4.2   Effect of source bandwidth

Figure 6-26 shows the dependence of the bounds on source bandwidth. The total energy of the source signal being kept constant, the frequency-incoherent bound is independent of bandwidth. The frequency-coherent bound varies as $\Delta W^{-1/3}$ at lower bandwidths. The effect of frequency coherence appears most pronounced at large bandwidths, for which the bound varies as $\Delta W^{-1/2}$.

By contrast, computations by Baggeroer for the deep ocean case lead to similar error bound levels, but with a bandwidth dependence of the order of ΔW^{-1}. The

difference might be due to the influence of the waveguide on acoustic propagation. The simulations presented in this thesis include strong bottom interactions in a shallow waveguide whereas Baggeroer's work modeled deep ocean propagation with little bottom interaction. More recent simulations by Daly for a similar shallow water waveguide show much smaller bounds and virtually no effect of frequency coherence. This discrepancy is attributed to two factors. First, the observation time in Daly's simulations is 50 s, or 50 times larger than the observation time used in the present computations. Second, the source range is 15 km instead of 3 km in the present case. The argument was made that given the spread of group velocities in the shallow water waveguide at 15 km, a spacing of 0.02 Hz (and therefore an observation time of 50s) was required in order to statisfy Nyquist's criterion in the frequency integral involved in the computation of the bound. The integral formulation however is of pure analytical convenience and has no physical basis. The derivation of Cramer-Rao bounds is made using the algebraic notation of equation (6.11) for an arbitrary frequency spacing which depends on the experimental configuration chosen by the observer. The amount of information contained in Daly's simulated acoustic data is therefore significantly larger than that of the present simulated data, leading to error bounds of significantly different levels.

6.4.3 Effect of source range

Figure 6-27 shows the dependence of the bounds on source range. Range affects the bound in two separate ways:

- from a perturbational perspective, an increase in range leads to a corresponding increase in the field perturbation, i.e., in signal level. Put differently a small sound speed variation will have a larger effect on the measured field at larger ranges.

- from a wave propagation perspective, larger ranges correspond to larger transmission losses and therefore larger signal attenuation.

122
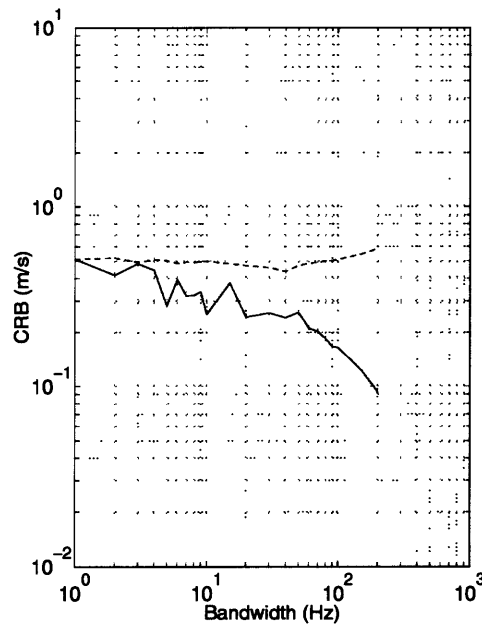
Figure 6-26: Cramer-Rao bound vs signal bandwidth. Solid line: frequency-coherent processing. Dashed line: frequency-incoherent processing

These two effects can be seen with the frequency-coherent bound. The bound decreases at smaller ranges when the signal-to-noise ratio is still large enough and the signal keeps building up. The bound degrades at larger ranges when the effect of transmission loss becomes overwhelming. In order to separate these two effects, the bounds were computed while keeping the receiver signal-to-noise ratio constant (see figure 6-27). The Cramer-Rao bounds then show a significant decrease with range.

As an element of comparison, actual acoustic inverse error estimates are plotted vs source range (figure 6-28). These error estimates were computed using equation (4.51). Before any comparison is made with figure 6-27, several important differences must be pointed out:

- the error estimates are computed assuming a significant body of a priori knowledge, described earlier in this chapter and in chapter 4.

- the acoustic inversion is a partial field inversion since it uses travel times of the direct and surface arrivals only. The Cramer-Rao bounds on the other hand are

123
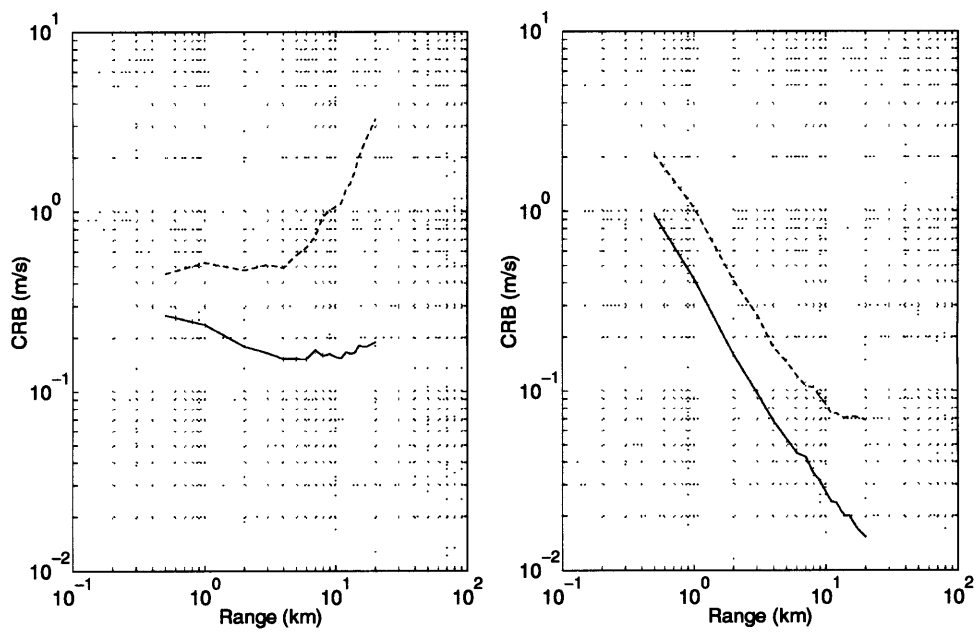
Figure 6-27: Cramer-Rao bound vs source range. Left panel: source level and noise level are kept constant. Right panel: source level is adjusted in order to keep the receiver signal-to-noise ratio constant. Solid line: frequency-coherent processing. Dashed line: frequency-incoherent processing
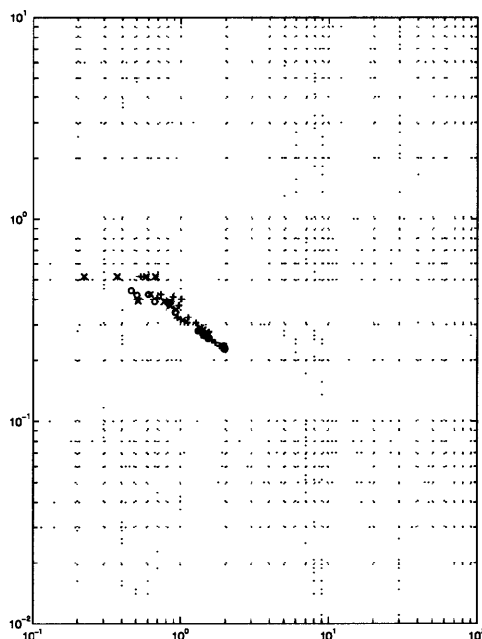
Figure 6-28: Acoustic inverse error vs source range. Crosses: SW WHOI mooring. Circles: NW WHOI mooring. X's: NE WHOI mooring.

based on full-field information.

- the Cramer-Rao bounds are computed assuming a realistic but pessimistic signal-to-noise ratio. The average signal-to-noise ratio observed in Haro Strait might be 5 to 10 dB larger.

The acoustic inverse error estimate exhibits a $r^{-1/2}$ dependence on source range, whereas the Cramer-Rao bound's dependence was approximately $r^{-1/3}$ for the frequency-coherent bound. Both standard deviations are in the vicinity of 0.1 to 1.0 m/s. The actual Cramer-Rao bound corresponding to the acoustic estimates would likely be decreased by a factor of 5 if actual signal-to-noise ratio levels were considered.

6.4.4 Effect of signal-to-noise ratio

The effect of signal-to-noise ratio (constant range) is shown in figure 6-29. Expectedly, the effect of a receiver signal-to-noise ratio increase at constant range is similar to a range increase at constant receiver signal-to-noise ratio. Both the frequency-

125
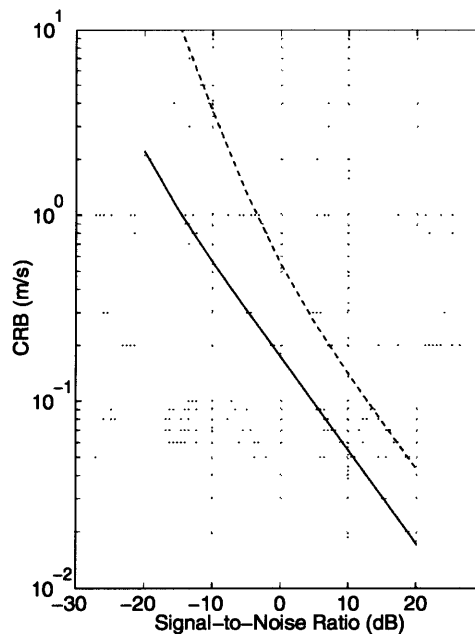
Figure 6-29: Cramer-Rao bound vs signal-to-noise ratio. Solid line: frequency-coherent processing. Dashed line: frequency-incoherent processing

incoherent and the frequency-coherent bounds decrease by an order of magnitude for a 20dB increase in signal-to-noise ratio. However, such a decrease in unlikely to be observed while actually processing acoustic data from a practical shallow water waveguide. The increase in source power will merely increase the reverberation level; unless the latter is properly modeled the additional information buried in the received signal will not be extracted by the inversion algorithm.

6.5 Conclusion

The performance of the inversion scheme presented earlier was analyzed in this chapter. Horizontal resolution lengths as low as 900 m and error levels as low as 15 cm/s (10% of the a priori variance) were achieved by combining the various data sets available across time and space. The actual source configuration was shown to induce an East-West bias of about half a correlation length when inverting the position of a sharp North-South front intersecting the center of the acoustic network. Finally, the

126
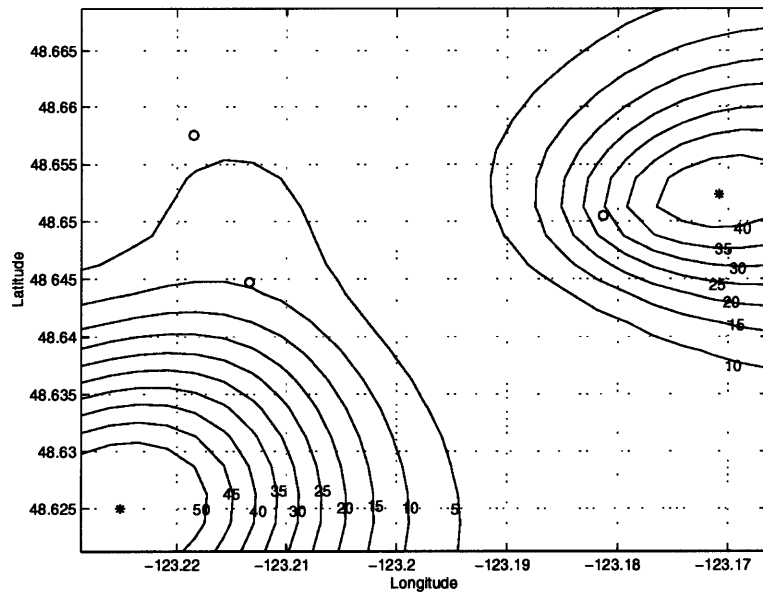
Figure 6-30: Relative difference in estimated sound speed variance (in percentage terms) between the combined estimate error and the acoustic only estimate error.

importance of exploiting signal frequency coherence was investigated by computing Cramer-Rao bounds for a synthetic Haro Strait-like environment. Given the short ranges and relatively high noise levels encountered in Haro Strait, taking into account frequency coherence, e.g. by using travel times, was found to substantially lower the corresponding error bounds.

Chapter 7

Experimental inversion results

7.1 Introduction

The inversion scheme which was developed in chapter 4 and tested using synthetic data in chapter 6 is now applied to the low frequency Haro Strait data set. The acoustic data covers a two-hour period during flood tide on 06/20/96. As the non-acoustic data is continuously available, the sound speed and current fields will be initially estimated using the non-acoustic data only. As acoustic shots are fired and acoustic data becomes available, it is included in the inversion and the evolution of the estimated field will then be discussed. Finally the adequacy and the relevance of the inversion is discussed in light of the experimental constraints encountered in Haro Strait.

7.2 Haro Strait data

7.2.1 Inversion summary

Using the procedures outlined in chapters 4 and 5, the data is first conditionned. The sound speed and current time series measured at the IOS moorings are low-pass filtered. Ray travel times are extracted from all past and present acoustic time series available at the time of inversion. Acoustic array shapes are estimated by

projecting the acoustic data on the array displacement model (bearing in mind ranges are relatively short). Travel time residuals are then inverted to produce a range-averaged acoustic tomographic sound speed profile for each acoustic shot.

The various data sets available for the combined field inversion are then:

- individual range-averaged sound speed profiles for each acoustic shot fired

- acoustic array displacement data

- point measurements of sound speed at the IOS moorings

- point measurements of current at the IOS moorings

The inversion starts with the last two data sets only as shots have not been fired yet. In time shots are fired and past and present acoustic data is included in the inversion as it becomes available. These four data sets are combined as discussed in chapter 4 in order to produce the field maps shown in this chapter.

7.2.2   Acoustic sound speed profiles

The acoustic sound speed profiles estimated using the actual Haro Strait data set are shown in figure 7-1. As discussed in section 6.3.1, the first five shots were fired near the SW and NW WHOI moorings at short range and are less accurate than the subsequent profiles. Further inacurracies might be introduced by the fact that the region near the SW and NW WHOI moorings was the most active region. Barotropic currents were included in the background profile. Although current fluctuations in depth were taken into account as travel time noise in the inversion, strong fluctuations in depth which are consistent over space and time might bias the sound speed profile estimate.

7.2.3   Time-series only field estimate

The field inversion begins before acoustic shots are fired. The only available data are a priori statistical information and local current and sound speed at the IOS

129
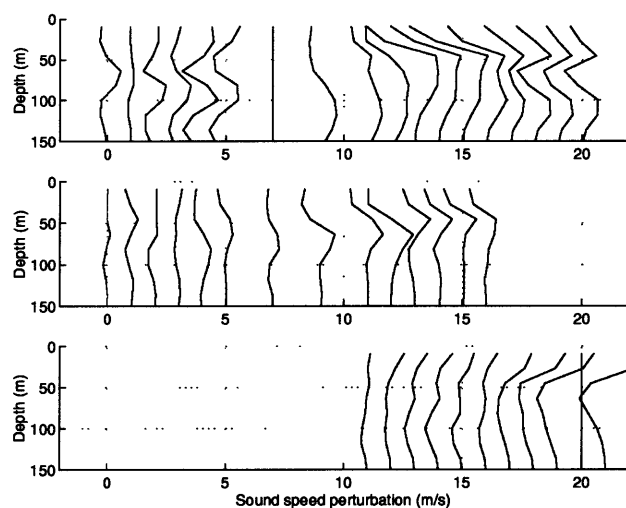
Figure 7-1: Inverted acoustic sound speed profiles (Haro Strait data, shots 20 to 42). Shots which were not properly captured by the acquisition system, or for which direct and surface arrivals were undistinguishable, are missing. Top panel: SW WHOI mooring. Middle panel: NW WHOI mooring. Bottom panel: NE WHOI mooring.

moorings. The first field estimate is shown in figures 7-2 and 7-3 for two depths: 25 and 75 m. The sound speed and current fields are estimated at 00:30 GMT on 06/20/1996 during flood tide. Cold Pacific water is flowing northward in the middle of the channel (near the 123.25 W meridian) from the Juan de Fuca Strait towards the Strait of Georgia. Higher temperatures are measured in the strait between Stuart Island and Spieden Island (NW IOS mooring)at a depth of 25 m. This might indicate the presence of warmer fresh water from the Frasier River. The estimated field at 75 m relies on data from the NE IOS buoy only since the SW IOS mooring has no sensor near that depth. Cold water similar to that observed at shallower depths near the SW IOS mooring is found near the NE mooring as well at 75 m. At 01:00 the balance starts changing (see figures 7-4 and 7-5) and by 01:30 GMT a warm eddy appears to have reached the SW IOS mooring (see figures 7-6 and 7-7). Thus far our sampling capabilities are limited by the fact that the estimate is based on local information from two moorings only. The error levels of the estimated field are relatively high except near the immediate vicinity of the IOS moorings.

130

Figure 7-2: Top view Haro Strait area at 00:30 GMT at a depth of 25m. Upper left panel: sound speed (m/s); upper right panel: sound speed error (m/s); lower left panel: current field (m/s); lower right panel: current perturbation error prior to melding (m/s). Dashed lines: isobaths. Stars: IOS moorings. Circles: WHOI acoustic moorings

Figure 7-3: Top view Haro Strait area at 00:30 GMT at a depth of 75m. Upper left panel: sound speed (m/s); upper right panel: sound speed error (m/s); lower left panel: current field (m/s); lower right panel: current perturbation error prior to melding (m/s). Dashed lines: isobaths. Stars: IOS moorings. Circles: WHOI acoustic moorings

Figure 7-4: Top view Haro Strait area at 01:00 GMT at a depth of 25m. Upper left panel: sound speed (m/s); upper right panel: sound speed error (m/s); lower left panel: current field (m/s); lower right panel: current perturbation error prior to melding (m/s). Dashed lines: isobaths. Stars: IOS moorings. Circles: WHOI acoustic moorings

Figure 7-5: Top view Haro Strait area at 01:00 GMT at a depth of 75m. Upper left panel: sound speed (m/s); upper right panel: sound speed error (m/s); lower left panel: current field (m/s); lower right panel: current perturbation error prior to melding (m/s). Dashed lines: isobaths. Stars: IOS moorings. Circles: WHOI acoustic moorings
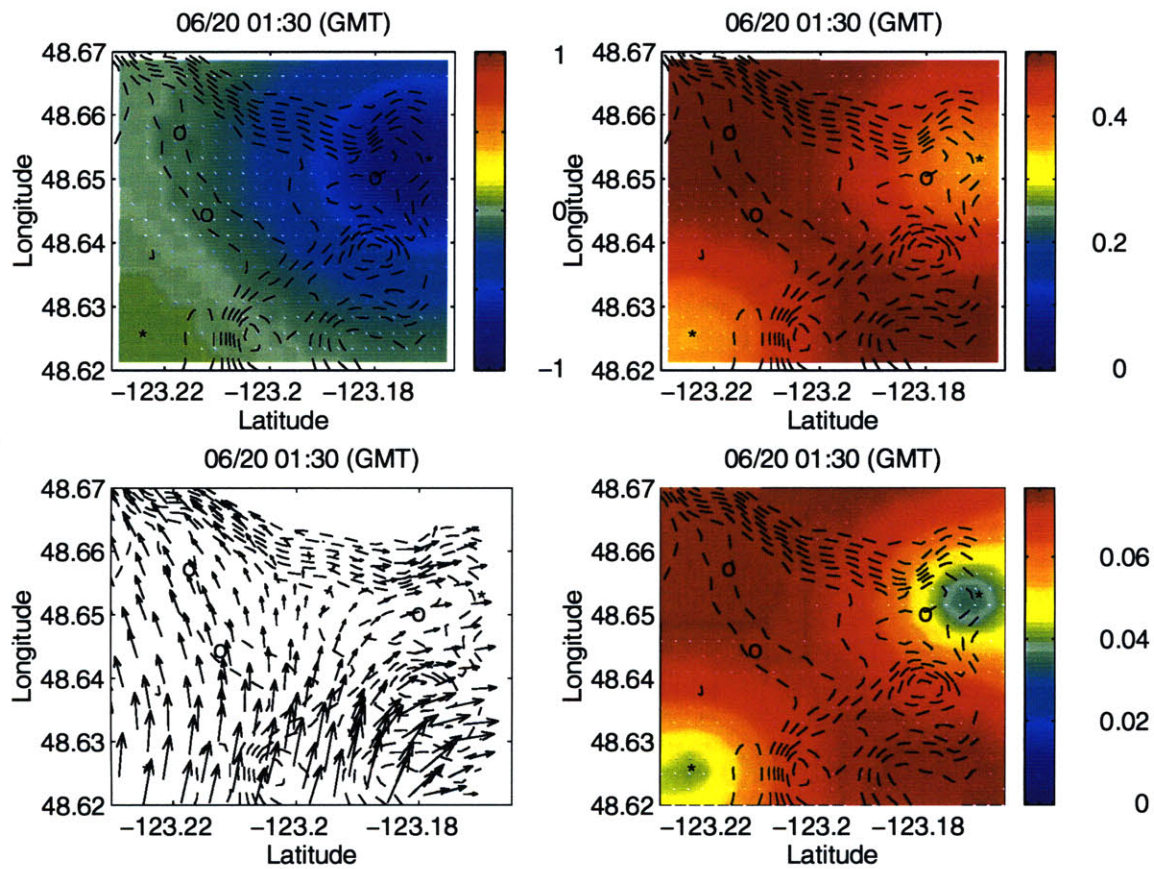
Figure 7-6: Top view Haro Strait area at 01:30 GMT at a depth of 25m. Upper left panel: sound speed (m/s); upper right panel: sound speed error (m/s); lower left panel: current field (m/s); lower right panel: current perturbation error prior to melding (m/s). Dashed lines: isobaths. Stars: IOS moorings. Circles: WHOI acoustic moorings
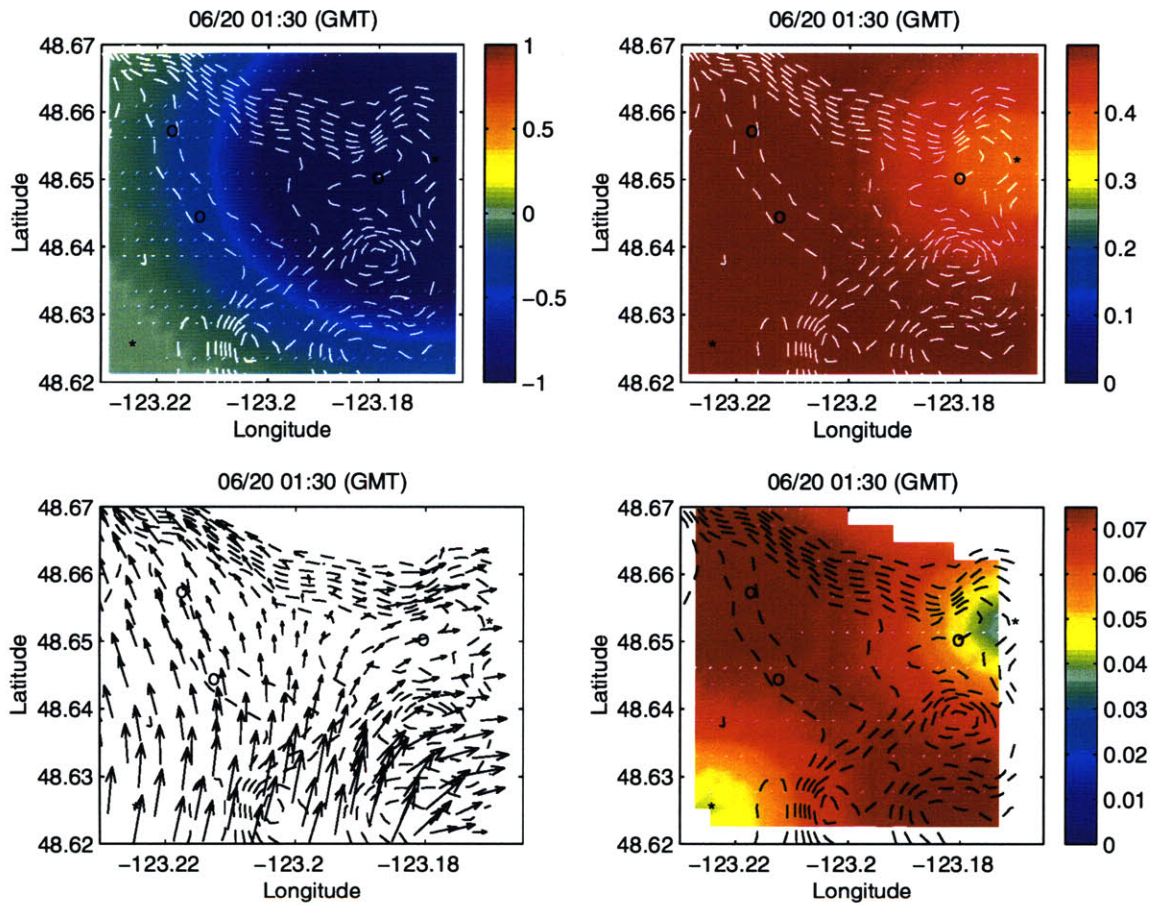
Figure 7-7: Top view Haro Strait area at 01:30 GMT at a depth of 75m. Upper left panel: sound speed (m/s); upper right panel: sound speed error (m/s); lower left panel: current field (m/s); lower right panel: current perturbation error prior to melding (m/s). Dashed lines: isobaths. Stars: IOS moorings. Circles: WHOI acoustic moorings

7.2.4 Combined field estimate

From 02:00 GMT on acoustic shots are fired, acoustic data is acquired, and the inversion can now combine both the non-acoustic data with the acoustic data available. Figures 7-8 through 7-15 show the evolution of the field estimates as more and more acoustic data is taken into account in the inversion. The absence of sound speed sensor near 70 m in depth at the location of the SW IOS mooring leads to a higher error level at that location relative to the 25 m case. The low sound speed error region expands in a way which is consistent with the locations of the shots fired before the time of inversion. The current field error decreases near the acoustic moorings as a result of the melding of array shape data into the current estimate. The 03:30 GMT estimate includes all acoustic data. By this time the sound speed error level has been significantly lowered over the entire region surrounded by the WHOI moorings. The combination of acoustically-derived array shape data at the NE WHOI mooring with data from the nearby IOS mooring leads to a sharp decrease of the current error level. Interestingly enough, this decrease is not observed at other locations where the current estimate relies on a single type of data only.

7.3 Discussion

The scarcity of relevant oceanographic data, particularly in coastal environments such as Haro Strait, makes it difficult to compare the field estimates described above with an independent data set. Aside from the synthetic data test discussed in chapter 6, the actual estimates can be compared to independent temperature records taken at the NW and NE WHOI moorings. Although no concomitant salinity measurements were performed, these temperature records can be converted into an equivalent sound speed by taking into account the strong correlation between temperature and salinity. A linear regression on a set of CTD casts taken a week after this experiment yields the following result:

$$c = 1.3043T + 1470.6 \qquad (7.1)$$

137
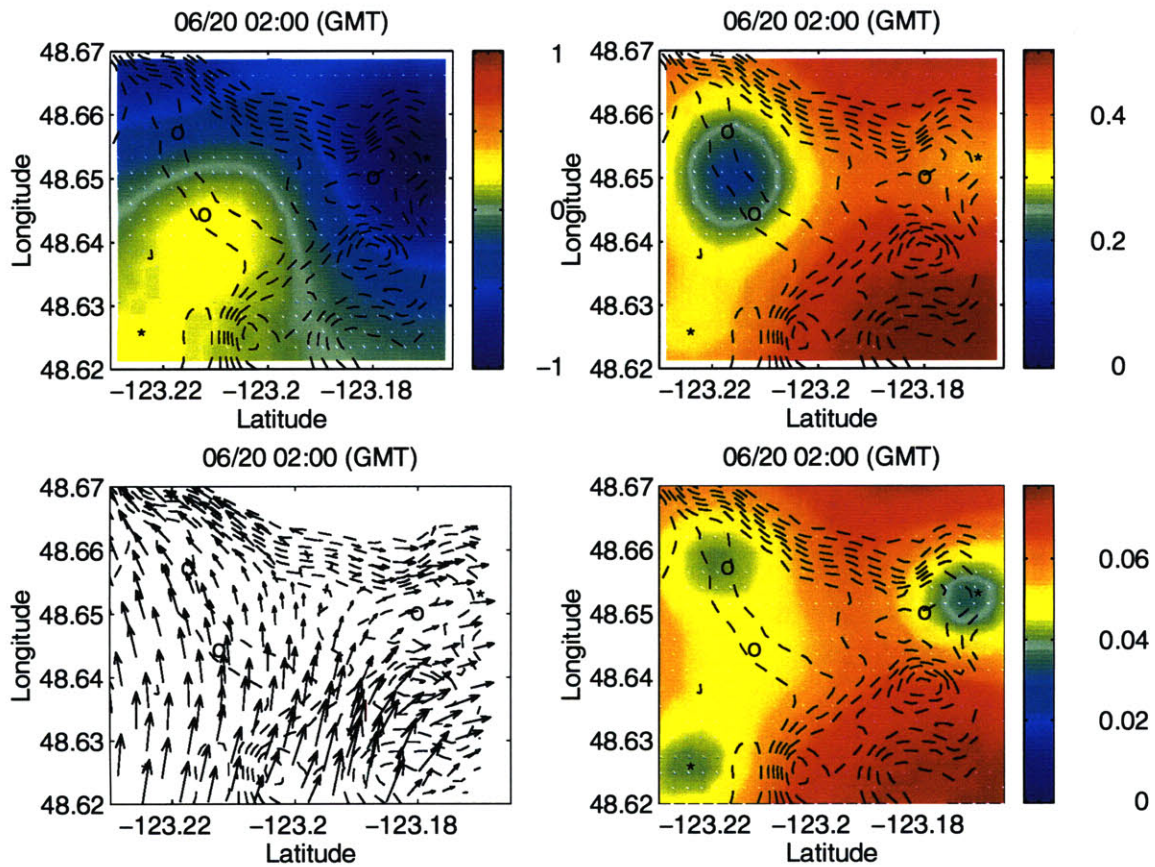
Figure 7-8: Top view Haro Strait area at 02:00 GMT at a depth of 25m. Upper left panel: sound speed (m/s); upper right panel: sound speed error (m/s); lower left panel: current field (m/s); lower right panel: current perturbation error prior to melding (m/s). Dashed lines: isobaths. Stars: IOS moorings. Circles: WHOI acoustic moorings
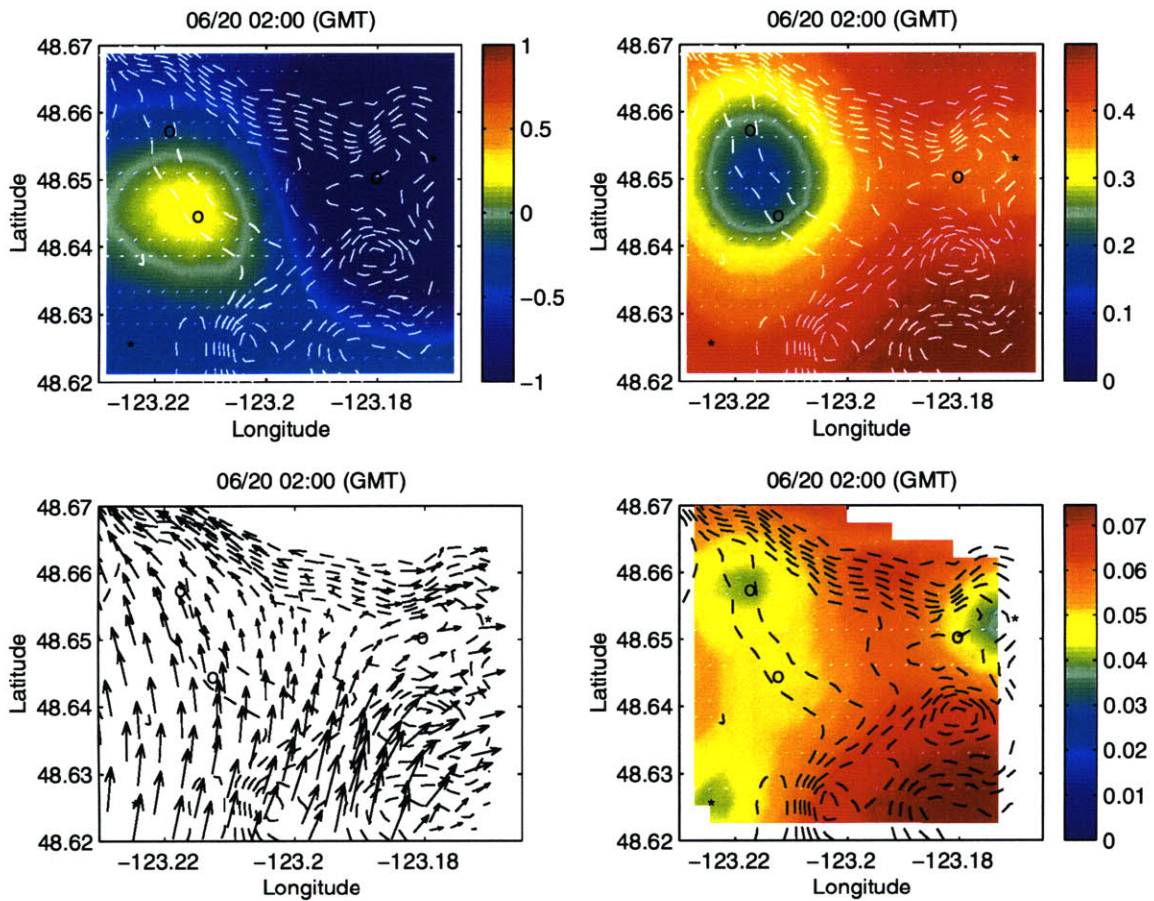
Figure 7-9: Top view Haro Strait area at 02:00 GMT at a depth of 75m. Upper left panel: sound speed (m/s); upper right panel: sound speed error (m/s); lower left panel: current field (m/s); lower right panel: current perturbation error prior to melding (m/s). Dashed lines: isobaths. Stars: IOS moorings. Circles: WHOI acoustic moorings
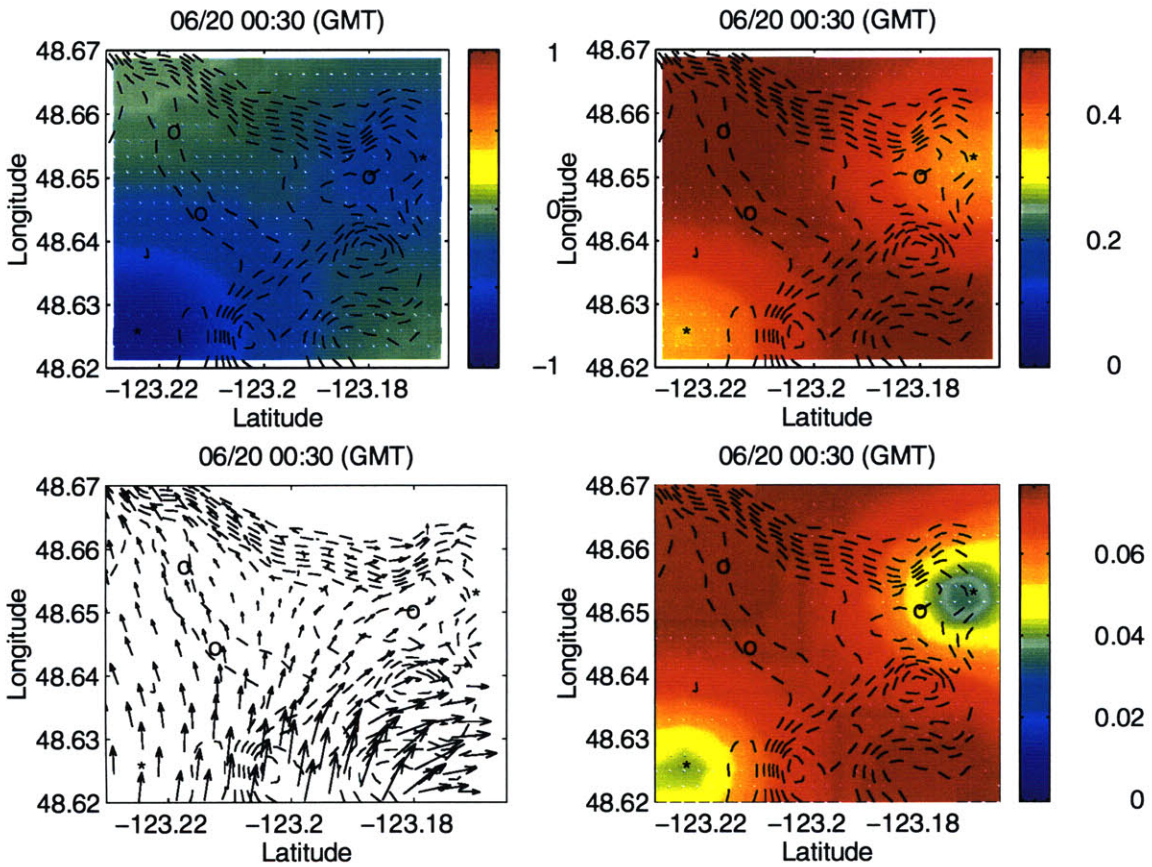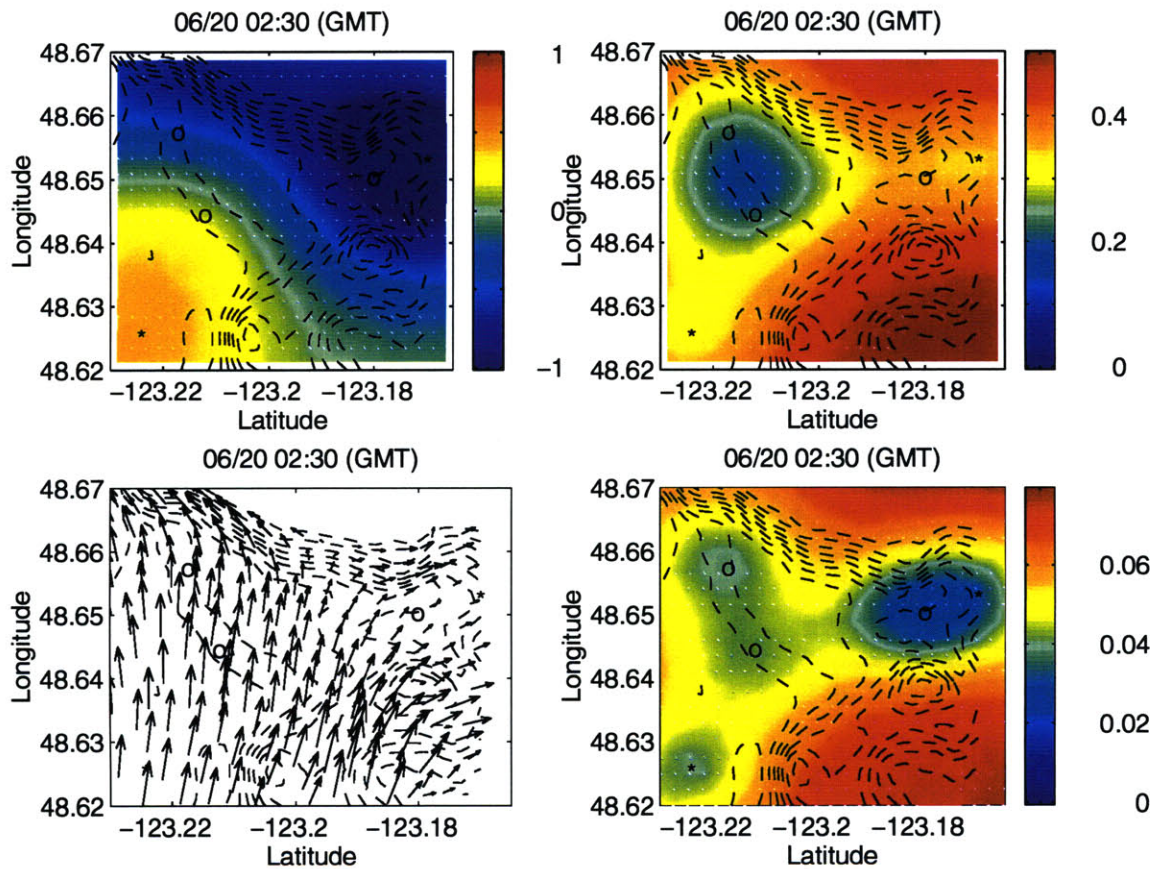
Figure 7-10: Top view Haro Strait area at 02:30 GMT at a depth of 25m. Upper left panel: sound speed (m/s); upper right panel: sound speed error (m/s); lower left panel: current field (m/s); lower right panel: current perturbation error prior to melding (m/s). Dashed lines: isobaths. Stars: IOS moorings. Circles: WHOI acoustic moorings
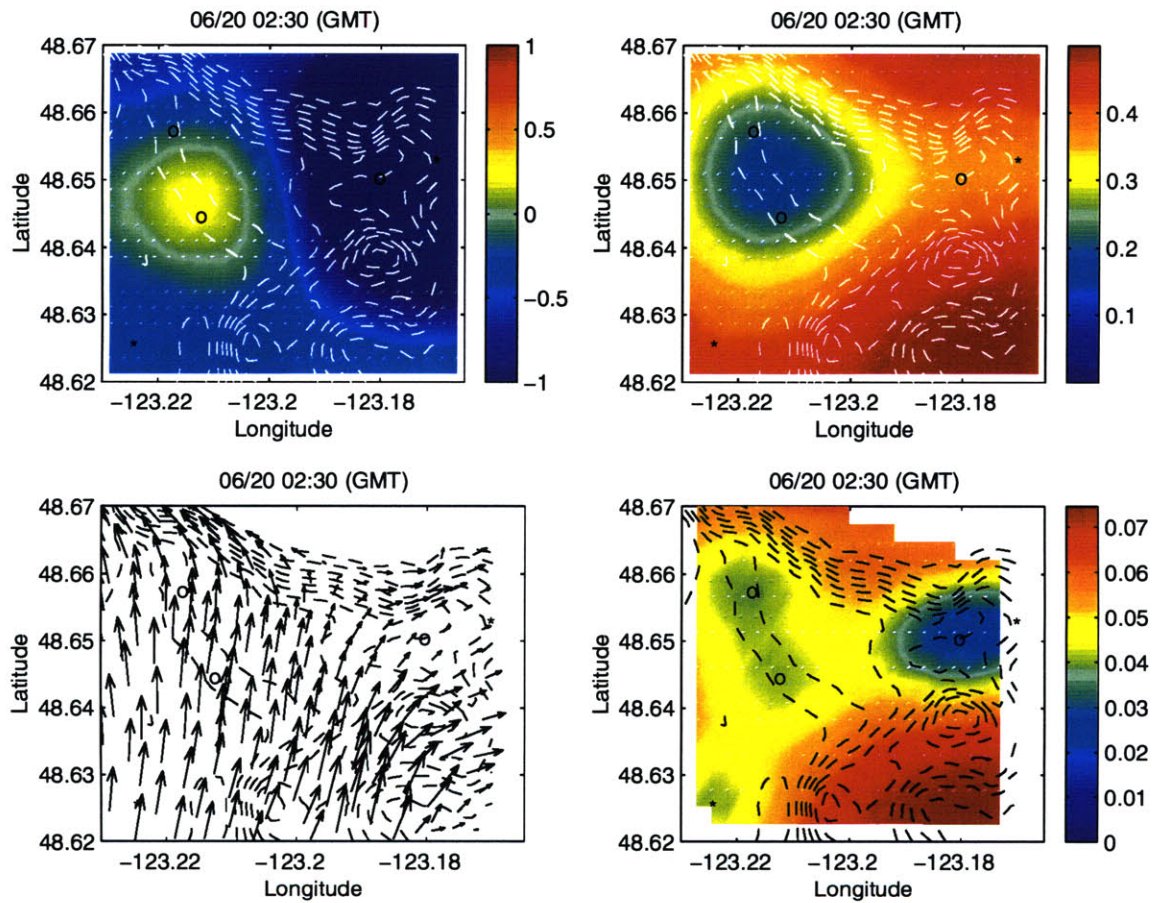
Figure 7-11: Top view Haro Strait area at 02:30 GMT at a depth of 75m. Upper left panel: sound speed (m/s); upper right panel: sound speed error (m/s); lower left panel: current field (m/s); lower right panel: current perturbation error prior to melding (m/s). Dashed lines: isobaths. Stars: IOS moorings. Circles: WHOI acoustic moorings
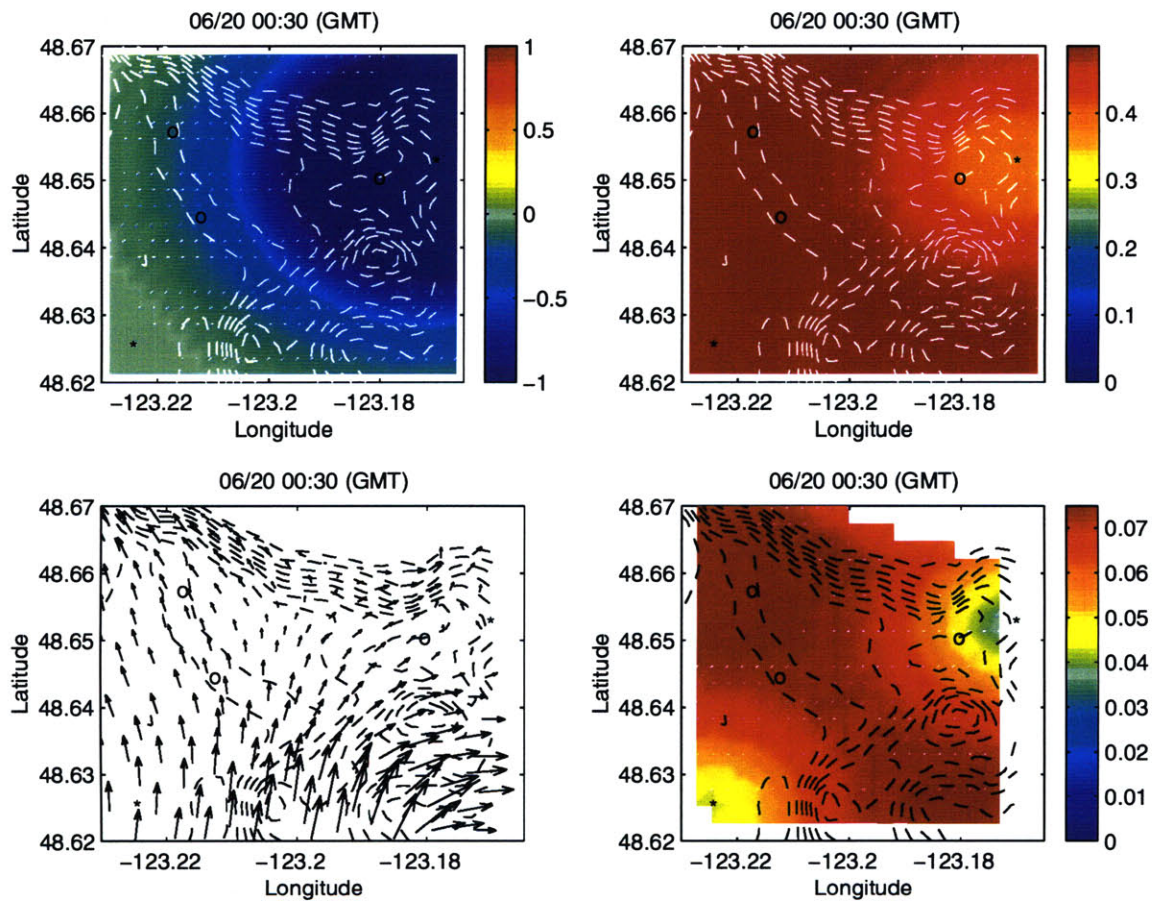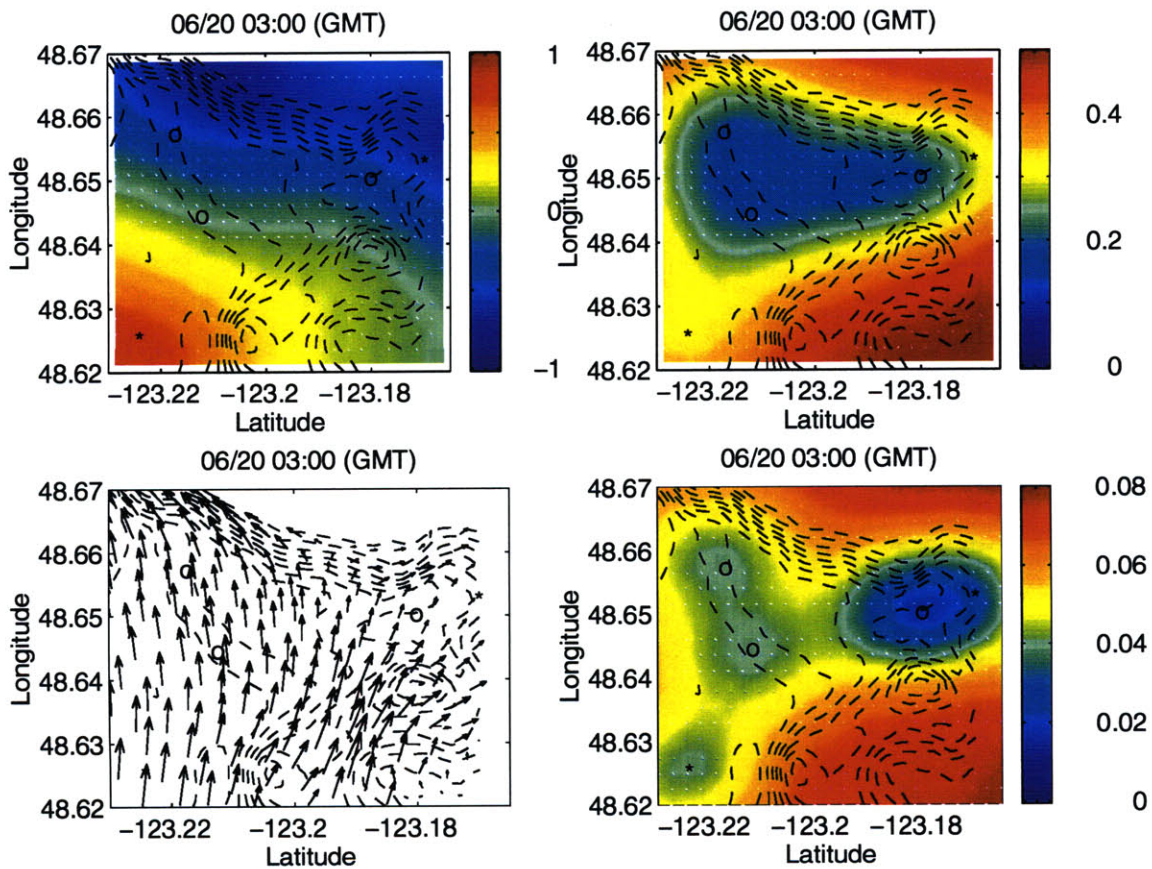
Figure 7-12: Top view Haro Strait area at 03:00 GMT at a depth of 25m. Upper left panel: sound speed (m/s); upper right panel: sound speed error (m/s); lower left panel: current field (m/s); lower right panel: current perturbation error prior to melding (m/s). Dashed lines: isobaths. Stars: IOS moorings. Circles: WHOI acoustic moorings
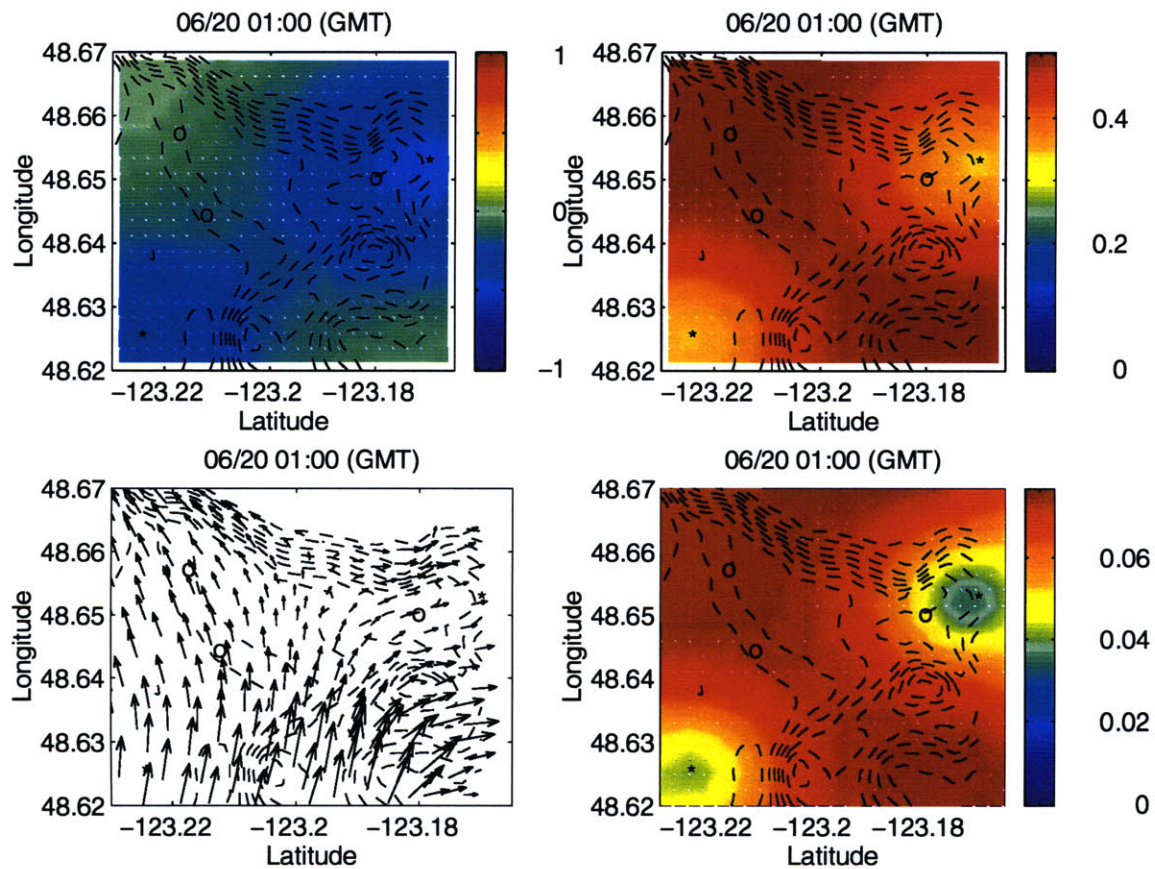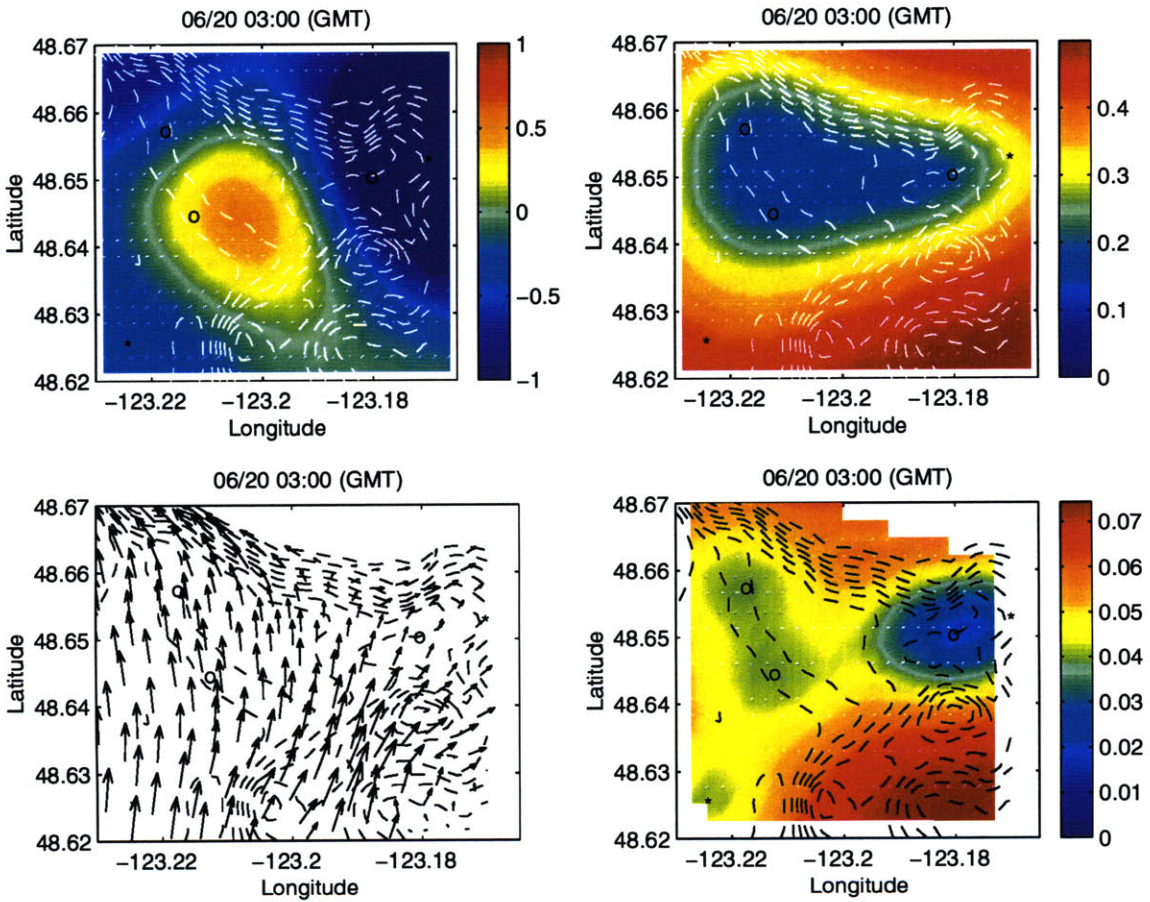
Figure 7-13: Top view Haro Strait area at 03:00 GMT at a depth of 75m. Upper left panel: sound speed (m/s); upper right panel: sound speed error (m/s); lower left panel: current field (m/s); lower right panel: current perturbation error prior to melding (m/s). Dashed lines: isobaths. Stars: IOS moorings. Circles: WHOI acoustic moorings
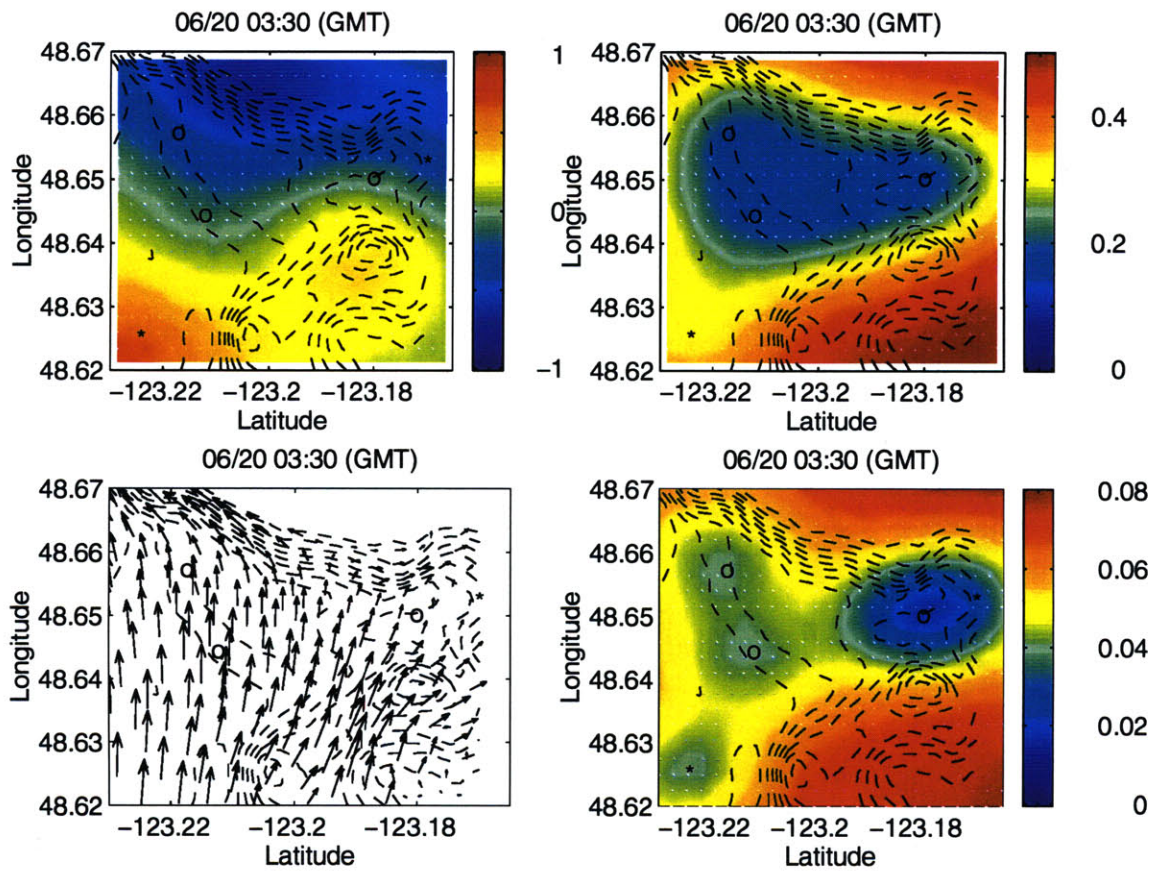
Figure 7-14: Top view Haro Strait area at 03:30 GMT at a depth of 25m. Upper left panel: sound speed (m/s); upper right panel: sound speed error (m/s); lower left panel: current field (m/s); lower right panel: current perturbation error prior to melding (m/s). Dashed lines: isobaths. Stars: IOS moorings. Circles: WHOI acoustic moorings
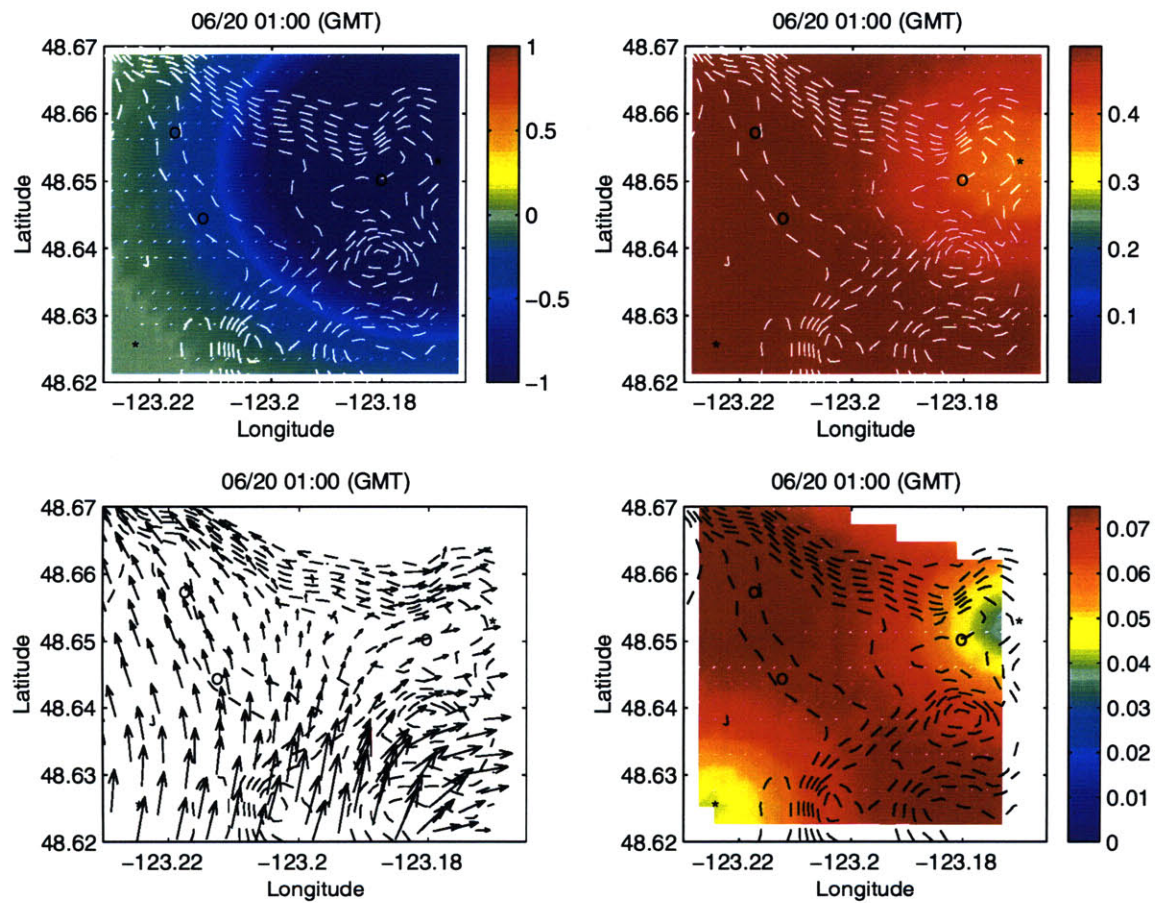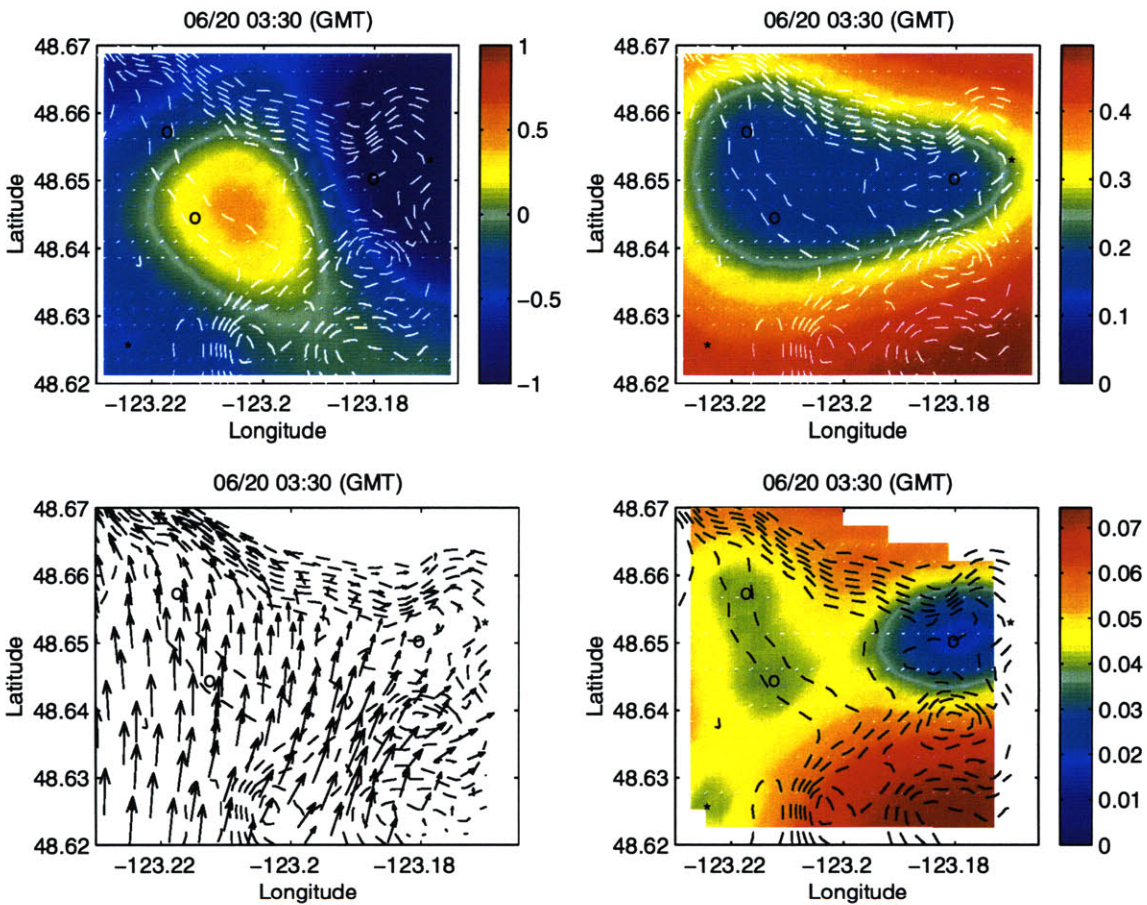
Figure 7-15: Top view Haro Strait area at 03:30 GMT at a depth of 75m. Upper left panel: sound speed (m/s); upper right panel: sound speed error (m/s); lower left panel: current field (m/s); lower right panel: current perturbation error prior to melding (m/s). Dashed lines: isobaths. Stars: IOS moorings. Circles: WHOI acoustic moorings
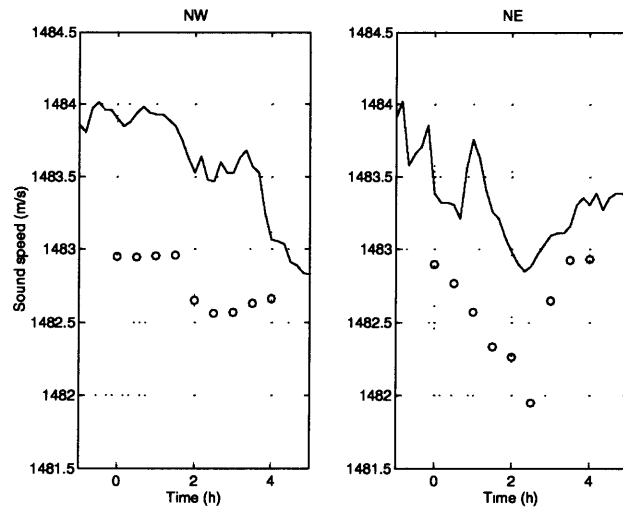
Figure 7-16: Comparison with thermistor data. Left panel: NW WHOI mooring. Right panel: NE WHOI mooring. Solid line: top thermistor (approximate depth: $25m$). Dashed line: second thermistor (approximate depth: $35m$). Circles: sound speed estimate at the relevant mooring location at a depth of $25m$.

where c is the sound speed in m/s and T is the temperature in ^oC. The regression correlation (R^2) is 0.94. The 95% confidence intervals for the gradient and constant terms are $+/-0.0233$ and $+/-0.22$ respectively. The resulting comparison is shown in figure 7-16. Acoustic data is assimilated from 02:00 on. The temperature being around 10^oC, the error induced by the regression is approximately $0.43m/s$, which accounts for some of the $0.8m/s$ bias observed in figure 21. The remainder is attributable to the inversion itself and possible calibration offsets between the WHOI thermistors and the IOS temperature sensors.

The combination of multiple data sets enables the inversion procedure to overcome the individual limitations these might have. The acoustic data set for instance is limited in its ability to measure an absolute sound speed by the fact that the source transmission time is not known accurately and must be estimated when localizing array elements. Thanks to clock synchronization across the acoustic network, sound speed differences can still be measured across different depths and different tracks. On the other hand the IOS mooring time series provide us with an absolute sound

speed reference, but are obviously limited in coverage as shown in figure 7-2, which shows the field estimates before any acoustic data is taken into account. The acoustic array shapes by themselves are a local indication of the current magnitude, but contain almost no information regarding its direction. However, they yield a relatively low-error current estimate in magnitude and direction when combined with the IOS time series and assimilated into Foreman's tidal model. By furthermore coupling the sound speed inversion with the current inversion, the current/sound speed ambiguity inherent to any acoustic inversion can be to some extent resolved without resorting to reciprocal transmissions. This is made possible by extracting the information contained in different data sets through the combined inversion described in section 3.

Combining oceanographic with acoustic data and models traditionally brings up several issues, both theoretical and computational. The resolution of an oceanic field estimate for instance must match that of the acoustic model if an accurate acoustic prediction is to be made based on this field estimate and at an acceptable computational cost [74]. If the field estimate is itself inaccurate the acoustic prediction might diverge widely from reality due to the non-linear dependence of the wave equation on environmental fields. In the present analysis the current field used as input to the acoustic model is produced by a barotropic tidal model. No vertical stratification is therefore added to the reference acoustic sound speed profile. Furthermore, given the short ranges involved in the Haro Strait experiment an individual acoustic transmission has no resolution in range and rays are sensitive primarily to the range-averaged sound-speed profile. The effect of using the tidal current field estimate as input to the ray tracer is then linear for all practical purposes. The effective sound speed profile is offset by some small constant quantity, which yields an approximately constant shift in travel times at the receiver array. The vertical variability of the current field is modeled as additional noise.

The robustness of the current melding scheme (see equation (4.44)) is ensured by the fact that data and model are melded *externally*, i.e., linearly. Of the four basic operations described in figure 4-1 three are therefore linear. The only non-linear operation is the array shape estimation, based on mean square travel time difference minimization. Due to the short ranges involved in this paper this operation can be carried out before the actual sound speed inversion by assuming some constant sound speed profile. Were longer ranges to be involved, the shape estimation would need to be either based on independent short range acoustic transmissions or included in the sound speed inversion. The robustness of the overall inversion scheme derives then from its linearity, i.e., its simplicity, and the combination of different data sets with different resolutions and coverages.

Finally it is worth noticing that due to the particular experimental configuration adopted in Haro Strait the final field estimate might be somewhat biased (see chapter 6). In addition the error estimate of the sound speed field does not formally propagate the error of the current estimate it used as its input. Error modeling, in particular in the case of oceanographic and acoustic model coupling, is still an active area of research and an accurate error model for the final field estimate lies beyond the scope of this paper. However the error fields analyzed with the Haro Strait experiment do show the potential impact of melding different types of data and models on the resulting estimate uncertainty. The combination of various data streams and models is able to exploit the advantages of each data set, e.g., resolution or coverage, and compensate to some extent their limitations.

Chapter 8

Conclusion

8.1 Summary

Forward propagation through a low Mach number, stratified flow was investigated in chapter 3 using a wavenumber integration and a normal mode analysis. Both approaches were unified in a single mathematical formulation suitable for efficient numerical computations. The resulting equations were implemented by modifying existing wavenumber integration and normal mode codes (OASES and KRAKEN). Numerical results for low and high frequency sources in a simple waveguide were shown to exhibit a high degree of agreement between the two approaches, as well as confirm previous theoretical results [43, 7, 73]. An analytical solution was also derived based on the mode set of the medium at rest. Comparison of the analytical solution with the previously computed numerical solution showed that the medium-at-rest mode set cannot adequately account for the presence of flow *regardless of the flow magnitude* if bottom penetration is present or if the current profile exhibits sharp variations with respect to depth. The theoretical feasibility of coherent reciprocal matched-field current tomography was then demonstrated. Assuming accurate knowledge of the acoustic waveguide, a current velocity of 1.5m/s was shown to be measurable at a range of 2km with a resolution of 0.2m/s using a multi-tone CW signal spanning 200–250Hz.

Remote-sensing of current and temperature fields at short ranges in a highly variable, highly uncertain coastal environment was subsequently investigated. A hybrid linear inversion scheme combining heterogeneous data sets, yielding a field estimate within a short amount of time (a few minutes at most), was developed. In order to do so a comprehensive set of observation models linking acoustic ray propagation, array motion, and tidal current as well as temperature sampling was developed in chapter 4. Formal expressions for the field estimates and their expected covariance matrices were derived. A final field estimate was produced by combining various data types over several correlation lengths and times.

The oceanic fields observed in Haro Strait, British Columbia, were then characterized in chapter 5. Second-order statistics were estimated for the current and sound speed fields. The horizontal correlation length was found to be approximately 1km. The vertical correlation length of the sound speed field was measured at 12m. The correlation time was found to be between 2 and 3.5h, depending on the functional form used to fit the data. Sound speed standard deviations of up to 1.5m/s were observed with respect to depth. Sound speed standard deviations with respect to time were measured between 0.13 and 0.50m/s. Current perturbation standard deviations with respect to time were measured between 0.15 and 0.22m/s. The tidal model used in this thesis (Foreman's tidal model), when coupled with the adequate observation model, was found to be a good predictor of acoustic array shapes.

A performance analysis of the inversion algorithm was carried out in chapter 6. Field estimate bias and resolution were explicitly and formally defined. The effect of source position on estimate resolution was found to be consistent with the sampling of the medium by acoustic rays. Acoustic vertical resolution lengths were computed and found to be approximately 15m for the Haro Strait case. Horizontal resolution lengths were estimated to be as low as 950m for the combined field estimate. Field bias was found to be generally negligible within the envelope of the sampling network and non-negligible outside. A synthetic data set was generated in order to calibrate

150

the inversion algorithm. The actual locations of the acoustic sources were found to be sub-optimal, resulting in an East-West shift of the theoretical front position by approximately 800m near the WHOI SW mooring. Except for this shift, the sound speed field was properly recovered. The estimated field was shown to be unbiased when acoustic sources were properly (uniformly) distributed around the region of interest. The effect of current mismatch was found to be negligible as long as current uncertainties were accounted for in the noise model. The influence of frequency coherence on the inversion accuracy was subsequently assessed by computing Cramer-Rao bounds for a typical Haro Strait environment. The frequency-coherent bound was found to decrease with source bandwidth, source range (up to 6km), and signal-to-noise ratio. The frequency-incoherent bound was found to be insensitive to source bandwidth, at best insensitive if not adversely affected by source range, and decrease with signal-to-noise ratio.

Finally, the inversion algorithm was applied to a two-hour segment of the Haro Strait data set, including 45 acoustic transmissions across the sampling network. The benefit from combining acoustic and non-acoustic data was demonstrated. While the combination of acoustic and non-acoustic data decreased the smallest estimated error of the sound speed field by only a few percents of the a priori variance, it also significantly increased the coverage of the low-error area, extending it to almost the entire area covered by the interdisciplinary sampling network. The effect of combining the acoustic and non-acoustic data sets on the current field field estimate was qualitatively different. Coverage was only locally increased, owing to the local nature of both the non-acoustic and the acoustic data (bearing in mind the acoustic data is the acoustically-estimated array shape, not the reciprocal travel time estimate). On the other hand the combination of acoustic and non-acoustic current data near the WHOI NE mooring led to a residual variance of approximately 10%, compared with approximately 30% near the other two WHOI moorings. The resulting sound speed field estimate was found to be in reasonable agreement with independent temperature measurements. The estimated front position was found to be consistent with visual

observations made that day.

8.2 Contributions

This thesis makes contributions to both the forward problem and the inverse problem. The contributions to the problem of acoustic forward propagation through a moving medium are:

- a unified theoretical formulation combining the wavenumber integration and the normal mode approaches was developed. Equations governing the acoustic field were derived for an arbitrary stratified flow. The non-reciprocity of propagation through a flow was shown to be attributed to a non-symmetric distortion of the wavenumber plane as well as the emergence of single poles on one half of the wavenumber plane.

- the problem of computing the upstream and downstream transmission loss in the absence of boundary penetration was solved using modified versions of the computer codes OASES and KRAKEN. Accurate numerical predictions of the acoustic field in the presence of a stratified flow can now be made. Inconsistencies previously found in the literature were resolved.

- regardless of the magnitude of the flow, the medium-at-rest mode set was shown to be fundamentally unsuited to modeling propagation in a non-uniform flow.

Chapter 3 was published in condensed form in the Journal of the Acoustical Society of America [23]. The contributions of this thesis to the inverse problem are:

- a robust, hybrid linear inversion scheme adapted to the estimation of oceanic fields in coastal environments such as Haro Strait was developed. A variety of observation models adapted to AFOS-generated data sets was formulated in a single framework. Expressions for hybrid field estimates as well as their associated estimate variances were derived. These expressions enable the combination of multiple data streams of global and local nature in a robust and versatile fashion while maintaining a manageable computational load.

- the performance of this inversion algorithm was assessed, showing significant gains in coverage and estimated error from the combination of multiple data sets. Signal frequency coherence was shown to be a key asset in shallow water, short range inversion scenarios such as Haro Strait.

- second-order statistics of sound speed and current fields in Haro Strait were computed, and the position of the Haro Strait front during flood tide on 06/20/96 was estimated.

8.3 Future work

The analysis presented in this thesis suggests new avenues of research, drawing on both the forward and the inverse problem as well as tying it to what could be termed the acoustic data assimilation problem. In particular, the flow propagation analysis needs to be formally extended to the case of range-dependent environments. The normal mode formulation based on the medium-at-rest mode set should be investigated assuming the "coupling" matrix $\mathbf{K}$ in equation (3.16) is not diagonal. The benefit from this improvement is that if the (measured) pressure field is projected on the known medium-at-rest mode set and the coupling matrix $\mathbf{K}$ estimated using reciprocal transmissions, a simple singular value decomposition of $\mathbf{K}$ will yield the actual current profile seen by the measured acoustic field.

The inversion scheme would benefit from a number of improvements. First a more sophisticated error model would lead to a better field estimation: in particular the error of the blended current field estimate was not properly modeled in this thesis for lack of analysis of the tidal model error field. Once this error is adequately modeled, error propagation from the current estimate to the sound speed estimate should also be investigated. Second another coastal field estimation experiment should be implemented, validating some of the lessons learned in Haro Strait. Trivial as it may seem, a special attention must be paid to practical issues such as source timing and independent array localization. Proper mastery of these issues will greatly decrease

the uncertainty of the resulting field estimates. Although the algorithm presented in this thesis claims to be fast on robust based on post-processed data, it needs to be put to the test by being actually interfaced with an Adaptive Ocean Sampling Network, either during an Ocean System Simulation Experiment or during an actual experiment at sea.

Finally a great deal of work remains to be done in acoustic data assimilation. So far only travel time perturbations (and in some cases wavenumber perturbations) have been used owing to the linearity of their associated observation model. Although the wave equation depends non-linearly on sound speed and current, an observation model could be cast in linear form using an adequate mapping. The classical finite difference parabolic equation formulation for instance can yield a suitable linear observation model by using the standard two-term expansion of the square root operator, and by using the squared refraction index $c_0^2/c^2(\mathbf{x})$ instead of the sound speed $c(\mathbf{x})$ as the field of interest. Sparse physical sampling will simply show up as a projection matrix multiplying both sides of the observation model equation. The door to full field acoustic data assimilation, or the combination of acoustic data and parabolic equation predictions in a single squared refraction index field estimate, will then be open.

Appendix A

Conditional probability density function of the data vector y

The data vector $\mathbf{y}$ and the model vector $\mathbf{x}$ are related by the observation model:

$$\mathbf{y} = b\mathbf{h}(\mathbf{x}) + \mathbf{n} \tag{A.1}$$

where $\mathbf{n}$ and b are noise terms. The expectation of $\mathbf{y}$ conditioned on $\mathbf{x}$ is then:

$$
\begin{aligned}
E\left[\mathbf{y}|\mathbf{x}\right] &= E\left[b\mathbf{h}(\mathbf{x})|\mathbf{x}\right] + E\left[\mathbf{n}|\mathbf{x}\right] \\
&= E\left[b\right]\mathbf{h}(\mathbf{x}) + E\left[\mathbf{n}\right] \\
&= \beta\mathbf{h}(\mathbf{x})
\end{aligned}
\tag{A.2}
$$

The covariance of $\mathbf{y}$ conditioned on $\mathbf{x}$ can be expressed as:

$$
\begin{aligned}
E\left[\left(\mathbf{y} - \beta\mathbf{h}(\mathbf{x})\right)\left(\mathbf{y} - \beta\mathbf{h}(\mathbf{x})\right)^{\dagger}|\mathbf{x}\right] &= E\left[(b - \beta)^2\mathbf{h}(\mathbf{x})\mathbf{h}(\mathbf{x})^{\dagger}|\mathbf{x}\right] - E\left[\beta\mathbf{n}\mathbf{h}(\mathbf{x})^{\dagger}|\mathbf{x}\right] \\
&\quad - E\left[\beta\mathbf{h}(\mathbf{x})\mathbf{n}^{\dagger}|\mathbf{x}\right] + E\left[\mathbf{n}\mathbf{n}^{\dagger}|\mathbf{x}\right] \\
&= \sigma_b^2\mathbf{h}(\mathbf{x})\mathbf{h}(\mathbf{x})^{\dagger} + \mathbf{R}_{nn}
\end{aligned}
\tag{A.3}
$$

155

Assuming b and $\mathbf{n}$ are jointly Gaussian, the probability density function of $\mathbf{y}$ conditionned on $\mathbf{x}$ can be written as:

$$p_{\mathbf{y}}(\mathbf{y}|\mathbf{x}) = C \, e^{-\frac{1}{2}(\mathbf{y}-\beta\mathbf{h}(\mathbf{x}))^{\dagger}(\mathbf{R}_{nn}+\sigma_b^2\mathbf{h}(\mathbf{x})\mathbf{h}(\mathbf{x})^{\dagger})^{-1}(\mathbf{y}-\beta\mathbf{h}(\mathbf{x}))} \tag{A.4}$$

where C is a normalization constant.

Appendix B

Light bulb acoustic transmissions in Haro Strait

About 45 light bulb acoustic transmissions were used in the combined field estimation. The main source and receiver characteristics are given in the chart below.

shot ID	date	GMT (s)	source LAT	source LONG	source depth	receiver mooring	capture file
20	06/20/96	06600	48.649750	123.218580	70.0	NW	17206453.btd
20	06/20/96	06600	48.649750	123.218580	70.0	SW	17206450.btd
21	06/20/96	06660	48.650467	123.218170	30.5	NW	17206544.btd
21	06/20/96	06660	48.650467	123.218170	30.5	SW	17206540.btd
22	06/20/96	06840	48.651967	123.217250	70.0	NW	17206733.btd
22	06/20/96	06840	48.651967	123.217250	70.0	SW	17206731.btd
23	06/20/96	06960	48.652583	123.216780	30.5	NW	17206804.btd
23	06/20/96	06960	48.652583	123.216780	30.5	SW	17206802.btd
24	06/20/96	07080	48.653500	123.216120	70.0	NW	17206963.btd
24	06/20/96	07080	48.653500	123.216120	70.0	SW	17206960.btd
25	06/20/96	07200	48.653950	123.215750	30.5	NW	17207059.btd
25	06/20/96	07200	48.653950	123.215750	30.5	SW	17207057.btd

shot ID	date	GMT (s)	source LAT	source LONG	source depth	receiver mooring	capture file
27	06/20/96	08400	48.647967	123.206300	70.0	NW	17208260.btd
27	06/20/96	08400	48.647967	123.206300	70.0	SW	17208257.btd
29	06/20/96	09000	48.650167	123.204000	70.0	NW	17208864.btd
29	06/20/96	09000	48.650167	123.204000	70.0	SW	17208861.btd
31	06/20/96	09780	48.651617	123.200430	50.0	NE	17209628.btd
31	06/20/96	09780	48.651617	123.200430	50.0	NW	17209631.btd
31	06/20/96	09780	48.651617	123.200430	50.0	SW	17209628.btd
32	06/20/96	10020	48.652083	123.198430	50.0	NE	17209816.btd
32	06/20/96	10020	48.652083	123.198430	50.0	NW	17209819.btd
32	06/20/96	10020	48.652083	123.198430	50.0	SW	17209815.btd
33	06/20/96	10500	48.645017	123.199250	50.0	NE	17210599.btd
33	06/20/96	10500	48.645017	123.199250	50.0	NW	17210602.btd
33	06/20/96	10500	48.645017	123.199250	50.0	SW	17210597.btd
34	06/20/96	10740	48.645433	123.198580	50.0	NE	17210769.btd
34	06/20/96	10740	48.645433	123.198580	50.0	NW	17210774.btd
34	06/20/96	10740	48.645433	123.198580	50.0	SW	17210769.btd
35	06/20/96	10860	48.645833	123.197830	50.0	NE	17210950.btd
35	06/20/96	10860	48.645833	123.197830	50.0	NW	17210954.btd
35	06/20/96	10860	48.645833	123.197830	50.0	SW	17210950.btd
36	06/20/96	11040	48.646050	123.197170	50.0	NE	17211115.btd
36	06/20/96	11040	48.646050	123.197170	50.0	NW	17211119.btd
36	06/20/96	11040	48.646050	123.197170	50.0	SW	17211115.btd

shot ID	date	GMT (s)	source LAT	source LONG	source depth	receiver mooring	capture file
37	06/20/96	11460	48.647550	123.191720	50.0	NE	17211528.btd
37	06/20/96	11460	48.647550	123.191720	50.0	SW	17211527.btd
38	06/20/96	11640	48.647500	123.190450	50.0	NE	17211697.btd
38	06/20/96	11640	48.647500	123.190450	50.0	SW	17211697.btd
39	06/20/96	11840	48.647433	123.189170	50.0	NE	17211874.btd
39	06/20/96	11840	48.647433	123.189170	50.0	SW	17211873.btd
40	06/20/96	12140	48.647183	123.187350	50.0	NE	17212149.btd
40	06/20/96	12140	48.647183	123.187350	50.0	SW	17212149.btd
41	06/20/96	12320	48.646933	123.186080	50.0	NE	17212339.btd
42	06/20/96	12320	48.646617	123.184750	50.0	NE	17212513.btd

Bibliography

[1] A.B. Baggeroer, W.A. Kuperman, and H. Schmidt. Matched field processing : Source localization in correlated noise as an optimum parameter estimation problem. *Journal of the Acoustical Society of America*, 83(2):571–587, 1988.

[2] A.B. Baggeroer and H. Schmidt. Parameter estimation theory bounds and the accuracy of full field inversions. In O. Diaschok, A. Caiti, P. Gerstoft, and H. Schmidt, editors, *Full field Inversion Methods in Ocean and SeismoAcoustics*, pages 79–84. Kluwer Academic, 1995.

[3] D. Behringer, T. Birdsall, M. Brown, B. Cornuelle, R. Heinmiller, R. Knoz, K. Metzger, W. Munk, J. Spiesberger, R. Spindel, D. Webb, P. Worcester, and C. Wunsch. A demonstration of ocean acoustic tomography. *Nature*, 299:121–125, 1982.

[4] J.G. Bellingham, H. Schmidt, and M. Deffenbaugh. Acoustically Focused Oceanographic Sampling in the Haro strait experiment. *Journal of the Acoustical Society of America*, 100(4):2612, 1996.

[5] D.I. Blokhintsev. The propagation of sound in an inhomogeneous and moving medium. *Journal of the Acoustical Society of America*, 18:322–328, 1946.

[6] L.M. Brekhovskikh and O.A. Godin. *Acoustics of Layered Media I*. Springer-Verlag, 1990.

[7] L.M. Brekhovskikh and O.A. Godin. *Acoustics of Layered Media II*. Springer-Verlag, 1992.

[8] E.F. Carter and A.R. Robinson. Analysis models for the estimation of oceanic fields. *Journal of Atmospheric and Oceanic Technology*, 4:pp49–74, March 1987.

[9] D. Chester, P. Malanotte-Rizzoli, and C. Lynch, J.F.and Wunsch. The eddy radiation field of the Gulf Stream as measured by ocean acoustic tomography. *Geophysical Research Letter*, 21:181–184, 1994.

[10] C.S. Chiu, J.F. Lynch, and O.M. Johanessen. Tomographic resolution of mesoscale eddies in the Marginal Ice Zone: a preliminary study. *Journal of Geophysical Research*, 92(C7):6886–6902, 1987.

[11] C.S. Chiu, J.H. Miller, and J.F. Lynch. Inverse techniques for coastal acoustic tomography. In D. Lee and M.H. Schultz, editors, *Theoretical and Computational Acoustics – Volume 2*, pages 917–931. Wolrd Scientific Publishing Co., 1994.

[12] C.S. Chiu, J.H. Miller, and J.F. Lynch. Forward coupled-mode propagation modeling for coastal acoustic tomography. *Journal of the Acoustical Society of America*, 99(2):793–802, 1996.

[13] I.P. Chunchuzov. Field of a low-frequency point source of sound in an atmosphere with a nonuniform wind-height distribution. *Soviet Physics - Acoustics*, 30(4):323–326, 1984.

[14] M.D. Collins, B.E. McDonald, W.A. Kuperman, and W.L. Siegmann. Jovian acoustics and comet Shoemaker-Levy 9. *Journal of the Acoustical Society of America*, 97(4):2147–2158, 1995.

[15] M.D. Collins, B.E. McDonald, W.A. Kuperman, and W.L. Siegmann. Erratum: Jovian acoustics and comet Shoemaker-Levy 9 [J.Acoust.Soc.Am. 97, 2147–2158 (1995)]. *Journal of the Acoustical Society of America*, 100(6):3983–3984, 1996.

[16] B. Cornuelle and B. M. Howe. High spatial resolution in vertical slice ocean acoustic tomography. *Journal of Geophysical Research*, 92(C11):11,680–11,692, 1987.

[17] B. Cornuelle, W. Munk, and P. Worcester. Ocean acoustic tomography from ships. *Journal of Geophysical Research*, 94:6232–6250, 1989.

[18] B. Cornuelle, C. Wunsch, D. Behringer, T. Birdsall, M. Brown, R. Heinmiller, R. Knox, K. Metzger, W. Munk, J. Spiesberger, R. Spindel, D. Webb, and P. Worcester. Tomographic maps of the ocean mesoscale. Part I : pure acoustics. *Journal of Physical Oceanography*, 15(2):133–152, 1985.

[19] B.D. Cornuelle and Worcester P.F. Ocean acoustic tomography: integral data and ocean models. In P. Malanotte-Rizzoli, editor, *Modern approaches to data assimilation in ocean modeling*, pages 97–115. Elsevier, 1996.

[20] G.B. Crawford, R.J. Lataitis, and S.F. Clifford. Remote sensing of ocean flows by spatial filtering of acoustic scintillations : theory. *Journal of the Acoustical Society of America*, 88:442–454, 1990.

[21] H.A. DeFerrari and H.B. Nguyen. Acoustic reciprocal transmission experiments, Florida Straits. *Journal of the Acoustical Society of America*, 79:299–315, 1986.

[22] B.D. Dushaw, P.F. Worcester, B.D. Cornuelle, and B.M. Howe. Barotropic currents and vorticity in the central north Pacific Ocean during summer 1987 determined from long-range reciprocal acoustic transmission. *Journal of Geophysical Research*, 99:3263–3272, 1994.

[23] P. Elisseeff and H. Schmidt. Acoustic propagation through a low Mach number, stratified flow. *Journal of the Acoustical Society of America*, 101(4):1936–1944, 1997.

[24] D.M. Farmer and G.B. Crawford. Remote sensing of ocean flows by spatial filtering of acoustic scintillations : observations. *Journal of the Acoustical Society of America*, 90:1582–1591, 1991.

[25] D.M. Farmer and G.B. Crawford. Remote sensing of ocean flows by spatial filtering of acoustic scintillations : observations. *Journal of the Acoustical Society of America*, 90:1582–1591, 1991.

[26] M.G.G. Foreman, R.A. Walters, R.F. Henry, C.P. Keller, and A.G. Dolling. A tidal model for eastern juan de fuca strait and the southern strait of georgia. *Journal of Geophysical Research*, 100(C1):721–740, 1995.

[27] E.R. Franchi and M.J. Jacobson. Ray propagation in a channel with depth-variable sound speed and current. *Journal of the Acoustical Society of America*, 52:316–331, 1972.

[28] E.R. Franchi and M.J. Jacobson. Effect of hydrodynamic variations on sound transmission across a geostrophic flow. *Journal of the Acoustical Society of America*, 54:1302–1311, 1973.

[29] E.R. Franchi and M.J. Jacobson. An environmental-acoustics model for sound propagation in a geostrophic flow. *Journal of the Acoustical Society of America*, 53:835–847, 1973.

[30] W.I. Futterman. Dispersive body waves. In M.N. Toksoz and D.H. Johnston, editors, *Seismic wave attenuation*. Society of Exploration Geophysicists, Geophysics reprint series No.2, 1981.

[31] O.A. Godin. Discrete spectrum of a sound field in a moving medium. *Soviet Physics – Acoustics*, 36(4):355–359, 1990.

[32] O.A. Godin, Y.U. Mikhin, and A.V. Mokhov. A full field inversion method for acoustic tomography of ocean currents. In O. Diachok, A. Caiti, P. Gerstoft, and H. Schmidt, editors, *Full field inversion methods in ocean and seismo-acoustics*, pages 261–266. Kluwer Academic Publishers, 1995.

[33] N.S. Grigor'eva and M.I. Yavor. Influence on the sound field in the ocean of a large-scale ocean current that qualitatively alters the nature of guided-wave sound propagation. *Soviet Physics - Acoustics*, 32(6):482–485, 1986.

[34] M. Grund, M. Johnson, and D. Herold. Haro strait tidal fron mapping experiment. Technical report, Woods Hole Oceanographic Institution, February 1997.

[35] R.M. Hamson and R.M. Heitmeyer. Environmental and system effects on source localization in shallow water by the matched-field processing of a vertical array. *Journal of the Acoustical Society of America*, 86:1950–1959, 1989.

[36] R.H. Hardin and F.D. Tappert. Applications of the split-step Fourier method to the numerical solution of nonlinear and variable coefficient wave equations. *SIAM Review*, 15:423, 1973.

[37] R.H. Headrick, J.L. Spiesberger, and P.J. Bushong. Tidal signals in basin-scale acoustic transmissions. *Journal of the Acoustical Society of America*, 93:790–802, 1993.

[38] G.S. Heller. Propagation of acoustic discontinuities in an inhomogeneous moving medium. *Journal of the Acoustical Society of America*, 25:950–951, 1953.

[39] B.M. Howe. Multiple receivers in single vertical slice ocean acoustic tomography experiments. *Journal of Geophysical Research*, 92(C9):9479–9486, 1987.

[40] B.M. Howe, P.F. Worcester, and R.C. Spindel. Ocean acoustic tomography : mesoscale velocity. *Journal of Geophysical Research*, 92(C4):3785–3805, 1987.

[41] U. Ingard and V.K. Singhal. Upstream and downstream sound radiation into a moving fluid. *Journal of the Acoustical Society of America*, 54(5):1343–1346, 1973.

[42] F.B. Jensen, W.A. Kuperman, M.B. Porter, and H. Schmidt. *Computational Ocean Acoustics*. AIP, 1994.

[43] D.S. Jones and J.D. Morgan. The instability of a vortex sheet on a subsonic stream under acoustic radiation. *Proceedings of the Cambridge Philosophical Society*, 72:465–488, 1972.

[44] T.K. Kapoor. *Three-dimensional acoustic scattering from arctic ice protuberances*. PhD thesis, Massachusetts Institute of Technology, June 1995.

[45] D.S. Ko, H.A. DeFerrari, and P. Malanotte-Rizolli. Acoustic tomography in the Florida Strait : temperature, current and vorticity measurements. *Journal of Geophysical Research*, 94:6197–6211, 1989.

[46] N.P. Lan and F.D. Tappert. Parabolic equation modeling of the effects of ocean currents on sound transmission and reciprocity in the time domain. *Journal of the Acoustical Society of America*, 78:642–648, 1985.

[47] D. Lee. Three-dimensional effects: interface between the Harvard Open Ocean Model and a three-dimensional acoustic model. In A.R. Robinson and L. Ding, editors, *Oceanography and acoustics: prediction and propagation models*. AIP, 1994.

[48] Y.L. Li, M.J. White, and S.J. Franke. New fast field programs for anisotropic sound propagation through an atmosphere with a wind velocity profile. *Journal of the Acoustical Society of America*, 95(2):718–726, 1994.

[49] C.J. Lozano, A.R. Robinson, H.G. Arango, A. Gangopadhyay, Q. Sloan, P.J. Haley, L. Anderson, and W. Leslie. An interdisciplinary ocean prediction system: assimilation strategies and structured data models. In P. Malanotte-Rizzoli, editor, *Modern approaches to data assimilation in ocean modeling*, pages 413–452. Elsevier, 1996.

[50] K.V. Mackenzie. Nine-term equation for sound speed in the oceans. *Journal of the Acoustical Society of America*, 70:807–812, 1981.

[51] P. Malanotte-Rizzoli. *Modern approaches to data assimilation in ocean modeling*. Elsevier, 1996.

[52] P. Malanotte-Rizzoli, editor. *Modern approaches to data assimilation in ocean modeling*. Elsevier, 1996.

[53] D. Menemenlis and D. Farmer. Acoustical measurements of current and vorticity beneath ice. *J. Atmos. Oceanic. Tech*, 9:827–849, 1992.

[54] J.A. Mercer and J.R. Booker. Long-range propagation of sound through oceanic mesoscale structures. *Journal of Geophysical Research*, 88:689–699, 1983.

[55] P.M. Morse and K.U. Ingard. *Theoretical Acoustics*. Princeton University Press, 1986.

[56] W. Munk and et al. Tidal effects on long-range sound transmission. *Journal of Geophysical Research*, 86:6399–6410, 1981.

[57] W. Munk, P. Worcester, and C. Wunsch. *Ocean Acoustic Tomography*. Cambridge University Press, 1995.

[58] W. Munk and C. Wunsch. Ocean acoustic tomography : a scheme for large scale monitoring. *Deep Sea Research*, 26A:123–161, 1979.

[59] V.E. Ostashev. Discrete spectrum of the sound field of a point source in a stratified moving medium. *Soviet Physics - Acoustics*, 32(4):303–306, 1986.

[60] A.R. Parsons, R.H. Bourke, R.D. Muench, C.S. Chiu, J.F. Lynch, J.H. Miller, A.J. Plueddemann, and R. Pawlowicz. The Barents Sea Polar Front in summer. *Journal of Geophysical Research*, 101(C6):14,201–14,221, 1996.

[61] M.B. Porter and E.L. Reiss. A numerical method for ocean acoustic normal modes. *Journal of the Acoustical Society of America*, 76:244–252, 1984.

[62] M.B. Porter and E.L. Reiss. Numerical method for acoustic normal modes for shear flows. *Journal of Sound and Vibration*, 100(1):91–105, 1985.

[63] D.C. Pridmore-Brown. Sound propagation in a temperature- and wind-stratified medium. *Journal of the Acoustical Society of America*, 34:438–443, 1962.

[64] J.S. Robertson, W.L. Siegmann, and M.J. Jacobson. Current and current shear effects in the parabolic approximation for underwater sound channels. *Journal of the Acoustical Society of America*, 77(5):1768–1780, 1985.

[65] J.S. Robertson, W.L. Siegmann, and M.J. Jacobson. Acoustical effects of ocean current shear structures in the parabolic approximation. *Journal of the Acoustical Society of America*, 82:559–573, 1987.

[66] J.S. Robertson, W.L. Siegmann, and M.J. Jacobson. A treatment of three-dimensional underwater propagation through a steady shear flow. *Journal of the Acoustical Society of America*, 86:1484–1489, 1989.

[67] A.R. Robinson, J.C. Carman, and S.M. Glenn. A dynamical system for acoustic applications. In A.R. Robinson and D. Lee, editors, *Oceanography and Acoustics: prediction and propagation models*, pages 80–117. AIP, 1994.

[68] T.B. Sanford. Observation of strong current shears in the deep ocean and some implications on sound rays. *Journal of the Acoustical Society of America*, 56:1118–1121, 1974.

[69] H. Schmidt. *SAFARI : Seismo-acoustic fast field algorithm for range independent environments. User's Guide.* SACLANT Undersea Research Centre, La Spezia, Italy, 1988.

[70] H. Schmidt and A.B. Baggeroer. Physics-imposed resolution and robustness issues in seismo-acoustic parameter inversion. In O. Diaschok, A. Caiti, P. Gerstoft, and H. Schmidt, editors, *Full Field Inversion Methods in Ocean and Seismo-Acoustics*, pages 85–90. Kluwer Academic, 1995.

[71] H. Schmidt, J.G. Bellingham, and P. Elisseeff. Acoustically Focused Oceanographic Sampling in coastal environments. In E. et al. Pouliquen, editor, *Rapid Environmental Assessment*. NATO Conference Proceedings, SACLANTCEN, 1997.

[72] H. Schmidt, J.G. Bellingham, M. Johnson, D. Herold, D. Farmer, and R. Pawlowicz. Real-time frontal mapping with AUVs in a coastal environment. In *IEEE Proceedings Oceans 96*, 1996.

[73] H. Schmidt and W.A. Kuperman. Spectral and modal representation of the Doppler-shifted field in ocean waveguides. *Journal of the Acoustical Society of America*, 96(1):386–395, 1994.

[74] W.L. Siegmann, D. Lee, G. Botseas, A.R. Robinson, and S.M. Glenn. Sensitivity issues for interfacing mesoscale ocean prediction and parabolic acoustic propagation models. In A.R. Robinson and D. Lee, editors, *Oceanography and acoustics: prediction and propagation models*, pages 133–160. AIP, 1994.

[75] J.L. Spiesberger, R.C. Spindel, and K. Metzger. Stability and identification of long range ocean acoustic multipaths. *Journal of the Acoustical society of America*, 67:2011–2017, 1980.

[76] R.C. Spindel and J.L. Spiesberger. Multipath variability due to the Gulf Stream. *Journal of the Acoustical Society of America*, 69:982–988, 1981.

[77] L.A. Stallworth and M.J. Jacobson. Acoustic propagation in an isospeed channel with uniform tidal current and depth change. *Journal of the Acoustical Society of America*, 48:382–391, 1970.

[78] L.A. Stallworth and M.J. Jacobson. Acoustic propagation in an uniformly moving ocean channel with a depth-dependent sound speed. *Journal of the Acoustical Society of America*, 52:344–355, 1972.

[79] L.A. Stallworth and M.J. Jacobson. Sound transmission in an isospeed ocean channel with depth-dependent current. *Journal of the Acoustical Society of America*, 51:1738–1750, 1972.

[80] A. Tarantola. *Inverse problem theory - methods for data fitting and model parameter estimation.* Elsevier, 1987.

[81] R.J. Thompson. Ray theory for an inhomogeneous moving medium. *Journal of the Acoustical society of America*, 51:1675–1682, 1972.

[82] P. Ugincius. Acoustic ray equations for a moving, inhomogeneous medium. *Journal of the Acoustical society of America*, 37:476–479, 1965.

[83] J.E. White. *Underground sound - Application of seismic waves*. Elsevier, 1983.

[84] P. Worcester. An example of ocean acoustic multipath identification at long range using both travel time and vertical arival angle. *Journal of the Acoustical Society of America*, 70:1743–1747, 1981.